DISSERTATION

RETRIEVAL TECHNIQUES AND INFORMATION CONTENT ANALYSIS TO IMPROVE REMOTE SENSING OF ATMOSPHERIC WATER VAPOR, LIQUID WATER AND TEMPERATURE FROM GROUND-BASED MICROWAVE RADIOMETER MEASUREMENTS

Submitted by

Swaroop Sahoo

Department of Electrical and Computer Engineering

In partial fulfillment of the requirements

For the Degree of Doctor of Philosophy

Colorado State University

Fort Collins, Colorado

Spring 2015

Doctoral Committee:

Advisor: Steven C. Reising

Branislav M. Notaros
Jothiram Vivekanandan
Steven A. Rutledge

ABSTRACT

RETRIEVAL TECHNIQUES AND INFORMATION CONTENT ANALYSIS TO IMPROVE REMOTE SENSING OF ATMOSPHERIC WATER VAPOR, LIQUID WATER AND TEMPERATURE FROM GROUND-BASED MICROWAVE RADIOMETER MEASUREMENTS

Observation of profiles of temperature, humidity and winds with sufficient accuracy and fine vertical and temporal resolution are needed to improve mesoscale weather prediction, track conditions in the lower to mid-troposphere, predict winds for renewable energy, inform the public of severe weather and improve transportation safety. In comparing these thermodynamic variables, the absolute atmospheric temperature varies only by 15%; in contrast, total water vapor may change by up to 50% over several hours. In addition, numerical weather prediction (NWP) models are initialized using water vapor profile information, so improvements in their accuracy and resolution tend to improve the accuracy of NWP. Current water vapor profile observation systems are expensive and have insufficient spatial coverage to observe humidity in the lower to mid-troposphere. To address this important scientific need, the principal objective of this dissertation is to improve the accuracy, vertical resolution and revisit time of tropospheric water vapor profiles retrieved from microwave and millimeter-wave brightness temperature measurements.

Ground-based microwave and millimeter-wave brightness temperature measurements from radiometers operating at frequencies near the 22.235 and 183.31 GHz water vapor absorption lines have been used extensively for retrieval of water vapor profiles. Such microwave radiometers have the advantages of relatively low cost, potential for future network deployment, and frequent revisit times for sensing dynamic changes as well as gradients in water vapor profiles. To retrieve water vapor profiles from microwave brightness temperature measurements, Bayesian optimal estimation is commonly used, requiring a water vapor background data set. Microwave brightness temperature measurements provide information on water vapor at the location and time of measurement, while background data sets provide statistics on the general behavior and variability of water vapor. Brightness temperature measurements at multiple frequencies contribute information to profile retrieval, although the information at multiple frequencies may be highly correlated due to similar sensitivities to changes in atmospheric pressure, temperature and water vapor mixing ratio as a function of altitude. To retrieve profiles with optimal vertical resolution and minimum retrieval error, as many independent measurements as possible need to be obtained, within the limitations of available resources. To this end, an analysis is performed to determine the amount of independent information about water vapor and temperature available from the microwave and millimeter-wave frequency spectrum. For this, a feature selection algorithm based on weighting function analysis is used to determine sets of frequencies between 10 and 200 GHz that have the greatest number of degrees of freedom for water vapor and temperature retrieval. Another analysis is performed to determine the optimal background data set size and layer thickness to yield maximum information about water vapor variability to sense dynamic changes in water vapor profiles at a particular location and a particular time of year. To explore the retrieval technique's capability and performance, the

HUMidity EXperiment 2011 (HUMEX11) was conducted at the U.S. Department of Energy's (DOE) Atmospheric Radiation Measurement (ARM) Southern Great Plains (SGP) site. The radiometer-retrieved profiles are compared with Raman lidar-retrieved profiles to determine their accuracy.

In addition to water vapor, clouds and precipitation also strongly affect microwave and millimeter-wave brightness temperature measurements. Since the presence of liquid water reduces the accuracy of water vapor retrievals, it is important to distinguish between clear and cloudy sky conditions and to estimate the amount of liquid water in the atmosphere. To address this need, a technique has been developed based on the ratio of the ground-based brightness temperature at 23.8 GHz to that at 30.0 GHz, known as the vapor liquid water ratio (VLWR). During clear sky conditions, the VLWR is much greater than unity, but when sufficient liquid water is present, the VLWR approaches unity. This sensitivity of the VLWR is used to develop an algorithm to retrieve integrated water vapor and liquid water in the atmosphere over a wide range of elevation angles. Measured brightness temperatures are obtained from the University of Miami radiometer during the DYNAmics of the Madden-Julian Oscillation (DYNAMO) experiment. The water vapor and liquid water retrieved from microwave brightness temperatures are compared to those retrieved from radar measurements by the National Center for Atmospheric Research S-PolKa (dual-wavelength S- and Ka-band) radar, which was collocated with the radiometer.

This dissertation advances the state of knowledge of retrieval of atmospheric water vapor from microwave brightness temperature measurements. It focuses on optimizing two information sources of interest for water vapor profile retrieval, i.e. independent measurements and background data set size. From a theoretical perspective, it determines sets of frequencies in the ranges of 20–23, 85–90 and 165–200 GHz that are optimal for water vapor retrieval from each of ground-based and airborne radiometers. The maximum number of degrees of freedom for the selected frequencies for ground-based radiometers is 5-6, while the optimum vertical resolution is 0.5 to 1.5 km. On the other hand, the maximum number of degrees of freedom for airborne radiometers is 8-9, while the optimum vertical resolution is 0.2 to 0.5 km. From an experimental perspective, brightness temperature data sets from the HUMEX11 and DYNAMO field experiments have been used to improve knowledge of the impact of the background information on retrieval of water vapor profiles and estimation of water vapor and liquid water using low elevation angle data sets. HUMEX11 measurements have been used to improve retrieval performance by choosing optimal atmospheric a-priori statistics of 35-55 profiles and layer thickness of 100-m to detect dynamic changes and gradients. DYNAMO measurements have been used to retrieve slant water path and slant liquid water with estimated error of less than 10% and 25%, respectively, for all elevation angles of interest.

These theoretical and experimental advances improve understanding of retrievals using microwave brightness temperature and extend them to more challenging applications, including sudden atmospheric gradients and slant path delay retrieval for elevation angles as low as 5º.

ACKNOWLEDMENTS

I would like to thank my advisor Prof. Steven C. Reising for his guidance during this research work. Also, I would like to thank Dr. Jothiram Vivekanandan, Prof. Branislav Notaros, and Prof. Steven A. Rutledge for their input to my dissertation and for serving on my committee. I would like to thank Dr. Javier Bosch-Lluis for his important technical ideas and contribution. His support and invaluable feedback throughout the research work performed for this dissertation has been very useful and helpful. I thank Dr. Jothiram Vivekanandan, Prof. Paquita Zuidema and Dr. Scott Ellis for collaborating with us and providing the DYNAMO experiment data and S-PolKa retrieved slant water path and slant liquid water used in this dissertation. I thank my co-workers Scott Nelson and Thaddeus Johnson in the Microwave Systems Laboratory for their contributions and assistance. I would also like to thank Ishan Thakkar for helping us during the HUMEX11 field campaign. Finally, I would like to thank my family and friends for their support and patience.

DEDICATION

To my family for their support.

TABLE OF CONTENTS

LIST OF FIGURES

LIST OF TABLES

LIST OF ACRONYMS

1D-VAR	1-Dimensional Variational Retrieval
ARM	Atmospheric Radiation Measurement
AGL	Above Ground Level
AERI	Atmospheric Emitted Radiance Interferometers
CMR-H	Compact Microwave Radiometer for Humidity Profiling
COARE	Coupled Ocean Atmosphere Research Experiment
CMIS	Conical-Scanning Microwave Imager/Sounder
CSU	Colorado State University
DOF	Degrees of Freedom
DYNAMO	Dynamics of the Madden-Julian Oscillation
DOE	Department of Energy
GPS	Global Positioning Systems
GCMs	General Circulation Models
GN	Gauss-Newton
HUMEX11	HUMidity Experiment 2011
IPT	Integrated Profiling Technique
IWV	Integrated Water Vapor
ILW	Integrated Liquid Water
IF	Intermediate Frequency
LCL	Lifting Condensation Level
LNA	Low Noise Amplifiers

LO	Local Oscillator
LM	Levenberg-Marquardt
MPM	Millimeter Wave Propagation Model
MSL	Microwave Systems Laboratory
MMIC	Monolithic Microwave Integrated Circuit
MJO	Madden-Julian Oscillation
NWP	Numerical Weather Prediction
NOAA	National Oceanic and Atmospheric Administration
NASA	National Aeronautics and Space Administration
NCAR	National Center for Atmospheric Research
NPOESS	National Polar-orbiting Operational Environmental Satellite System
OSSE	Observation System Simulation Experiment
PDF	Probability Density Function
PWV	Precipitable Water Vapor
PPI	Plan Position Indicator
RF	Radio Frequency
RMS	Root Mean Square
RFI	Radio Frequency Interference
SVD	Singular Value Decomposition
SWP	Slant Water Path
SLW	Slant Liquid Water
SPDT	Single-Pole Double-Throw
SGP	Southern Great Plains

TPR	Total Power Radiometer
UNOLS	University National Oceanographic Laboratory System
UM-Radiometer	University of Miami Microwave Radiometer
VLWR	Vapor Liquid Water Ratio
WF	Weighting Function
WRF	Weather Research and Forecasting

Chapter I Introduction

Atmospheric water vapor plays a significant role in weather changes and various atmospheric processes like Earth's energy budget, cloud formation and convective initiation [1] [2]. These processes determine the intensity and location of severe weather. Directly or indirectly water vapor is involved in initiation of severe storms and turbulent weather conditions [1] [3]. Therefore, it is very important to determine water vapor distribution in the troposphere and the physical processes that controlling it. Various observing techniques have been developed that are helping to understand moisture convection interaction and humidity trends [4] [5] [6]. However, the distribution of water vapor in the lower troposphere is still not properly quantified [1] and modeled due to its large spatial and temporal variability. Instruments including microwave radiometers have been used to retrieve atmospheric water vapor and temperature profiles with excellent temporal resolution but varying spatial resolution and accuracy.

1.1. Scientific Motivation

The measurement of water vapor distribution in the lower troposphere is important for numerical weather prediction (NWP) models since water vapor profiles are key inputs for the initialization of these models [7]. Ensemble forecasting of convective initiation is particularly sensitive to the accuracy and spatial resolution of water vapor profiles. This type of forecasting examines forecast variability under a variety of initial conditions to determine where and when severe weather is likely to begin. Severe storms are known to develop within 30 to 60 minutes at locations where water vapor distribution changes rapidly in time [8] [9] [10]. Therefore, tracking dynamic changes in integrated water vapor and water vapor profiles with improved spatial resolution is important to predict the timing and location of cloud formation and the initiation of convective storms.

Water vapor is the only atmospheric constituent that is short lived and abundant in the atmosphere and has a strong positive feedback on climate and weather changes driven by various influences [1]. Thus, information about water vapor and it's variability is very critical. However, study of water vapor until now has not led to precise knowledge of its distribution in the troposphere or clear understanding of the factors controlling water vapor amount and the mechanisms by which it influences atmospheric processes. Therefore, sensing atmospheric water vapor is a major area of interest to National Oceanic and Atmospheric Administration (NOAA), National Aeronautics and Space Administration (NASA), and National Center for Atmospheric Research (NCAR). Consequently, a significant amount of work has been performed to develop systems and techniques for measurement of atmospheric water vapor, as well as to increase the spatial and temporal resolution of observed water vapor density profiles. Some of this work is summarized in the following sections.

1.2. State of the Art for Water Vapor Retrieval

This section describes various retrieval techniques that have been developed and used in the past for estimation of 1-dimensional profiles of water vapor and temperature. The retrieval algorithms used for determination of 2- and 3-dimensional water vapor distribution use tomographic retrieval techniques and have been discussed as follows.

1.2.1 One-Dimensional Water Vapor Profile Retrieval using Ground-Based Radiometers

Retrieval of humidity profiles from passive ground-based radiometers is an *ill-posed* problem [11] because there are a large number of atmospheric states that can produce a given measurement vector within its uncertainty. Various methods have been developed to retrieve 1-D water vapor profiles from radiometer brightness temperature measurements in the last few decades, including statistical profile inversion and the variational method. In statistical profile inversion, a relationship between radiometric measurements and temporally as well as spatially coincident radiosonde profiles is established for a particular area. Using this relationship, measured brightness temperatures are extrapolated to retrieve water vapor and temperature profiles. The problem with this process is the anomalous estimation of profiles having a negative or positive bias.

Therefore, the variational methods of retrieving water vapor and temperature profiles were developed and are known as 1D-VAR [12] and integrated profiling technique (IPT) [13]. This technique uses a forward model to relate the state vector (temperature, water vapor profile and cloud liquid) to the observation vector i.e., brightness temperatures measured at the frequencies channels of operation. The *ill-posed* problem is addressed by the addition of background or *a-priori* data set, sometimes in the form of a short-term forecast from a NWP model. This method also takes into consideration the error due to observations and the variability due to background data set. The optimum profile is retrieved by adjusting the atmospheric state vector in order to minimize a cost function using an optimization method, usually the Gauss-Newton or regularized Levenberg–Marquardt method [14]. 1D-VAR uses the Levenberg–Marquardt optimization method whereas Gauss-Newton method is used by IPT.

As part of 1D-VAR degrees of freedom (DOF) analysis was performed and showed that temperature and water vapor measurement frequencies had DOF of 2.8 and 1.8, respectively. The vertical resolution of temperature profiles degrades from approximately 0.7 km near the ground to 8 km at 4 km altitude while that of humidity profiles detoriates from 2 km at ground level to 7 km at 2 km altitude. An error analysis determined that the 1D-VAR retrieval uncertainties for temperature and water vapor density profiles were 1 K and 2.5 gm^{-3}, respectively [14]. Error analysis for IPT [13] shows that the root mean square (RMS) uncertainties are less than 1 K and 1 gm^{-3} for temperature and humidity, respectively. The relative error for retrieved integrated liquid water ranges from 15% to 25% whereas the bias error for integrated water vapor is approximately 0.013 cm based on comparison with radiosonde launched close to measurement time.

There are various other retrieval algorithms as described by Westwater [15] and Solheim [16] i.e. regularization techniques, iterative techniques, regression methods and *a-priori* linear statistical method with focus on estimation of temperature profiles. The *a-priori* linear statistical method is similar to the 1D-VAR and provides an estimated error of 0.5 to 2 K from ground to 10 km altitude. Solheim compared the performance of different optimization techniques i.e., Gauss-Newton iteration method, regression method, neural network and Bayesian maximum probability estimation technique, for retrieval of water vapor, temperature and liquid water profiles. All the techniques showed temperature errors of approximately of 0 to 4 K while water vapor rms error was in the range of 0 to 2 gm^{-3}. Scheve and Swift [17] compared water vapor profiles retrieved from K-band microwave brightness temperature measurements to those retrieved from Raman lidar measurements [18].

1.2.2 Two-Dimensional Absorption Coefficient Structure using an Elevation Angle Scanning Radiometer

The retrieval of 2-D absorption coefficient structure uses tomographic measurements from a radiometer with a single frequency channel at 23.8 GHz [19] where the radiometer scans a vertical plan of atmosphere using 12 different elevation angles from 23° to 90°. Tomography works best when a lot of elevation angles of measurement are available from multiple perspectives but the number of angular measurements is limited in the 2-D retrieval explained here. The scanned region is modeled as a panel of 9 km height and 23 km horizontal extent. This observed region is subdivided into rectangular bins, as shown in Figure 1. The size of bins is smaller near the radiometer and larger further away from the radiometer. The vertical size of all bins is 1.5 km, while the horizontal sizes of the bins vary from 0.5 km near the radiometer to 6 km furthest away from the radiometer. Solid lines in the figure represent the propagation paths observed by the radiometer antenna at various elevation angles. The number of elevation angles is determined by the eigenstructure of the forward problem as shown by singular value decomposition (SVD) [20]. For each of the 12 elevation angles, the contribution of each bin to the brightness temperature is computed assuming that the medium properties are constant within the bin. Again, the problem is *ill-posed* because the number of measurements is less than the variables. Therefore, a re-parameterization allows the 39 bins to be re-expressed into five macrocells, identified by letters, according to the eigenstructure of the Jacobian matrix. To retrieve the absorption coefficients in each bin, a forward model is defined by linearizing the radiative transfer equation about a reference model, where the difference between the measured and modeled brightness temperature are related to variations in absorption coefficient in each bin by means of a Jacobian matrix. The forward model needs to be inverted and least squares regression method is applied to retrieve the absorption coefficient profiles.

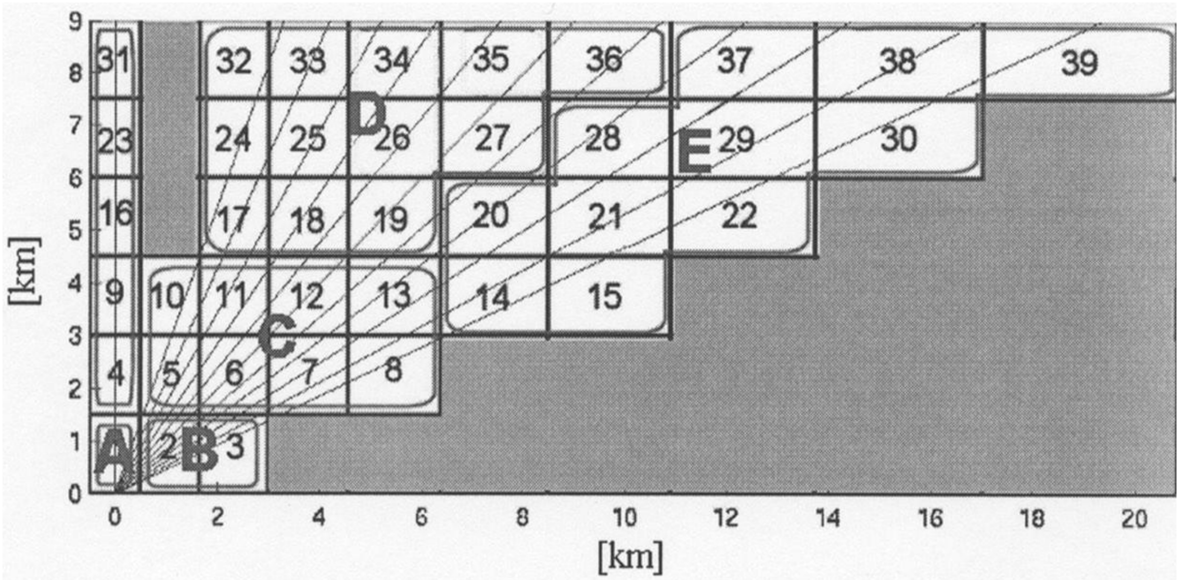

Figure 1. The scanned vertical plane is divided into resolution bins, identified by numbers, each with constant attenuation [19].

1.2.3 Three-Dimensional Water Vapor Field using a Network of Radiometers

Three-dimensional water vapor density is retrieved from brightness temperatures measured by a network of compact microwave radiometer for humidity profiling (CMR-H) [21] designed and fabricated at Microwave Systems Laboratory, Colorado State University. The retrieval algorithm developed by Padmanabhan et al. [5] uses algebraic reconstruction tomography, optimal estimation and Kalman filtering [22]. The network of radiometers performs measurements of the atmosphere at various elevation and azimuth angles. Each vertical plane scanned by the radiometer is divided into grid cells of equal size, as shown in Figure 2. The elevation angles used have minimum redundancy in terms of degrees of freedom and are determined by calculating the number of non-zero eigenvalues of the Jacobian matrix relating the variation of brightness temperatures and absorption coefficients. The number of eigenvalues is equal to the total number of independent ray intersections inside unique grid cells. A water vapor profile from radiosonde is used as an *a-priori* or reference profile. Using the reference atmospheric state, a radiative transfer equation in discrete form is used to calculate the brightness temperature at each measurement frequency and elevation angle. The difference between the measured and simulated brightness temperatures is termed the variation in brightness temperature. The absorption coefficient in each of the grid cells is calculated using Van-Vleck Weisskopf absorption model. The variation of the brightness temperature at each elevation angle and the variation of the absorption coefficient in each grid cell are related by the elements of the Jacobian matrix. Calculating the absorption coefficient from the brightness temperature variation and the Jacobian matrix is an *ill-posed* problem because the number of measurements is less than the number of grid cells at which the absorption coefficient needs to be determined. Therefore, the deviation of each absorption coefficient from its reference value is calculated using Bayesian optimal estimation. The absorption coefficient retrieved in this way for each of the four brightness temperature measurement frequencies is fit to the Van-Vleck Weisskopf model [23] [24] of the water vapor absorption line to retrieve the water vapor density in each of the grid cells. In addition, spatial interpolation i.e., kriging [25] is used to estimate a continuous image of water vapor density at each of the unsampled grids.

The 3-D water vapor is retrieved with a vertical and horizontal resolution of 0.5 km [26]. The temporal resolution of the retrieved water vapor field depends on the time required to scan the spatial volume measured by the three radiometers. An observation system simulation experiment performed using Weather Research and Forecasting (WRF) model data showed that the water vapor density expected percent error was approximately 15-20%.

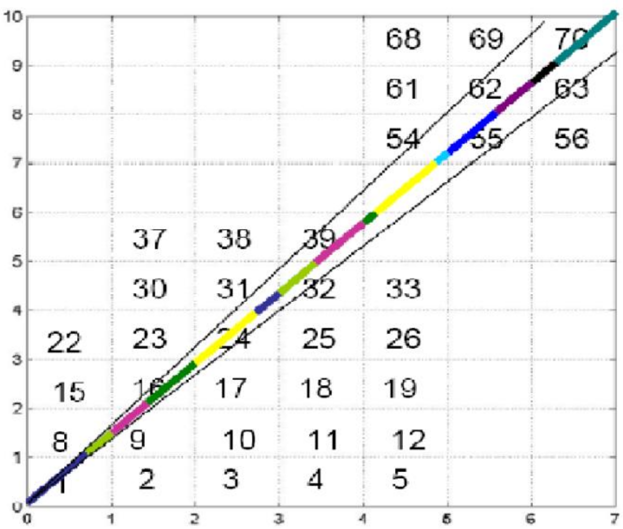

Figure 2. The vertical plane scanned by the radiometer is divided into grid cells to perform the 3-D water vapor retrieval [5].

1.3. State of the Art for Retrieval of Integrated Water Vapor and Liquid Water

There are various retrieval algorithms for estimating integrated water vapor and liquid water in the atmosphere using measured brightness temperatures at two frequencies i.e., frequency near the 22.235-GHz water vapor absorption line and the other is between 29 to 33 GHz, in a window region that is primarily affected by liquid water. These retrieval techniques are broadly divided in to two types. One is site specific and another is site independent, where both are dependent on background statistics.

A) Site-Specific Statistical Retrieval

Retrieval algorithms developed by Liljegren [27] et. al. and Westwater [28] relate the mean radiating temperatures and two-frequency microwave radiometer measurements to the total opacities at those two frequencies. These opacities τ_1 and τ_2 are related to integrated water vapor (IWV) and integrated liquid water (ILW) through a linear relationship using statistically-determined and site-specific retrieval coefficients v_i and l_i which are the path averaged mass absorption coefficient for water vapor and liquid water at the two frequency of operation of the radiometer. Opacities τ_1 and τ_2 are determined using Eqn. (I.1)

$$\tau_i(0,\infty) = ln\left(\frac{T_{mr} - T_b}{T_{mr} - T_{b0}}\right) \tag{I.1}$$

where i determines the frequency index, T_{mr} is the mean radiating temperature, T_{b0} is the cosmic background and T_b is the measured brightness temperature [28]. Opacity is defined as the impenetrability to electromagnetic radiation and is a measure of atmospheric extinction or absorption. The relationship between the opacities and the retrieved IWV and ILW are based on linear regression over a large data set which is usually radiosonde data compiled over a period of a year or more. The regression relationship is shown by Eqns. (I.2) and (I.3)

$$\hat{V} = v_0 + v_1\tau_1 + v_2\tau_2 \tag{I.2}$$

$$\hat{L} = l_0 + l_1\tau_1 + l_2\tau_2 \tag{I.3}$$

where $\hat{V}$ and $\hat{L}$ are the estimated IWV and ILW. The common practice is to calculate the retrieval coefficients and mean radiating temperatures for each of a year so as to take into consideration the annual variation in water vapor and liquid water. This method provides a very good accuracy for integrated water vapor but the estimation method requires regular update of the background data required to calculate the retrieval coefficients, which acts as a limitation. Total water vapor, liquid water and ice content are also being estimated from radiometer measurements using neural network-based inversions, as developed by Li et al. [29].

B) Site-Independent Statistical Retrieval

These retrieval algorithms use surface parameters such as pressure, water vapor partial pressure and temperature to estimate IWV and ILW. In this method the mean radiating temperature $\hat{T}_{mr}$, retrieval coefficients are determined from surface temperature T_{surf}, pressure P_{surf}, relative humidity RH_{surf} and partial pressure e_{sfc} as given by Eqns. (I.4) to (I.7)

$$\hat{T}_{mr} = a + bT_{surf} + cRH_{surf} \tag{I.4}$$

$$\hat{\tau}_{dry} = a + b(P_{surf} - e_{surf})^2/T_{surf} \quad \text{(I.5)}$$

$$\hat{v} = a + bT_{surf} + c_1T_{surf} + c_2T_{surf}^2 + d_1e_{surf} + d_2e_{surf}^2 \quad \text{(I.6)}$$

$$\hat{l} = a + bP_{surf} + cP_{surf}e_{surf} + de_{surf}^2 \quad \text{(I.7)}$$

where $\hat{\tau}_{dry}$ is the dry estimated optical depth, a, b, c, d, c_1, c_2, d_1 and d_2 are the regression parameters and determined using statistical data collected over a long period of time for a number of different places like the southern great plains, Oklahoma, ARM site in Alaska, Coupled Ocean Atmosphere Research Experiment (COARE) and various other field campaigns and radiosonde launch sites. This method [27] performed better than the site specific retrieval algorithm in estimating liquid water and the error was less than 0.05 mm for most of the cases. However, the IWV estimation error was higher for site independent algorithm than the site specific algorithm by approximately 0.2 to 0.3 mm.

1.4 Organization of this Ph.D. Dissertation

This dissertation is organized as follows:

- The fundamentals of remote sensing and radiometry i.e., Planck's Black body radiation, radiative transfer theory and the absorption models used in this dissertation are explained in Chapter II.
- Chapter III describes the Bayesian optimal estimation, Gauss-Newton and Levenberg-Marquardt optimization techniques used for retrieval of water vapor profiles.
- Chapter IV discusses the branch and bound feature selection algorithm which is used for determining the measurement frequencies which provide the most amount of information for water vapor and temperature retrieval. The frequencies selected and the corresponding weighting functions are also presented.

- Chapter V focuses on the HUMidity Experiment 2011 (HUMEX11). Measurements performed during this campaign are used for improving the accuracy of retrieval algorithm. The method of optimization of background data set size for improving ability of retrieval algorithm to detect gradients in water vapor profiles using ground based microwave radiometer measurements is discussed.
- Chapter VI explains the DYNAMO field campaign as well its goals.
- Chapter VII shows and discusses the azimuth anisotropy observed in the measured brightness temperatures at low elevation angles. Also the various sources of the azimuth anisotropy are discussed in this chapter.
- Chapter VIII discusses the sensitivity of vapor liquid water ratio (VLWR) to water vapor and liquid water as well as the retrieval algorithm used for estimation of slant water path and slant liquid water at low elevations. Slant water path (SWP) and slant liquid water (SLW) are compared with those retrieved from radar measurements.
- Chapter IX shows the sensitivity of VLWR to change in elevation angle as well as to changes in precipitation.
- Chapter X describes the conclusions of this research work.

Chapter II Fundamentals of Remote Sensing using Radiometry

This chapter discusses the fundamentals of remote sensing of water vapor and temperature using ground-based and airborne radiometers operating at microwave and millimeter wave frequencies. In this chapter atmospheric radiation and microwave radiometer topologies are introduced and discussed.

2.1. Planck's Blackbody Radiation and Brightness Temperature

An ideal black body is a totally opaque object that absorbs and emits all incident radiation at all frequencies without reflecting any. The characteristics of a perfect black body can be described using the Planck's law [23] and the emitted energy is given as Eqn. (II.1)

$$B_f = \frac{2hf^3}{c^2}\left[1/\left(e^{\frac{hf}{kT}} - 1\right)\right] \tag{II.1}$$

where B_f is the spectral brightness of the blackbody with units of W/(m^{2}SrHz),

- h is the Planck's constant and is equal to 6.626x10^{-34} joules,
- k is Boltzmann's constant and is equal to 1.381x10^{-23} joule/K,
- T is absolute temperature, with units of K,
- f is the frequency in Hz,
- c is the speed of light in $\mathrm{m/s}$.

The brightness calculated using Eqn. (II.1) for a range of frequencies and temperatures are shown in Figure 3. The figure shows that increase in the temperature of a black body leads to increase in amount of radiation emitted by it at a particular frequency. As the temperature is increased, the frequency at which Planck's radiation is maximum also increases. For illustration, a body at 100 K emits maximum radiation at infrared frequencies whereas at 10^9 K the maximum radiation is observed in the gamma ray frequency ranges.

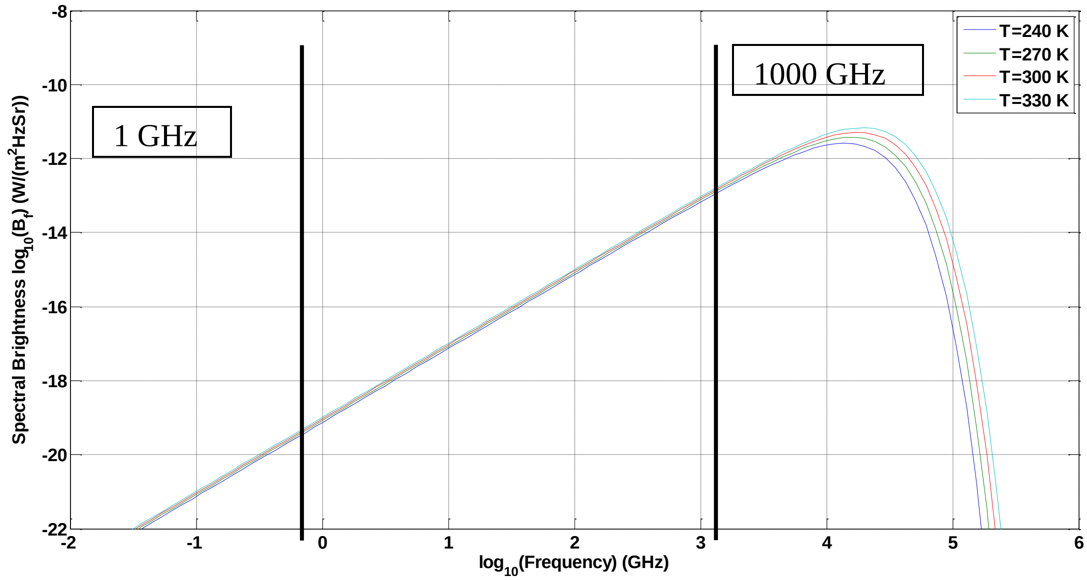

Figure 3. Spectral brightness on a logarithmic plot for a frequency range of 10 MHz to1000 THz according to the Planck law for spectral brightness at four different absolute temperatures with varying frequency [30].

In Figure 3, the spectral brightness is approximately directly proportional to frequency in the 1- 1000 GHz range i.e., 0 to 3 on the log scale. Based on this Rayleigh-Jeans law [23] has been developed for the frequency range 1 to 300 GHz. For this frequency range, the exponential term of Eqn. (II.1) is very small due to which it can be approximated to Eqn. (II.2).

$$\frac{hf}{kT} \ll 1 \tag{II.2}$$

Then, applying the first order Taylor approximation to the exponential in Eqn. (II.1) leads to Eqn. (II.3)

$$e^{\frac{hf}{kT}} - 1 \cong \frac{hf}{kT} \tag{II.3}$$

Therefore, Eqn. (II.1) can be rewritten as in Eqn. (II.4)

$$B_f = \frac{2f^2kT}{c^2} \tag{II.4}$$

This simplified form relates the spectral brightness to physical temperature of the black body and yields brightness values similar to the Planck's law for the frequency range of 1 to 300 GHz. For a black body at a temperature of 300 K, the error in spectral brightness computed using the Raleigh-Jeans approximation instead of Planck's Law is approximately 0.008% at 1 GHz and 2.4% at 300 GHz.

To develop a power-temperature relationship, a lossless antenna is surrounded by a blackbody with a physical temperature of T. The power measured by the antenna [23] is given by Eqn. (II.5)

$$P_{bb} = kT\Delta f \frac{A_r}{\lambda^2} \iint_{4\pi} F_n(\theta, \phi) d\Omega \tag{II.5}$$

where θ is the elevation angle, ϕ is the azimuth angle, $F_n(\theta, \phi)$ is the power normalized antenna pattern, $d\Omega$ is solid angle, A_r is the receiving area of antenna or effective aperture, Δf is the bandwidth of received power and λ is the wavelength of operation of the antenna. The integral in Eqn. (II.5) is the antenna pattern solid angle Ω_p given by Eqn. (II.6)

$$\Omega_p = \iint_{4\pi} F_n(\theta, \phi) d\Omega = \frac{\lambda^2}{A_r} \tag{II.6}$$

Eqn. (II.5) can be simplified to obtain a linear relationship between the physical temperature and the received power, as in Eqn. (II.7)

$$P_{bb} = kT\Delta f \tag{II.7}$$

For a bandwidth of Δf, brightness of a blackbody at particular frequency is given by Eqn. (II.8)

$$B_{bb} = B_f \Delta f = \frac{2kT}{\lambda^2} \Delta f \tag{II.8}$$

In case of a grey body or a non-blackbody, brightness temperature $T_B(\theta, \phi)$ [23] is used to define the direction dependent brightness. It is defined as the temperature a black body in thermal equilibrium with its surroundings would have to represent the observed intensity of a grey body object at a particular frequency. A grey body has a brightness given by Eqn. (II.9)

$$B(\theta,\phi) = \frac{2kT_B(\theta,\phi)}{\lambda^2}\Delta f \tag{II.9}$$

The brightness of the grey and blackbody are related by emissivity as shown in Eqn. (II.10)

$$\mathrm{e} = \frac{B(\theta,\phi)}{B_{bb}} = \frac{T_B}{T} \tag{II.10}$$

The power radiated by an object can be written as a function of its brightness temperature, T_B. Using Eqn. (II.9), one can rewrite the power radiated by an object as a function of its brightness temperature and will be used to derive the radiative transfer function in the next sub-section. However, the power received by the antenna is slightly different than the power emitted by the body. The power received by the antenna has contributions from both the main beam and the side lobes and depends on it's main-beam efficiency. The antenna received power is related to the antenna temperature and is given by Eqn. (II.11)

$$T_A = \eta_m \bar{T}_{ML} + (1-\eta_m)\bar{T}_{SL} \tag{II.11}$$

In this equation, η_m represents the main-beam efficiency of the antenna and in microwave and millimeter wave radiometry is typically greater than 90%. Also, $\bar{T}_{ML}$ represents the apparent temperature of the main-lobe, and $\bar{T}_{SL}$ represents the apparent temperature of the side-lobes.

2.2. Radiative Transfer Equation

The radiative transfer theory [15] describes the intensity of electromagnetic radiation propagating in a medium which absorbs, emits and scatters. In the atmosphere scattering usually occurs during cloudy conditions based on drop-size distribution, and size of the droplets relative to the electromagnetic wavelength. Therefore, it has not been considered while deriving the radiative transfer equation. The starting point of the theory is the description of the radiation field in terms of the specific intensity or brightness I_f. The variation at a point s along a line in the direction of propagation is obtained by considering the sources and sinks of the radiation in a volume element along that line as shown in Figure 4. The loss in brightness due to absorption is given by Eqn. (II.12)

$$dI_f = I_f \alpha ds \tag{II.12}$$

where α is the absorption coefficient of the medium and has units of $\mathrm{nepers/m}$.

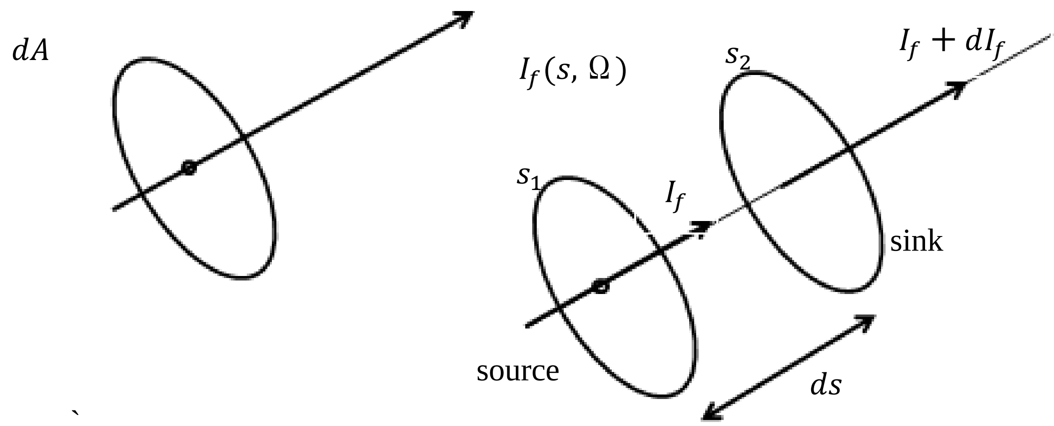

Figure 4. Illustration of radiation in a small region in space [28].

Based on Figure 4 the emission and absorption can be modeled as in Eqn. (II.13)

$$dI_f = (-I_f \alpha + S)ds \tag{II.13}$$

while S is the source that account for emission and absorption. The source can be written as $S = \alpha B_f(T)$ so (II.13) can be rewritten as in Eqns. (II.14) and (II.15)

$$dI_f = (-I_f \alpha + \alpha B_f)ds \tag{II.14}$$

$$\frac{dI_f}{ds} = -I_f \alpha + \alpha B_f \tag{II.15}$$

where $B_f(T)$ has units of brightness and depends on both temperature and frequency while αB_f quantifies the locally generated energy that is added to the radiation due to emission, $I_f \alpha$

quantifies the loss of energy due to absorption and dI_f is the total source due to emission and absorption. Then, Eqn. (II.15) can be rewritten as Eqn. (II.16)

$$\frac{dI_f}{ds} + I_f \alpha = \alpha B_f \tag{II.16}$$

The further simplification of the differential equation done by using the concept of optical depth, τ. This is done by using Eqn. (II.17), where $d\tau$ is an increment of optical depth.

$$d\tau = \alpha ds \tag{II.17}$$

The optical depth, $\tau(s_1, s_2)$, along a path from s_1 to s_2 as shown in Eqn. (II.18)

$$\tau(s_1, s_2) = \int_{s_1}^{s} \alpha ds \tag{II.18}$$

Using Eqns. (II.16), (II.17) and (II.18), it is possible to obtain a solution to the radiative transfer equation by considering the transfer along the path from 0 to a point s' a differential equation of the form shown in Eqn. (II.19)

$$\frac{dB(s')}{d\tau} e^{-\tau(0,s')} + B(s') e^{\tau(0,s')} = S(s') e^{\tau(0,s')} \tag{II.19}$$

After several simplifications and manipulation the solution is shown as Eqn. (II.20)

$$B(s) = B(0) e^{-\tau(0,s)} + \int_0^s \alpha(s') S(s') e^{-\tau(s',s)} ds' \tag{II.20}$$

Applying modified version of Eqn. (II.9) gives Eqn. (II.21)

$$B(s) = \frac{2k}{\lambda^2} T_B(s) \Delta f \tag{II.21}$$

where T_B is the brightness temperature and is related to the energy emitted from a layer of the atmosphere. Additionally, the source function S, can be rewritten using a similar approach. Since the local thermal equilibrium is assumed, the emission must equal the absorption. It is important to point out that these source functions represent an approximation. As such, the source function takes a form similar to $B(s)$.

Using Eqns. (II.20) and (II.21), the brightness temperature is derived as Eqn. (II.22)

$$T_B(s) = T_B(0)e^{-\tau(0,s)} + \int_0^s \alpha(s')T(s')e^{-\tau(s',s)}ds' \quad \text{(II.22)}$$

where $T(s')$ is the physical temperature of the atmospheric layer at height s'.

2.3. Radiometers Topology Overview

A microwave or millimeter-wave radiometer is a passive remote sensing device used for the detection of electromagnetic energy which is noise-like in characteristics. The spatial as well as spectral characteristics of observed energy sources like determine the performance requirements imposed on the functional subsystems of the sensor which include an antenna, receiver, and output indicator. There are various topologies of microwave and millimeter-wave radiometers some of which are explained here.

2.3.1 Total Power Radiometer Topology

A total power radiometer (TPR) is a super heterodyne receiver that has three important parts i.e., radio frequency (RF) section, an intermediate frequency (IF) section, power detector and integrator. The components of the RF and IF section are the antenna, low noise amplifiers (LNA), local oscillator (LO), mixer and intermediate frequency (IF) amplifiers. The block diagram of a typical total power radiometer (TPR) is shown in Figure 5. The RF section amplifies and filters the low-level, wideband noise signal i.e., the antenna temperature, T_A. The output is centered at the RF frequency, f_{RF}. The mixer down converts RF signals to IF signal at the IF frequency, f_{IF} using the local oscillator at a frequency of f_{LO}. The IF amplifier provides further amplification to the signal to reach a detectable level. Afterward, the output of square law detector is a voltage proportional to the amount of power at its input. The output voltage signal of the square law detector has time-varying Gaussian noise fluctuations which are averaged by the integrator over a time period, $\tau_{int.}$ thereby averaging a number of independent samples (equivalent to the time-bandwidth product, $\Delta f \tau_{int.}$) to reduce the effect of the system noise on the desired signal.

The system bandwidth Δf is determined by the IF filter. The antenna temperature is also affected by the receiver noise temperature, T_{rec}. Thus the total system noise temperature by Eqn. (II.23)

$$T_{sys} = T_A + T_{rec} \tag{II.23}$$

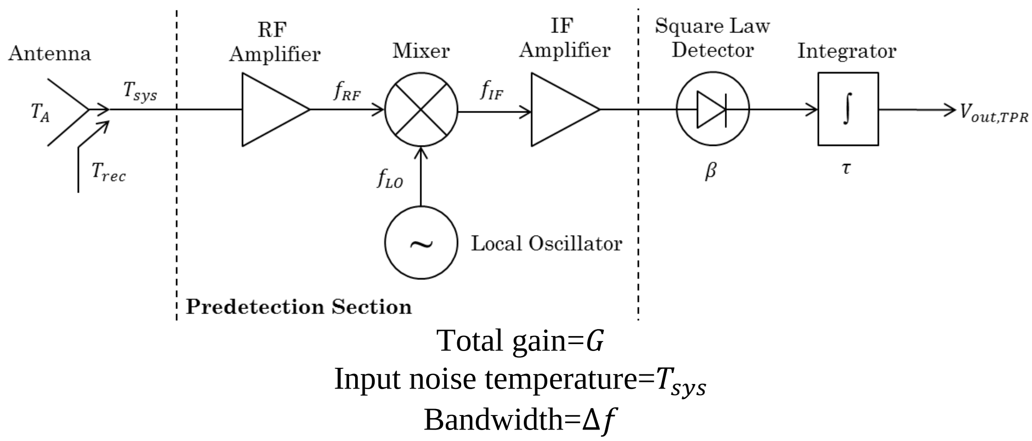

Figure 5: Topology of a total power radiometer.

The total system noise temperature is related to output voltage of an ideal TPR by Eqn. (II.24)

$$V_{out,TPR} = k\Delta f G\beta T_{sys} \tag{II.24}$$

where G is the overall gain of the radiometer, and β is the detector sensitivity with units of V/W. An important parameter is the radiometric resolution defined as the minimum change in antenna noise temperature that produces detectable change in output voltage and is given by Eqn. (II.25).

$$\Delta T_{ideal} = \frac{T_{sys}}{\sqrt{\Delta f \tau_{int}}} \tag{II.25}$$

where τ_{int} is the integration time, ΔT_{ideal} is equal to the standard deviation of the noise fluctuations during the integration time. The expressions in Eqns. (II.24) and (II.25) do not take into account time-varying $1/f$ radiometer gain fluctuations, ΔG. The gain fluctuations affect both the output voltage and radiometric resolution of the radiometer. Taking the gain fluctuations into consideration, the output voltage of a TPR is given by Eqn. (II.26).

$$V_{out,TPR} = kB\beta T_{sys}(G + \Delta G) \tag{II.26}$$

The RMS uncertainty in ΔT_{ideal} due to system gain variations is given by Eqn. (II.27)

$$\Delta T_G = T_{sys}\left(\frac{\Delta G}{G}\right) \tag{II.27}$$

The ideal radiometer resolution and uncertainty due to gain variations are independent of each other and can be related to the total RMS uncertainty given by Eqn. (II.28)

$$\Delta T_{TPR} = \sqrt{(\Delta T_{ideal})^2 + (\Delta T_G)^2} \tag{II.28}$$

This can be rewritten as in Eqn. (II.29)

$$\Delta T_{TPR} = T_{sys}\sqrt{\frac{1}{\Delta f \tau_{int}} + \left(\frac{\Delta G}{G}\right)^2} \tag{II.29}$$

The gain variation has an impact of the sensitivity of the radiometer. One method to reduce gain variation involves changing the architecture of a TPR to that of a Dicke radiometer.

2.3.2 Dicke Radiometer Topology

The gain fluctuation problem with TPR can be reduced by using a Dicke radiometer topology. In this radiometer a single-pole double-throw (SPDT) “Dicke” switch is used before the first LNA. The input of the radiometer is switched rapidly between the antenna temperature, T_A and a matched reference load with equivalent noise temperature, T_{ref}. The switching frequency is chosen such that the gain variations are constant during each switching cycle and hence can be cancelled out. The block diagram for a Dicke radiometer in super-heterodyne configuration is given in Figure 6.

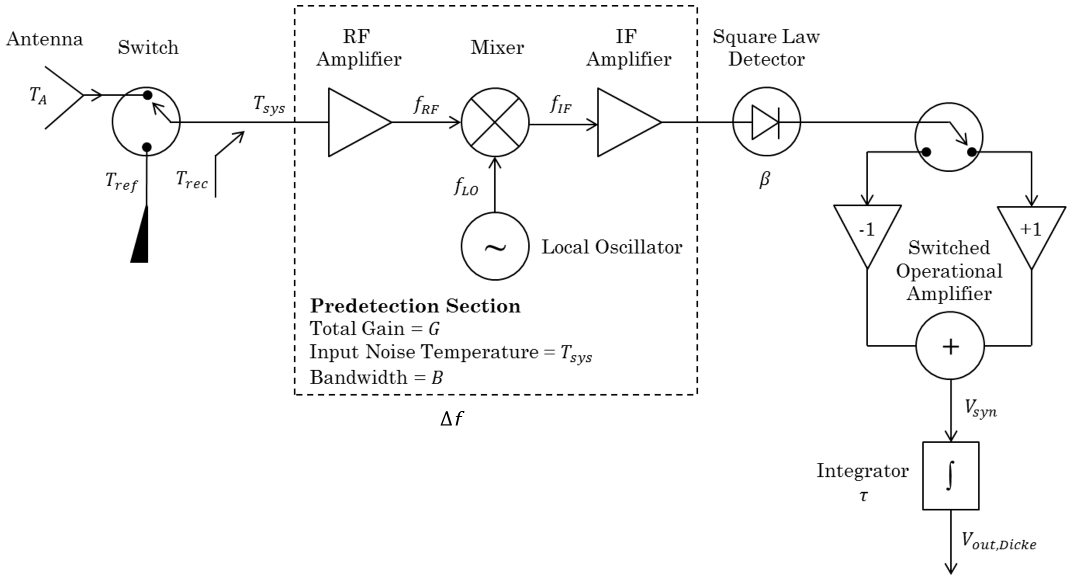

Figure 6: Topology of a Dicke radiometer [23].

An operational amplifier after the square-law detector is switched between inverting and non-inverting modes, as shown in Figure 6. This switching is in synchronization with the Dicke switch at the beginning of the receiver chain. The result is that the antenna signal is input to a positive unity gain amplifier and the reference signal is input to a negative unity gain amplifier. As the input to the receiver is switched to the antenna for half of the time and to the reference matched load for the other half of the time, output voltage of integrator is given by Eqn. (II.30)

$$V_{out,Dicke} = k\Delta f \Delta G\beta\left(T_A - T_{ref}\right) \tag{II.30}$$

Thus, the equivalent receiver noise temperature is cancelled from the output voltage. The uncertainties due to gain variation, reference load and antenna temperature uncertainty are statistically unrelated and hence the resolution of a Dicke radiometer is given in Eqn. (II.31).

$$\Delta T_{out,Dicke} = \sqrt{(\Delta T_{ideal})^2 + \left(\Delta T_{Nref}\right)^2 + (\Delta T_G)^2} \tag{II.31}$$

Eqn. (II.31) can be rewritten as Eqn. (II.32)

$$\Delta T_{out,Dicke} = \left[\frac{2(T_A + T_{rec})^2 + 2(T_{ref} + T_{rec})^2}{\Delta f \tau_{int}} + \left(\frac{\Delta G}{G}\right)^2 (T_A - T_{ref})^2\right]^{1/2} \quad \text{(II.32)}$$

However, the reduction in error in a Dicke radiometer comes at the expense of an degradation in radiometric resolution by a factor of two compared to a TPR for a balanced radiometer when $T_A = T_{ref}$ and neglecting gain variations in the TPR. This factor of two increase for a balanced radiometer, shown in Eqn. (II.32), is the result of a reduction of integration time of the signal of interest by a factor of two due to viewing the scene only half of the time. From a comparison of Eqn. (II.29) to Eqn. (II.32), it appears that the TPR has a better radiometric resolution than a Dicke radiometer; however, since the gain variations increase with longer integration time, the radiometric resolution of a TPR increases much more rapidly with increasing integration time than that of a Dicke radiometer. Difference in the performance of Dicke and TPR is shown in Figure 7. The Dicke radiometer performs better than TPR when gain fluctuations are $3\text{x}10^{-4}$.

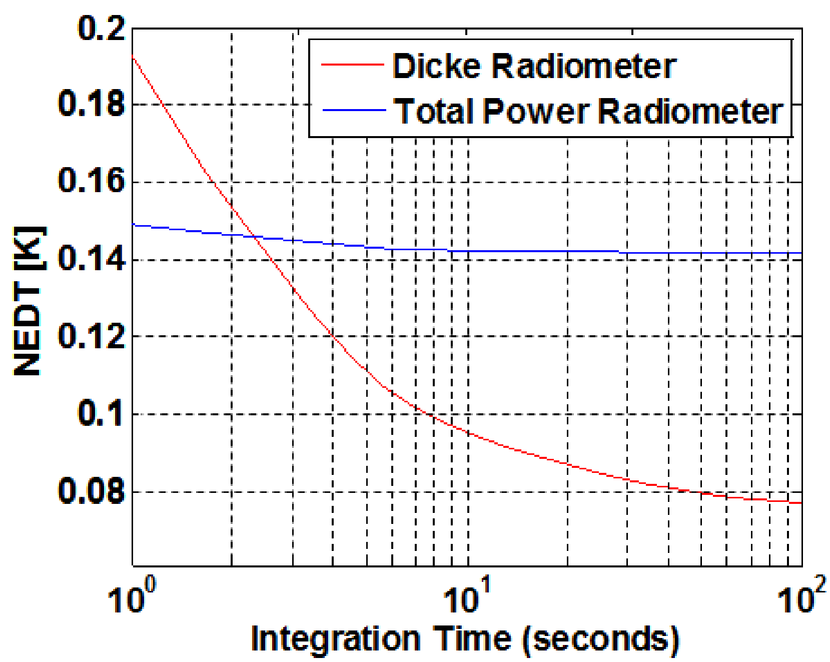

Figure 7. Radiometric resolution of a TPR and a Dicke radiometer for an antenna temperature T_A of 300 K, T_{rec} of 400 K and gain fluctuations, $\Delta G/G$ = $3\text{x}10^{-4}$.

2.3.3 Direct-Detection Radiometers

The previous two sections discussed total power radiometers and Dicke radiometers in a super-heterodyne configuration; however, both types of radiometers can also be implemented in a direct-detection configuration. For both total power radiometers and Dicke radiometers, direct-detection configurations have no down-conversion of the RF signal to an IF signal. The detector diode operates at the RF frequency. Mixers and local oscillators are not needed since down-conversion is not involved.

2.4. Atmospheric Absorption Models

Absorption models play an important role in forward models relating the atmospheric parameter of interest and the measured brightness temperatures. They also describe the absorption as well as emission of electromagnetic radiation by different gases present in the atmosphere. Gases absorb and radiate electromagnetic waves at discrete frequencies, known as absorption line spectra due to transitions between electronic states of atoms as well as due to their vibration and rotation [31]. Emissions due to electronic transition happen in the visible or the ultraviolet region of the spectrum. Emission of energy due to vibration and rotation usually takes place at infrared, millimeter and microwave frequencies. Ideally spectral lines should be infinitesimally sharp but they are not because of the constant motion of the molecules/atoms resulting in the spectral lines being broadened known as line broadening. Pressure broadening is prominent in the lower atmosphere. This broadening of the spectral lines has been used to get information about profiles of water vapor and temperature using microwave and millimeter-wave radiometers measurements at various frequencies. Because of pressure broadening each frequency is sensitive to variation in water vapor at different altitude. In general absorption lines for any gas can be modeled as in Eqn. (II.33)

$$\alpha_{line} = n \sum_i S(f,T)\,F(f) \tag{II.33}$$

where n is the number of molecules per unit volume, $S_f(T)$ is the line strength and depends on temperature as well as frequency while $F(f)$ is the line shape and dependents on frequency.

Water vapor and oxygen are known to be the common absorbing gases in Earth's atmosphere and are the only gases which have absorption lines in the microwave and millimeter-wave frequency range. Their absorption spectrums are calculated using meteorological parameters. Since the proportion of oxygen in the atmosphere is constant in the well-mixed troposphere, the oxygen lines allow the retrieval of atmospheric temperature profiles. The absorption models for these gases have been determined and modified by Liebe and Rosenkranz. The absorption coefficients for water vapor, cloud liquid water and oxygen calculated using the Liebe [32] [33] [34] and Rosenkranz models [31] [35] are shown in Figure 8.

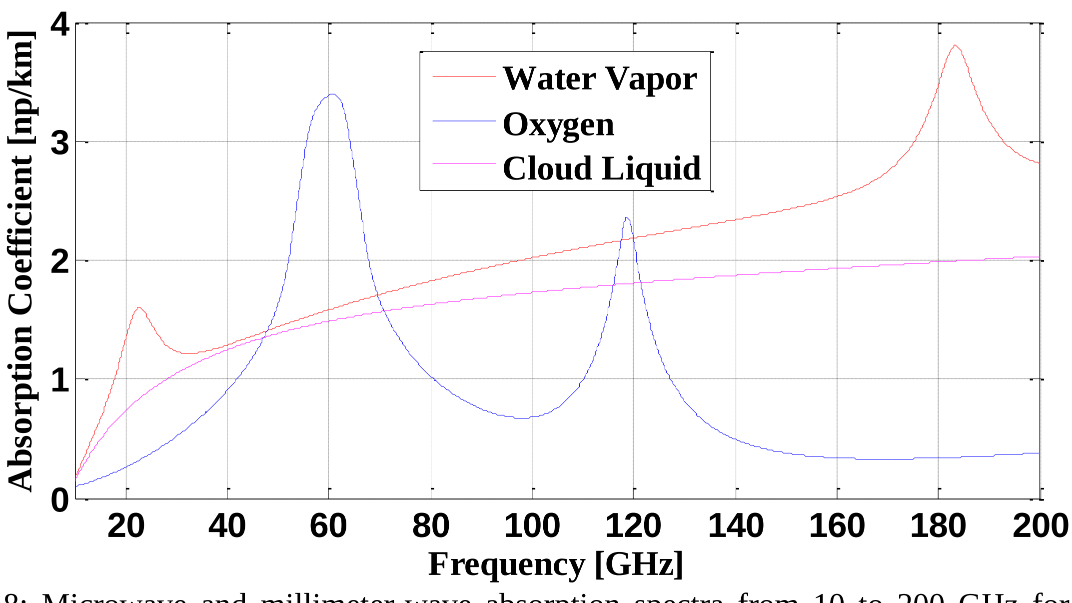

Figure 8: Microwave and millimeter-wave absorption spectra from 10 to 200 GHz for water vapor density of 15.1 gm^{-3}, temperature of 297 K, and cloud liquid water density of 0.1 gm^{-3} [36].

The peaks represent the absorption lines for the water vapor and oxygen models. Frequencies that are sufficiently separated from these absorption lines are considered to be window regions. Brightness temperature measurements near the water vapor resonance frequencies at 22.235 GHz and the window region frequency at 30.0 GHz can be used for simultaneous retrieval of integrated water vapor and liquid water in the atmosphere. Brightness temperature measurements at a number of frequencies near water vapor and oxygen resonance frequencies allow retrieval of atmospheric water vapor content and temperature at a variety of heights due to pressure broadening.

2.4.1 Liebe Absorption Model

Liebe's 1993 Millimeter wave Propagation Model (MPM) [34] which is a modification of the MPM87 [32] describes the absorption spectra of water vapor, dry air (in which oxygen is major contributor) and hydrometeors for a frequency range of 1 to 1000 GHz for non-precipitating conditions. This is done by computing the complex refractivity N given by Eqn. (II.34)

$$N = N_0 + N' + iN'' \quad \text{(II.34)}$$

where $i = \sqrt{-1}$, N_0, N' frequency independent refractive index terms and N'' is the refraction term which depends on frequency and is also the attenuation term quantifying loss of radiation energy, respectively. Refractivity [37] is defined as in Eqn. (II.35)

$$N = 10^6(r_i - 1) \quad \text{(II.35)}$$

where r_i is given as the refractive index. The real and imaginary refractivity terms are related to the attenuation, phase dispersion and the delay rate shown in Eqns. (II.36), (II.37) and (II.38)

$$\alpha = 0.182\, fN'' \text{ dB/km} \quad \text{(II.36)}$$

$$\beta = 1.2008f(N_0 + N') \text{ deg/km} \quad \text{(II.37)}$$

$$\tau_d = 3.3356(N_0 + N') \text{ ps/km} \quad \text{(II.38)}$$

where α, β, τ_d, and f are the absorption coefficient, phase dispersion, delay rate and frequency, respectively. The use of phase dispersion and delay rate has not been discussed in this chapter. The absorption by the atmosphere can be divided into three categories as in Eqn. (II.39)

$$\alpha = \alpha_D + \alpha_V + \alpha_W \qquad \text{(II.39)}$$

where α is the total absorption coefficient, α_D is the dry air component, α_V is the water vapor component and α_W is the component due to liquid water or ice particles in cloud. The dry, wet and liquid components of complex refractivity index are discussed in the following sections.

2.4.1.1 Dry-Air Component

Refractivity of dry air has contributions from frequency independent term, 44 oxygen spectral lines term (resonance spectrum) and non-resonant refractivity of oxygen given by Eqn. (II.40)

$$N_D = N_d + \sum_{k=1}^{44} S_k F_k + N_n \qquad \text{(II.40)}$$

where N_d is the frequency independent term, S_k is the line strength, F_k is the complex line shape function for oxygen, k is the line index with values from 1 to 44 and N_n is the non-resonant refractivity. The line shape of a gas describes the shape of the absorption spectrum with respect to the resonance frequency while the line strength is determined by the physical temperature of gas, number density of absorbing molecules. The frequency independent term is given by Eqn. (II.41)

$$N_d = 0.2588 p_d \theta_t \qquad \text{(II.41)}$$

where p_d is the partial pressure [38] of dry air in millibars and θ_t is defined as the ratio $300/(T + 273)$, T being the ambient temperature in Celsius. The non-resonant oxygen spectrum and the nitrogen absorption line are given by Eqn. (II.42)

$$N_n = S_o F_o(f) + i S_n F_n(f) \qquad \text{(II.42)}$$

where $i = \sqrt{-1}$, S_o is the line strength and F_o is the shape function for non-resonant oxygen frequencies while S_n is the line strength and F_n is the shape function for nitrogen.

2.4.1.2 Water-Vapor Component

Refractivity due to water vapor contains the contributions from 34 H_2O resonance lines spectrum as well as the 10 H_2O continuum spectrum and is given by Eqn. (II.43)

$$N_V = N_f + \sum_{l=1}^{34} S_l F_l + N_c \tag{II.43}$$

N_f is the frequency independent term, S_l is the line strength, F_k is the complex shape function for water vapor and l is the line index. N_c is contributions from the continuum spectrum. The non-dispersive term is given as in Eqn. (II.44)

$$N_f = (4.163\theta + 0.239)e\theta_t \tag{II.44}$$

where $e = (ue_s)/100$ e_s is saturation pressure [39] and u is relative humidity [39].

The contributions to the refractivity in the window region frequency ranges are due to strong lines centered in the rotational water vapor spectrum above the one TeraHertz frequency and are known as the water vapor continuum.

2.4.1.3 Cloud or Fog Component

Cloud liquid, fog and ice contribute towards absorption of radiation where the size of the hydrometeor is less than 50 μm. The refractivity is given by Eqn. (II.45)

$$N_W = 1.5\left(\frac{w}{m_{w,i}}\right)\left[\frac{\epsilon_{w,i}-1}{\epsilon_{w,i}+2}\right] \tag{II.45}$$

where, $m_{w,i}$=1 (for water) and 0.916 g/cm^3 (for ice) and $\epsilon_{w,i}$ is the complex permittivity due to water and ice, w is the density of water or ice.

A) Complex Permittivity Data for Water

The relative dielectric constant of water is known as complex permittivity given by Eqn. (II.46)

$$\epsilon_{w,i} = \epsilon' + i\epsilon'' \tag{II.46}$$

where ϵ' and ϵ'' are the real and loss terms. $\epsilon_{w,i}$ values depend on temperature T and frequency f which provide information about the interaction mechanism between liquid water and electromagnetic waves. The single Debye relaxation model describes the permittivity spectrum of liquid water using three temperature-dependent parameters below 100 GHz. At higher frequencies, additional relaxation and resonance terms are used for frequencies 100 – 1000 GHz which is known as the double Debye relaxation [33].

i) Single Debye Model

The single Debye model provides a description of spectral permittivity for frequencies below 100 GHz. The single Debye model for the dielectric constant of water is given by Eqn. (II.47)

$$\epsilon_D(f) = \frac{(\epsilon_o - \epsilon_\infty)}{\left[1 - i\left(\frac{f}{\gamma_D}\right)\right]} + \epsilon_\infty \tag{II.47}$$

where ϵ_o is the static dielectric constant of pure water given by Eqn. (II.48)

$$\epsilon_o(T) = 77.66 - 103.3\theta_{\mathrm{t}} \tag{II.48}$$

and ϵ_∞, relaxation frequency γ_D are given by Eqns. (II.49) and (II.50)

$$\epsilon_\infty = 0.066\epsilon_o \tag{II.49}$$

$$\gamma_D = 20.27 + 146.5\theta_{\mathrm{t}} + 314\theta_t^2 \tag{II.50}$$

ii) Double Debye Model

On using frequencies above 100 GHz the Debye parameters also change as given by Eqn. (II.51)

$$\epsilon_M(f) = \frac{(\epsilon_o - \epsilon_1)}{\left[1 - i\left(\frac{f}{\gamma_1}\right)\right]} + \frac{(\epsilon_1 - \epsilon_2)}{\left[1 - i\left(\frac{f}{\gamma_2}\right)\right]} + \epsilon_2 \tag{II.51}$$

where $\epsilon_1 = 0.0671\epsilon_o$, primary relaxation frequency $\gamma_1 = 20.2 + 146.4\theta_t + 316\theta_t^2$, secondary relaxation frequency $\gamma_2 = 39.8\gamma_1$ and $\epsilon_2 = 3.52 + 7.52\theta_t$. The real and imaginary parts of permittivity are shown in Figure 9.

B) Complex Permittivity Data for Ice

Permittivity model of ice is given by Eqn. (II.52)

$$\epsilon_i = 3.15 + i(a_i/f + b_i/f) \tag{II.52}$$

where a_i and b_i are temperature dependent empirically computed coefficients.

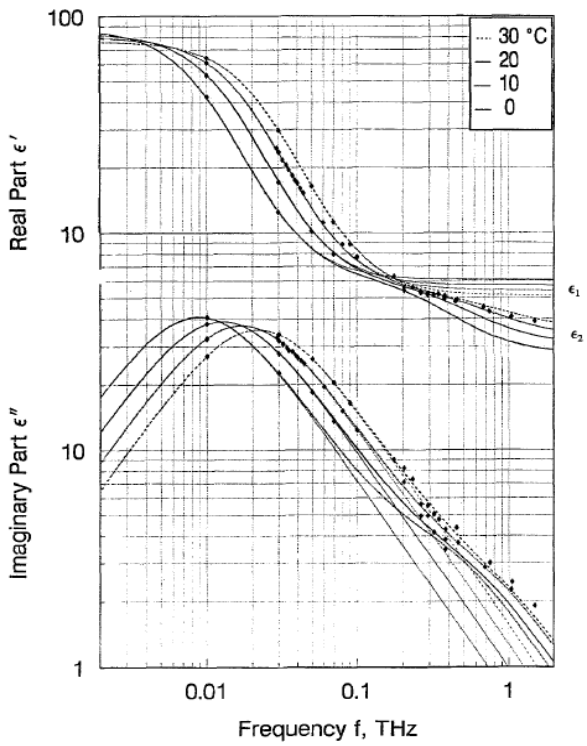

Figure 9. Real and imaginary parts of permittivity of water from 2 GHz to 2 THz [33].

2.4.2 Rosenkranz absorption Model

Rosenkranz worked on determining and improving the absorption models for ozone, water vapor, carbon monoxide, carbon dioxide, nitrogen and oxygen [31] [35]. In this dissertation, Rosenkranz water vapor absorption model has been used extensively so it is discussed in particular. Based on previous research work by Liebe and Van Vleck [40] water vapor absorption models had discrepancies which are attributed to the water vapor continnum i.e., contribution to the absorption line strength in the microwave and millimeter-wave frequency range due to absorption lines in the infrared frequency range. Rosenkranz [35] improved the water vapor continuum values by combination of MPM87's foreign broadened component (contribution from infrared frequencies) which depends on water vapor partial pressure, and MPM93's self-broadened component. This is an empirical method and based on that the foreign- and self- broadened parts of the water vapor continuum were increased by 15% and 3%, respectively. The absorption coefficients are calculated using Eqn. (II.33), absorption line strength for resonance frequencies given in [31] and the line shape $F_i(f)$ given by Eqn. (II.53)

$$F_i(v) = \begin{cases} \left(f^2\gamma h_i/\pi f_i^{\,2}\right)\left\{\left[(f-f_i)^2+\gamma h_i^{\,2}\right]^{-1}-\left[f_c^{\,2}+\gamma h_i^{\,2}\right]^{-1}\right\}, & |f-f_i|<f_c \\ 0, & |f-f_i|\geq f_c \end{cases} \tag{II.53}$$

where f_c is the line center frequency and γh_i is the line half width calculated as in Eqn. (II.54)

$$\gamma h = w_s p_{H_2O}\theta^{x_s} + w_f p_d \theta^{x_f} \tag{II.54}$$

where p_d is partial pressure of dry air p_{H_2O} is the partial pressure of water vapor, w_s, w_f, x_s and x_f are constant coefficients determined empirically.

To calculate the contributions towards the continuum from infrared absorption lines Rosenkranz used contributions from the frequency range of 0 to 750 GHz as lines higher than 750 GHz have minimal impact. Using both the absorption lines and the continuum the absorption coefficient [35] of water vapor is given by Eqn. (II.55)

$$\alpha = \alpha_{line} + f^2\theta^3\left(C_f p_d p_{H_2O} + C_s p_{H_2O}^2\right) \tag{II.55}$$

where, C_f is a coefficient which is dependent on temperature and frequency. This model was found to give better results than MPM model for water vapor.

2.5. Conclusions

This chapter analyses the radiative transfer theory which is usually used as the forward model in the retrieval algorithms used for estimation of water vapor and temperature profiles as well as the retrieval of integrated water vapor and liquid water. In addition, the two most common types of radiometer topologies are explained. Dicke radiometers are widely used for water vapor and temperature remote sensing because of their stable performance. The commonly used absorption models in remote sensing i.e., Leibe and Rosenkranz models are also discussed.

Chapter III Water Vapor and Temperature Profile Retrieval Algorithms

Estimation of profiles of atmospheric parameters like water vapor and temperature using microwave radiometer measurements require the use of a linear/non-linear retrieval algorithm. This chapter discusses the various types of retrieval algorithms, particularly the Bayesian optimal estimation technique used for estimation of atmospheric parameters. Furthermore, the various sources of information for profile retrieval algorithms are discussed.

3.1. Sources of Information for Retrieval Algorithms

In a general sense, the retrieval process performs a mapping between the measurement space and the retrieval solution space according to a probabilistic model in the presence of uncertainties like radiometric measurement noise, model inaccuracies and representativeness errors [11]. Retrieval algorithms use four information sources [41] [13] [28] for estimating profiles of water vapor and temperature i.e., measured brightness temperatures ($\bar{T}_B$), background data set covariance matrix ($\bar{\bar{S}}_a$), measurement error covariance matrix ($\bar{\bar{S}}_\varepsilon$) [11] and weighting function matrix also known as Jacobian ($\bar{\bar{K}}$) [12] [41].

The brightness temperature vector contains radiometric measurements performed at multiple frequencies. These measurements contribute information towards profile retrieval [36], although at some frequencies the information they provide can be highly correlated with that at other frequencies due to similar sensitivities to changes in atmospheric pressure, temperature and water vapor mixing ratio as a function of altitude.

The uncertainties associated with the retrieval can be overcome by knowledge of variability (statistics) of the parameters in the solution space. Background information covariance matrix describes the statistical variability of measured profiles over the time period during which they were measured. It is calculated using a background data set, i.e. a collection of profiles measured over a certain period of time at a specific location [41]. The number of elements in the background data set and the relationships among them determine the values of the matrix elements, depending on the period of the day, in the same or different seasons.

Measurement error covariance matrix includes the noise in radiometric observations, representativeness error and the radiative transfer model errors [11]. Noise in radiometric observations is related to the sensitivity of the instrument, radiative transfer model errors are due to the errors in the model and representativeness error is due to the atmospheric variability over a certain period of time. Usually measurements at each of the frequencies of operation are assumed to be independent of each other, so the off-diagonal elements are assumed to be zero [13].

The Jacobian is the sensitivity of the measured brightness temperatures to changes in atmospheric water vapor as a function of altitude above ground level [28]. Jacobian depends on the operating frequency of each of the microwave radiometer channels and on the water vapor content and temperature of the atmosphere.

3.1.1 Radiometric Measurements and Information Content

Brightness temperature measurements at various microwave frequencies provide information about the state of the atmospheric parameter of interest. For example, measurements near the weak water vapor absorption lines i.e., frequency range of 18-26 GHz [42] [36] and strong water vapor absorption lines i.e., frequency range of 168-192 GHz [42] [43] [36] provide information about the distribution of water vapor while the measurements near the oxygen complex i.e., the frequency range of 50-60 GHz provide information about the temperature profile of the atmosphere [16] [36]. However, these measurements could have a high degree of redundancy depending on the frequencies of operation. Providing redundant measurements to retrieval will increase the amount of noise in the retrieval depending on how they are used. The goal for profile retrieval is to obtain as many independent measurements as possible, both to maximize the vertical resolution and to minimize the retrieval error of the profile. Achieving a maximum amount of independent pieces of information is more complex than just adding as many frequency channels measurements as possible and requires a selection process for determining the best frequency channels [36].

3.1.2 Sources of Initialization Profile and Background Information

Water vapor profiles from various sources can be used as initialization profiles and background data, including in-situ measurements from radiosondes and remote sensing measurements from Raman lidar, both of which have high vertical resolution. Other potential sources of background data are statistical data sets and weather prediction model output compiled over a long time period, i.e., 1-3 years [28].

Radiosonde data have a typical vertical resolution of 10 m and therefore can detect fine gradients in water vapor and temperature profiles in the lower troposphere. Humidity biases in radiosonde measurements are often greater than 5% throughout the troposphere. Residual dry bias errors are greater during the day than the night by 5%–7% [44]. The radiosonde balloon typically takes 25 to 40 minutes to reach a height of 15-20 km above ground level (AGL) and may drift horizontally up to tens of km from the launch site, depending on the local wind speed and direction as it ascends [5]. On the other hand, Raman lidar measurements have a vertical resolution of 35 m from 0 to 0.2 km, 39 m from 0.2 to 3.7 km and 78 m from 3.7 to 6 km AGL with a temporal resolution of 10 minutes [45]. The relative humidity error in Raman lidar profiles is less than 10% for altitudes below 8.5 km AGL [18].

The background data set for profile retrieval from radiometer measurements is typically high-vertical resolution radiosonde or remote sensing measurements over a time period of 2-3 years [28]. Background data sets are used to derive the statistics of profile variability, and their usefulness and applicability to retrievals depend upon the location at which and the time of the year during which they were taken.

Finally, numerical weather prediction model outputs are another potential source of background data. However, their spatial and temporal resolution may not be sufficiently fine to detect changes or sharp gradients in water vapor profiles.

3.1.3 Background Information Covariance Matrix

The Bayesian retrieval technique uses background statistics of the solution space to invert the measurement and retrieve the most probable solution, as illustrated by Cimini et al. [43] and Hewison [12] while using the 1D-VAR technique. The quality of retrieved profiles depends on the atmospheric background information covariance matrix [41]. Therefore, the size and content of the background data set from which the covariance matrix is calculated is very important. If each element in the data set is a sample of the same stationary process [46], the joint probability distribution of the atmospheric layers remains constant in time. Therefore, the mean and covariance of each layer do not change depending on the size of the background data set. Typically, the background data set is filtered based on location, season and time of day to ensure its stationarity [46]. Due to the central limit theorem, as data set size increases, the background data set becomes a normally distributed random process describing a “mean” atmospheric behavior. Failing to achieve stationarity introduces error in the retrieval since the prior statistics are not consistent with the atmospheric conditions at the time of the radiometer measurement and therefore will bias the retrievals [41].

Using a large background data set to determine the background information covariance matrix improves the representation of the higher-order atmospheric statistics, which helps to improve the accuracy of retrieved water vapor profiles but decreases the capability of retrieving or predicting singular or so-called “outlier” events. This happens because the covariance matrix is general and therefore not “customized” for any particular atmospheric condition. The retrieval error approaches a constant value, but gradients or inversions in water vapor profiles will be difficult to detect with high accuracy since the covariance matrix describes the variability of water vapor profiles during the entire time period represented by the background data set. Therefore, both the content and size of the background data set are very important for the retrieval.

When the background covariance matrix is optimized, it will not be general but instead will be particular to the current retrieval and will satisfy the requirement for stationarity, in the sense of a particular state of the atmosphere. Since the particular background data set does not describe every atmospheric condition, the retrieval performance is expected to degrade as a function of time between the initialization and the retrieval.

However, a small background data set (less than approximately 10 profiles) will not be able to describe the atmosphere accurately enough since statistical information will not be significant. Taking this into consideration, it is reasonable to expect that the choice of optimum background data set size will be one of the major factors of the ability to detect evolving changes and gradients in water vapor profiles.

The size of the background data set can be chosen based on the application. If the application is to monitor dynamic changes in water vapor profiles, an optimum data set can be chosen to correspond to recent weather conditions. Instead, if the application requires water vapor profiles with statistical or seasonal accuracy, a large background data set can be chosen, often collected over many months or years [28].

3.2. Retrieval algorithms for Inverse Problems

Retrieval algorithms for inverse problems can be categorized as linear, nearly linear, moderately non-linear and grossly non-linear. They are defined as

a) Linear: Usually linear inverse problems can be represented and solved by using the forward model $\bar{y} = \bar{\bar{K}}\bar{x}$. The *a-priori*, measurements and the state vector for linear problems are assumed to be Gaussian [14].

b) Nearly linear: These inverse problems are non-linear, but linearization about some prior state can be used to find a possible solution.

c) Moderately non-linear: In this case linearization can be used for error analysis but not for finding a solution.

d) Grossly non-linear: For these problems linearization cannot be used for finding the solution or even for error analysis.

3.2.1 Determination of Degree of Nonlinearity

The non-linearity for an inverse problem can be tested by comparing the forward model with the linearized forward model as in Eqn. (III.1) [14]. The problem is linear if the difference is within the *a-priori* variability as given by

$$\delta\hat{\rho} = \bar{\bar{G}}\left([\bar{T}_B(\hat{\bar{\rho}}) - \bar{T}_B(\bar{\rho}_a)] - \bar{\bar{K}}[\hat{\bar{\rho}} - \bar{\rho}_a]\right) \tag{III.1}$$

where $\bar{\bar{G}}$ is the gain function, $\hat{\bar{\rho}}$ is the estimated water vapor profile, $\bar{T}_B$ is the brightness temperature vector as function of water vapor profile and $\bar{\rho}_a$ is the *a-priori* profile. The problem is non-linear if the difference is within the solution error covariance as given by Eqn. (III.2) [14]

$$\delta\hat{\rho} = \bar{\bar{G}}\left([\bar{\mathrm{T}}_{\mathrm{B}}(\hat{\rho}) - \bar{\mathrm{T}}_{\mathrm{B}}(\bar{\rho})] - \bar{\bar{K}}[\hat{\rho} - \bar{\rho})]\right) \tag{III.2}$$

After the determination of non-linearity, respective solutions are applied. Generally, remote sensing inverse problems are either moderately or highly non-linear. The rest of this section discusses the solution process for a non-linear problem.

3.2.2 Bayesian Optimal Estimation

Usually, remote sensing problems are *ill-posed* inverse problems [14] [12] because the atmospheric state vector $\bar{x}$ to be retrieved has more elements than the measurements in vector $\bar{y}$ where the relation between measurement and state vector is given by Eqn. (III.3).

$$\bar{y} = F(\bar{x}) + \bar{\varepsilon} \tag{III.3}$$

where $F(x)$ is the forward model and $\bar{\varepsilon}$ is the observation error.

As already stated these measurements can be correlated to each other due to which the problem becomes more difficult. Consequently, a large number of possible solutions to the state vector exist which satisfy the measurements. Therefore, to constraint the number of possible solutions additional information is required in the form of initialization profile or *a-priori* and background information covariance matrix. The *a-priori* information is observation of the state vector prior to the measurement. For water vapor and temperature profile retrieval, it is usually data taken from radiosonde launched a few hours before the radiometer performs the measurement. Background information covariance matrix on the other hand, provides a measure of the variability associated with water vapor or temperature profiles during the entire time period represented by the background data set.

To map the measurement space to the state space in the presence of *a-priori* information, Bayes' theorem can be used. The probability density function (PDF) of all possible solutions $\bar{x}$ given the measurement $\bar{y}$ is shown in Eqn. (III.4) [14]

$$P(\bar{x}|\bar{y}) = \frac{P(\bar{y}|\bar{x})P(\bar{x})}{P(\bar{y})} \tag{III.4}$$

where

- $P(\bar{x})$ and $P(\bar{y})$ are the PDF of the state vector (*a-priori* knowledge) and the measurement, respectively
- $P(\bar{y}|\bar{x})$ is the conditional PDF of $\bar{y}$ given $\bar{x}$, which provides the knowledge of the forward model and the measurement error
- $P(\bar{x}|\bar{y})$ is the resulting improvement in the *a-priori* knowledge $\bar{x}$, because of combination with the measurement vector $\bar{y}$. It shows the set of possible solutions to the inverse problem and is not the exact solution.

Bayes' theorem can be used to derive the Bayesian optimal estimation method under the assumption that the PDF of measurements and state vector are Gaussian. Like any retrieval algorithm, the error characteristics of the measurements and the forward model should be as low as possible and must be accurately described by covariance matrices. The measurements with small errors and/or an accurate description of the relation between measurement and parameter will have a higher weight in the solution than measurements with large errors and/or an inaccurate description of the relationship between measurement and parameter. If the forward model is moderately non-linear, it can be simplified to a linear problem by means of a Taylor series expansion about an initial state vector $\bar{x}_i$. If higher terms are omitted, $\bar{y}$ can then be expressed by Eqn. (III.5) [14]

$$\bar{y} - \bar{y}_i = \bar{\bar{K}}_\iota(\bar{x} - \bar{x}_i) \tag{III.5}$$

where $\bar{\bar{K}}_\iota$ is the Jacobian matrix of the problem or weighting function [28].

The retrieval of water vapor and temperature profiles are non-linear problems. Therefore, only numerical optimization methods can be used for determining the maximum *a-posteriori* solution (MAP).

3.2.3 Maximum *a Posteriori* Solution

Bayesian optimal estimation is used to solve inverse problems by determining:

a) Posterior PDF of the state vector, which are the most likely state for which $P(\bar{x}|\bar{y})$ is maximum given by MAP or the expected value of the state i.e. the state averaged over the PDF given by Eqn. (III.6):

$$\hat{\bar{x}} = \int \bar{x}P(\bar{x}|\bar{y})dx \tag{III.6}$$

b) Together with the second moment matrix as a measure of the width of the distribution/PDF or the uncertainty of the solution. The error analysis can done using the measurement error and the modelling error.

Linear problems with measurements and *a-priori* having Gaussian distribution the expected value of the state and most likely state are identical because of the symmetry of the PDF. The MAP solution is also known as most likelihood (ML) solution. For non-Gaussian statistics the MAP and expected value solutions will provide different solutions. In these circumstances the covariance matrices are not an adequate description of uncertainty and higher order moments of the PDF are needed. Numerical methods are required to find the MAP solution in case of non-linear and non-gaussian statistics. Some of the numerical methods are Gauss-Newton and Levenberg-Marquardt optimization methods.

3.2.4 Gauss-Newton Optimization Method

If the retrieval problem is slightly non-linear, Gauss-Newton (GN) retrieval method can be used. The GN iteration is given by Eqn. (III.7) [14] [13]

$$\bar{\rho}_{i+1} = \bar{\rho}_i + \left(\bar{\bar{S}}_a^{-1} + \bar{\bar{K}}_i^{\ T}\bar{\bar{S}}_\varepsilon^{-1}\bar{\bar{K}}_i\right)^{-1}\left(\bar{\bar{K}}_i^{\ T}\bar{\bar{S}}_\varepsilon^{-1}\left[\bar{T}_B{}' - \bar{T}_B(\bar{\rho}_i)\right] - \bar{\bar{S}}_a^{-1}[\bar{\rho}_i - \bar{\rho}_a]\right) \tag{III.7}$$

where

- i is the index of iteration
- $\bar{\bar{K}}_i$ is the kernel function or the weighting function matrix
- ρ is the water vapor density profile, where $\bar{\rho}_i$ is the initialization water vapor density profile when $i = 1$, and $\bar{T}_B'$ is the measured brightness temperature vector
- $\bar{\rho}_a$ is the background profile and is same as the initialization profile. For a small background data set, a radiosonde profile taken close to the measurement time is used as the initialization profile while for a large background data set mean profile is used as initialization profile
- $\bar{T}_B$ is the vector of brightness temperature simulated using a radiative transfer model for the frequencies of operation of a radiometer
- $\bar{\bar{S}}_\varepsilon$ is the measurement error covariance matrix, where the main diagonal elements are determined by the radiometric resolution of each channel [47]. Usually measurements at each of the frequencies of operation are assumed to be independent of each other, so the off-diagonal elements are assumed to be zero. $\bar{\bar{S}}_\varepsilon$ also includes the noise in radiometric observations, representativeness error and the radiative transfer model errors
- $\bar{\bar{S}}_a$ is the background information covariance matrix, with dimensions depending on the number of atmospheric layers used for the retrieval and with values based on the statistics of the background data set profiles

The final output profile is chosen based on the convergence criterion given by Eqn. (III.8) [14]

$$[\bar{T}_B(\bar{\rho}_{i+1}) - \bar{T}_B(\bar{\rho}_i)]^{\ T}\bar{\bar{S}}_{\delta y}^{-1}[\bar{T}_B(\bar{\rho}_{i+1}) - \bar{T}_B(\bar{\rho}_i)] << m \tag{III.8}$$

where m is the number of measurements and $\bar{\bar{S}}_{\delta y}$ is the covariance between $\bar{T}_B'$ and $\bar{T}_B(\bar{\rho}_i)$. The iteration stops when Eqn. (III.8) reaches a value which is significantly less than m and the resulting profiles are checked for consistency.

3.2.5 Levenberg-Marquardt Optimization Method

GN method works well when the *a-priori* for the problem is in a region sufficiently close to the solution so that the second-order derivative of the cost function is small. If the *a-priori* is not close to the solution region, then the Levenberg-Marquardt (LM) method is used. The LM method is used as a trust-region method [12].

LM is an iterative, non-linear optimization algorithm, similar to the Gauss-Newton (GN) algorithm but with better performance for highly non-linear problems. The main difference between LM and GN is that LM has a damping parameter γ that is updated during each iteration based on the ratio of the actual value of the cost function to that when the problem was considered to be linear. The LM algorithm usually converges within 15 - 20 iterations similar to GN technique and is defined by Eqn. (III.9) [14] [12] [43]

$$\bar{\rho}_{i+1} = \bar{\rho}_i + \left((1+\gamma)\bar{\bar{S}}_a^{-1} + \bar{\bar{K}}_i^{\,T}\bar{\bar{S}}_\varepsilon^{-1}\bar{\bar{K}}_i\right)^{-1}\left(\bar{\bar{K}}_i^{\,T}\bar{\bar{S}}_\varepsilon^{-1}\left[\bar{T}_B{}' - \bar{T}_B(\bar{\rho}_i)\right] - \bar{\bar{S}}_a^{-1}[\bar{\rho}_i - \bar{\rho}_a]\right) \qquad \text{(III.9)}$$

where γ is the LM factor.

LM is an iterative process in which the value of γ is chosen to minimize a cost function, J where m is the number of measurements and $\bar{\bar{S}}_{\delta y}$ is the covariance between $\bar{T}_{\mathrm{B}}'$ and $\bar{T}_B(\bar{\rho}_i)$. The iteration stops when Eqn. (III.8) reaches a value which is significantly less than m, and the resulting profiles are checked for consistency using cost function as in Eqn. (III.10)

$$J = (\bar{\rho} - \bar{\rho}^b)^T\bar{\bar{S}}_a^{-1}(\bar{\rho} - \bar{\rho}^b) + (\bar{T}_B(\bar{\rho}_i) - \bar{T}_B')^T\bar{\bar{S}}_\varepsilon^{-1}(\bar{T}_B(\bar{\rho}_i) - \bar{T}_B') \qquad \text{(III.10)}$$

where $\bar{\rho}$ and $\bar{\rho}^b$ are the water vapor profile outputs for each iteration and initialization profile, respectively.

3.3. Conclusions

This chapter discusses the various retrieval algorithms and the information sources for them. The characteristics and function of each information source is also described. The Bayesian optimal estimation along with the GN and LM optimization methods is discussed which will be used extensively in later chapters.

Chapter IV Radiometric Information Content for Water Vapor and Temperature Profiling

The goal of this chapter is to determine sets of frequencies in the 10 to 200 GHz range that provide the largest amount of mutually independent information on water vapor and temperature profiles from ground and airborne instruments for clear sky measurements. Results of such a study are important and useful for frequency selection and design of microwave and millimeter-wave radiometers for humidity and temperature profiling.

A branch and bound feature selection algorithm has been used to determine the sets of frequencies. The degrees of freedom and the vertical resolution for each frequency set are also determined. Finally, an analysis has been performed to determine the impact of measurement uncertainty on the number of degrees of freedom of measurement and also the vertical resolution.

4.1. Introduction

Typically, retrieval algorithms use frequencies near water vapor absorption at 22.235 and 183.31 GHz [17] [42] for humidity profile retrieval as well as frequencies near 60 GHz for temperature profile retrieval [48]. These frequency ranges provide the largest amount of information on water vapor and temperature in the troposphere as a function of altitude. However, accurately determining sets of frequencies that provide the maximum amount of information for retrievals is important to optimize the use of resources when designing and fabricating microwave and millimeter-wave radiometers.

Previous research has focused on information content analysis of the frequency range of 20 – 70 GHz using eigenvalue analysis of the weighting function (WF) covariance matrix [16]. The

WF or Jacobian is the sensitivity of ground-based zenith-viewing brightness temperatures to change in the atmospheric parameter of interest, as shown in Eqns. (IV.1) and (IV.2) for the parameters of water vapor and temperature, respectively [28].

$$WF_{\rho_v}^{\downarrow R}(s) = e^{-\tau(0,s)} \frac{\partial \alpha(s)}{\partial \rho_v} \left[T'(s) - T_{b0} e^{-\tau(s,\infty)} - \int_s^\infty T'(s') \alpha e^{-\tau(s,s')} ds' \right] \tag{IV.1}$$

$$WF_T^{\downarrow R}(s) = \frac{dT'}{dT} \alpha(s) e^{-\tau(0,s)} + e^{-\tau(0,s)} \frac{\partial \alpha(s)}{\partial T} \left[T'(s) - T_{b0} e^{-\tau(s,\infty)} - \int_s^\infty T'(s') \alpha e^{-\tau(s,s')} ds' \right] \tag{IV.2}$$

where s represents the altitude above ground, $\alpha(s)$ is the total absorption coefficient, $\rho_v(s)$ is the water vapor density, $T(s)$ is the temperature, $T'(s) = \frac{T(s)}{R(T)}$, $R(T) = 1$, and $R(T)$ is the Rayleigh-Jeans approximation factor [15], T_{b0} is the cosmic background radiation and $\tau(s_1, s_2)$ is the optical depth from s_1 to s_2, given by $\tau(s_1, s_2) = \int_{s_1}^{s_2} \alpha(s) ds$.

Other previous work has focused on finding the rank of frequencies in the 18 – 37 GHz range to determine those suitable for estimating the wet-path delay using microwave radiometers [49]. This analysis consists of constructing two- and three-frequency sets for the 18 – 37 GHz frequency range. Measurements were simulated for each frequency set using radiosonde data collected from various launch sites, and each set was ranked based on its retrieval noise.

Additionally, the WFs in the frequency range of 10 – 1000 GHz was analyzed to identify frequencies that are useful in retrieving water vapor and temperature profiles with high vertical resolution from nadir-viewing airborne radiometer measurements [50]. The selected frequency ranges were 43 – 86 GHz and 121 – 183 GHz for temperature and water vapor retrieval, respectively. These frequency sets were found to provide the best resolution for retrieval over the range of effective heights [50] from 1.9 to 6.4 km, although this result varies slightly with season and geographic location. The water vapor and temperature WFs [50] for nadir-viewing airborne radiometer are given in Eqns. (IV.3) and (IV.4).

$$WF_{\rho_v}^{\uparrow}(s) = e^{-\tau(s,h)} \frac{\partial \alpha(s)}{\partial \rho_v} \left[T'(s) - T_{b0}^{0\downarrow RE} e^{-\tau(0,s)} - \int_0^s T'(s') \alpha e^{-\tau(s',s)} ds' \right] + e^{-\tau(0,s)} r WF_{\rho_v}^{\downarrow R}(s) \tag{IV.3}$$

$$T_{b0}^{0\downarrow RE} = (1-r)T'(f, T_S) + (rT_B(f, 0, \infty))$$

$$WF_T^{\uparrow}(s) = \frac{dT'}{dT} \alpha(s) e^{-\tau(s,h)} + e^{-\tau(s,h)} \frac{\partial \alpha(s)}{\partial T} \left[T'(s) - \int_0^s T'(s') \alpha e^{-\tau(s,s')} ds' - e^{-\tau(0,s)} \{(1-r)T' + r(T'(f, T_S) + WF_T^{\downarrow R}(s))\} \right] \tag{IV.4}$$

where:

- h is the observation height above ground level
- r is the surface reflection coefficient
- T_S is surface temperature
- $(1-r)T'(f, T_S)$ is the brightness temperature emitted from the surface
- $T_B(f, 0, \infty)$ is the downwelling brightness temperature
- $rT_B(f, 0, \infty)$ is the atmospheric downwelling brightness temperature reflected from the surface
- $T_{b0}^{0\downarrow RE}$ is the sum of the reflected and the emitted radiation and
- $WF_{\rho_v}^{\downarrow R}(s)$ and $WF_T^{\downarrow R}(s)$ are the downwelling water vapor and temperature weighting functions from Eqns. (IV.1) and (IV.2), respectively

To extend and expand upon previous work, this chapter focuses on determining the maximum number of independent measurements possible in the range 10 to 200 GHz, with a bandwidth of 100 MHz, for the retrieval of atmospheric water vapor and temperature profiles using zenith-pointing ground-based and nadir-pointing airborne radiometers under a variety of clear sky atmospheric conditions, including winter and summer weather, as well as over the diurnal cycle.

4.2. Frequency Identification Process Based on Feature Selection to Maximize the Number of Degrees of Freedom

The strategy used in this work is to identify the nonredundant frequencies in the range from 10 to 200 GHz, with a bandwidth of 100 MHz, which contribute to water vapor and temperature profile retrieval, with the goals of fine vertical resolution and good retrieval accuracy. The 100-MHz bandwidth is a requirement to ensure that the frequency channels do not "average over" any feature of interest. However, from a practical point of view, radiometers often have bandwidths greater than 100 MHz to reduce noise, but this should not have any significant impact on the frequencies sets selected and the associated number of degrees of freedom (DOF). The number of DOF is used as a criterion and is considered to be the same as the number of independent measurements in the retrieval solution. To determine this number, we first select those frequency sets that are the most sensitive to the atmospheric parameter of interest and retrieve the parameter with optimum vertical resolution from ground level to the top of the troposphere (~10 km). A feature selection algorithm is used to determine the most significant frequencies by selecting those with linearly independent WFs, i.e., those providing nonredundant information. The WFs are calculated using Eqns. (IV.1) and (IV.2) for zenith-pointing ground based radiometers and Eqns. (IV.3) and (IV.4) for nadir-viewing airborne radiometers.

WFs are dependent on atmospheric conditions and on measurement frequency. Therefore, atmospheric parameters are needed to compute the WF for each frequency. These parameters can be obtained from radiosondes that are launched 2-4 times daily from many weather stations in and near populated areas of the world's land masses. This study uses radiosonde data from the U.S. Department of Energy (DOE)'s Atmospheric Radiation Measurement (ARM) Southern Great Plains (SGP) site near Lamont, Oklahoma to calculate the WFs [51].

4.2.1 Feature Selection and Number of Degrees of Freedom

Feature selection [52] [53], also known as variable selection, is the process of selection of a subset of relevant variables from a larger set. For this study, the variables are the measurement frequencies. When using a feature selection algorithm, the main assumption is that the data (here the WFs) have some redundant or irrelevant elements and the goal is to identify and remove then. Therefore, feature selection is a dimensionality reduction algorithm. In this study, a branch and bound algorithm [54] is used, as described below.

Assume that a set Z_m contains relevant, redundant, and unnecessary features, i.e., X_1, X_2, X_3,…, X_m, where m is the total number of elements of the set. The selection algorithm provides a subset of n elements, Z_n which are those n elements that have the most relevant features within Z_m. To select the subset Z_n, a selection criterion J has to be defined.

If J is monotonic, any subset of features should have a value of J that is less than or equal to that of any proper superset or superset. However, excluding a particular feature from a large set may not significantly impact the criterion values (i.e., number of DOF). Therefore, each feature in the m-feature superset (Z_m in Figure 10) is removed (one at a time), and the value of J is evaluated for each of the resulting subsets at level 1 in Figure 10. The subset with the maximum value of J (Z_{m-1}) at level 1 is selected, and all other subsets are discarded. All subsets of Z_{m-1} at level 2 have a value of J that is less than or equal to that of Z_{m-1}. The subsets of Z_{m-1} (at level 2 in Figure 10) with the maximum value of J (Z_{m-2}) is selected, while others are discarded. This process of selecting the subset with the maximum value of J and discarding all others is repeated until the desired number of features is selected. In this study, the number of DOF for a set of features under consideration is the selection criterion, where features are the WFs corresponding to various frequencies.

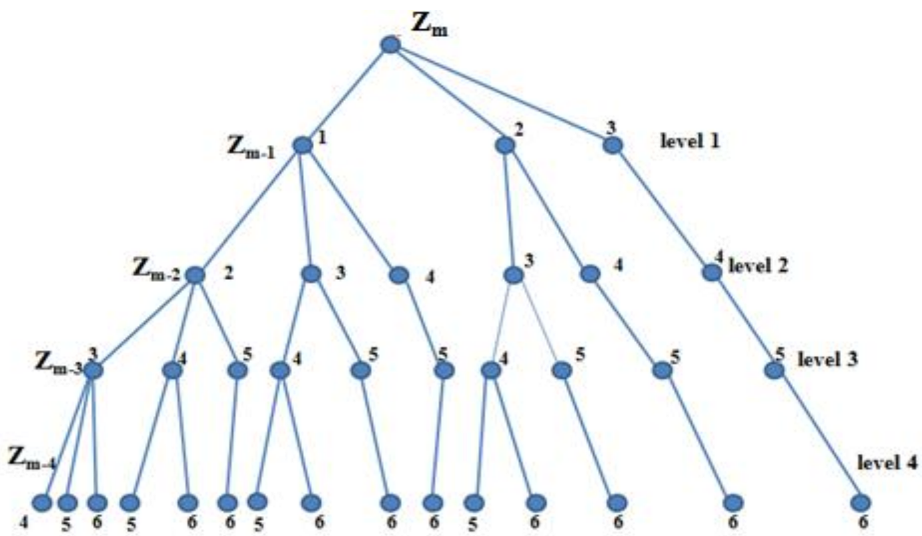

Figure 10: A solution tree based on a branch and bound feature selection algorithm.

The averaging kernel is calculated using Eqn. (IV.5) [14], and the number of DOF is calculated as the trace of averaging kernel matrix Eqn. (IV.6) [14]

$$\overline{\overline{AK}} = \bar{\bar{S}}_a \overline{\overline{WF}}^T (\overline{\overline{WF}} \bar{\bar{S}}_a \overline{\overline{WF}}^T + \bar{\bar{S}}_\varepsilon)^{-1} \overline{\overline{WF}} \quad \text{(IV.5)}$$

$$DOF = tr(\overline{\overline{AK}}) \quad \text{(IV.6)}$$

where

- $\bar{\bar{S}}_a$ is the background information covariance matrix, with dimensions depending on the number of layers used for the retrieval and with values calculated based on the statistics of radiosonde profiles
- $\overline{\overline{WF}}$ is the weighting function matrix
- $\bar{\bar{S}}_\varepsilon$ is the measurement error covariance matrix. The measurements at each of the frequencies are independent of each other, so the errors associated with the measurements are also

independent. $\bar{\bar{S}}_\varepsilon$ includes the noise due to radiometric observations, representativeness error and radiative transfer model errors [11]. However, the off-diagonal elements are assumed to be negligible, and the radiometer instrument noise is considered to be 0.5 K. In addition, in the later part of this study for determining the impact of measurement error on DOF and vertical resolution, variable measurement noise has been used and the effects of representativeness error and radiative transfer model error have also been included

The feature selection algorithm evaluates a set of WFs corresponding to the frequency range 10 to 200 GHz to determine the major contributing frequencies for remote sensing of water vapor and temperature profiles. The value of *m* is 1900, and the frequency selection process is repeated for values of *n* equal to 2, 3, 4, 5, 10, 20, 30, 40 and 50.

4.2.2 Averaging Kernel and Vertical Resolution

The vertical resolution of a retrieved profile is defined as the spread of its averaging kernel, given by Eqn. (IV.7). The averaging kernel is a linear combination of WFs for the frequencies used in the study, as shown in Eqn. (IV.8) [14].

$$sp(z) = 12\int (z-z')^2 \left[\sum_{i=1}^{m} \overline{\overline{WF}}_i(z')G_a(z)\right]^2 dz' \tag{IV.7}$$

$$AK(z,z') = \int \sum_{i=1}^{m} \overline{\overline{WF}}_i(z')G_a(z)\,dz' \tag{IV.8}$$

The spread of an averaging kernel can be rewritten as Eqn. (IV.9)

$$sp(z) = G_a(z)^T \bar{\bar{Q}}_a(z) G_a(z) \tag{IV.9}$$

where $G_a(z)$ is the gain function (containing coefficients for a linear combination of WFs), and $\bar{\bar{Q}}_a$ is given by Eqn. (IV.10).

$$\bar{\bar{Q}}_{a_{ij}}(z) = 12\int (z-z')^2 \overline{\overline{WF}}_i(z')\overline{\overline{WF}}_j(z')\,dz' \tag{IV.10}$$

where the $\bar{\bar{Q}}_a$ matrix elements are the correlations between values of the WFs at two different frequencies (i and j) at various altitudes z. $\overline{\overline{WF}}$ is the WF matrix, z is height above ground level, i and j are the indices of the frequency channels and z' is the height above ground level of the center of the averaging kernel.

Achieving optimal vertical resolution requires minimizing the spread of the averaging kernel. An ideal averaging kernel would be a Dirac delta function. However, the spread of an averaging kernel is determined based on a finite number of WFs (for different weather conditions) at the corresponding frequencies of measurement. The limited number of WFs makes it virtually impossible to achieve a delta function as an averaging kernel. To address this limitation, the Backus-Gilbert technique improves the vertical resolution by using a gain function, calculated as in Eqn. (IV.11) [14], to minimize the spread of the averaging kernel. Using Eqns. (IV.10) and (IV.11) in Eqn. (IV.9), the spread of the averaging kernel is given by Eqn. (IV.12).

$$\bar{g}_a(z) = \frac{\bar{\bar{Q}}_a^{-1}(z)\bar{u}}{\bar{u}^T\bar{\bar{Q}}_a^{-1}(z)\bar{u}} \tag{IV.11}$$

$$sp(z) = \frac{1}{\bar{u}^T\bar{\bar{Q}}_a^{-1}\bar{u}} \tag{IV.12}$$

where the elements of $\bar{u}$ are given by Eqn. (IV.13)

$$u_i = \int_0^{10\ km} \overline{\overline{WF}}_i\, dz \tag{IV.13}$$

4.3. Analysis of Water Vapor and Temperature Measurements from Zenith-Pointing Ground-Based Radiometers

4.3.1 Effect of Liquid Water on Temperature and Water Vapor Profile Retrieval

Brightness temperature measurements near weak (22.235 GHz) and strong (183.31 GHz) water vapor absorption lines have significant contributions from cloud liquid water and precipitation, when present, which can be major sources of error in water vapor retrieval. The contributions from clouds and precipitation can be due to scattering and/or absorption at microwave and millimeter-wave frequencies. Figure 11 shows microwave and millimeter-wave absorption spectra of water vapor, oxygen and liquid water absorption coefficients for 10 to 200 GHz.

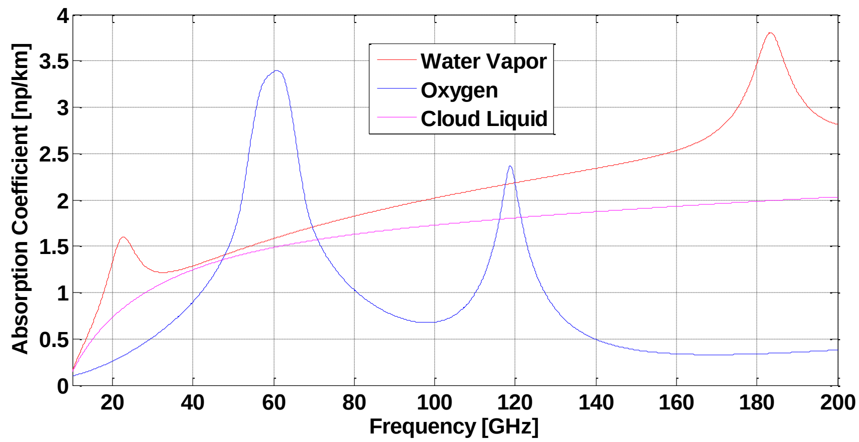

Figure 11: Microwave and millimeter-wave absorption spectra from 10 to 200 GHz for water vapor density of 15.1 g/m^3, temperature of 297 K and a cloud liquid water density of 0.1 g/m^3.

Typically, scattering occurs in nonprecipitating ice clouds, whereas absorption occurs in liquid clouds. The emission by clouds is also affected by cloud thermodynamic temperature [55]. Cloud liquid is a significant contributor to measured brightness temperature near the weak water vapor absorption line at 22.235 GHz. However, water drops in clouds can be very small compared to the wavelength of the radiation, so the Rayleigh approximation can be used. Based on this approximation, scattering can be neglected in the forward radiative transfer equations, so only absorption models are used [4]. Water vapor profile retrieval with current methods is highly inaccurate during precipitation [56], unless specifically tuned for it [57]. For this reason, cloudy conditions have not been considered, and all the cases used in this study are for clear sky conditions.

4.3.2 Determining Measurement Frequencies for Ground-Based Water Vapor Profiling

A branch and bound feature selection technique is applied to the water vapor WFs calculated using Eqn. (IV.1) for frequencies in the range from 10 to 200 GHz. As described in Section 4.2, WFs have been calculated using radiosondes launched from the ARM SGP site. These WFs have been calculated for four "typical" weather conditions, i.e., winter day/night and summer day/night based on radiosondes launched during December/January and June/July for winter and summer, respectively, and at noon/midnight for day/night, respectively. The frequencies selected for each value of *n* are shown in Figure 12, where *n* is the number of main contributing frequencies, as defined in Section 4.2.1. For any of these four combinations of season and time of day, frequencies near the weak water vapor absorption line at 22.235 GHz are selected as the first contributing measurement frequency for water vapor sensing, in agreement with previous work [49]. The first 10 selected frequencies for water vapor retrieval in each case are given in Table 1. Similarly, frequencies relatively close to the strong water vapor absorption line at 183.31 GHz are selected as the second contributing frequency, near 200 GHz.

Table 1: First 10 frequencies (in GHz) selected for water vapor profile retrieval from ground-based measurements for winter day/night and summer day/night conditions

Winter Day	21.3	198.9	65.3	167.7	22.9	168.1	21.7	22.5	23.3	64.9
Winter Night	21.3	198.9	165.3	22.9	85.7	164.9	165.7	85.3	22.5	23.3
Summer Day	21.3	198.9	90.5	174.9	22.9	175.3	131.3	20.5	24.1	25.7
Summer Night	21.3	198.9	22.9	170.1	55.7	170.5	120.5	20.5	22.5	24.1

When the number of frequencies to be selected is greater than two, the frequencies selected vary with the season and time of the day. When the number of frequencies selected is 3 and 4, frequencies near 90 and 165 GHz are also selected along with the frequencies near 23 and 183 GHz.

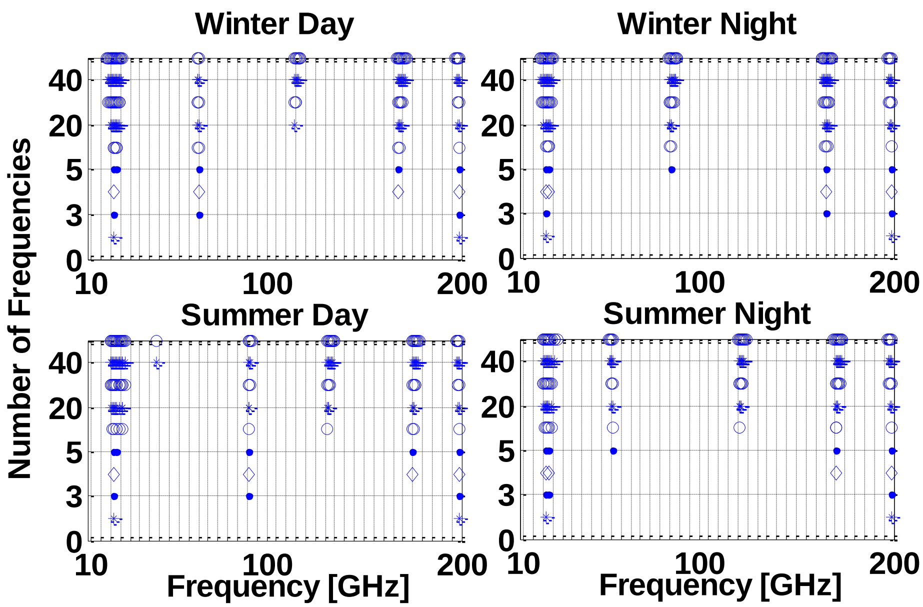

Figure 12: Main contributing frequencies for water vapor profile retrieval from a ground-based radiometer determined using the feature selection method for the frequency range of 10-200 GHz. The width of the horizontal axis divisions is 5 GHz.

The selected frequencies were analyzed to determine the number of independent pieces of information by calculating their number of DOF using Eqns. (IV.5) and (IV.6). The parameters required for the averaging kernel in Eqn. (IV.6), i.e., background covariance matrix $\bar{\bar{S}}_a$ and WF matrix $\overline{\overline{WF}}$, are calculated using a background data set of radiosonde profiles measured at the ARM SGP site [51]. The background data set is a collection of water vapor and temperature profiles for the appropriate season and time of the day, i.e. winter day/night or summer day/night for this study. Similarly, WFs are calculated using mean water vapor and temperature profiles from the same data set. The number of DOF is calculated for each set of selected frequencies based on the value of *n*. This process is followed for a number of background data sets, and the resulting mean and standard deviation of each value of *n* is shown in Figure 13. It can be seen that the number of DOF is slightly lower during winter than during summer, for both day and night. This is because water vapor profiles are more variable during summer than during winter.

When the number of frequencies selected is in the range of 2 – 5, the mean number of DOF increases linearly with the number of selected frequencies.

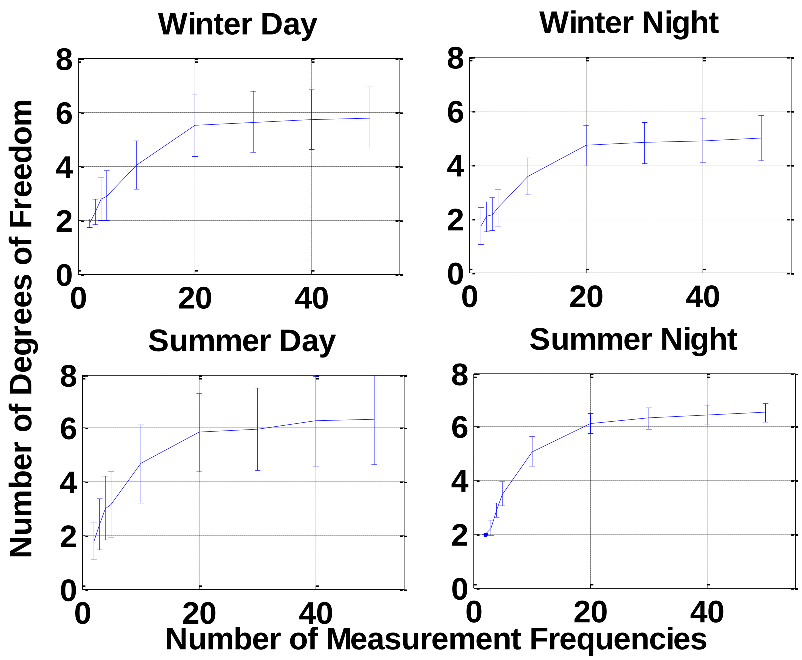

Figure 13: Number of DOF for water vapor profile retrieval from ground-based radiometer measurements under four different clear-sky weather conditions, i.e. winter day/night and summer day/night, for the frequency range of 10 - 200 GHz.

When the number of frequencies selected is in the range of 5 - 20, the number of DOF continues to increase, but at a much slower rate. For the range of 20 - 50 frequencies, the number of DOF saturates. The range of maximum number of DOF (for a mean profile) is 5 - 6.2 for any atmospheric condition. Hence, increasing the number of selected frequencies of measurement above a certain value does not significantly increase the number of independent pieces of information. For example, the number of DOF increases by only one or two as the number of measurement frequencies is increased from 10 to 40.

It is also important to determine the vertical resolution of the retrieval using the selected frequencies. In this study, vertical resolution is defined as spread of the averaging kernel based on the Backus-Gilbert technique, as described in Section 4.2.2. Vertical resolution is computed as the spread is computed as the spread of the averaging kernel for the first two frequencies selected for winter and summer daytime using Eqn. (IV.12) for a height range of 0 to 10 km above ground level, as shown by the black curves in Figure 14, (a) for winter and (b) for summer.

Similarly, the vertical resolution is calculated for the first three selected frequencies, as shown by the red curves in Figure 14. This process is continued for 4, 5 and 10 selected frequencies. There is a general trend of degradation in vertical resolution as the altitude increases. However, the spread decreases and vertical resolution improves as the number of selected frequencies increases. The vertical resolution for 10 measurements is approximately 0.5 to 1.5 km from 0 to 2 km above ground level for both winter and summer. However, from 2 to 9 km above ground level the vertical resolution for 10 measurements is approximately 1.5 to 3 km.

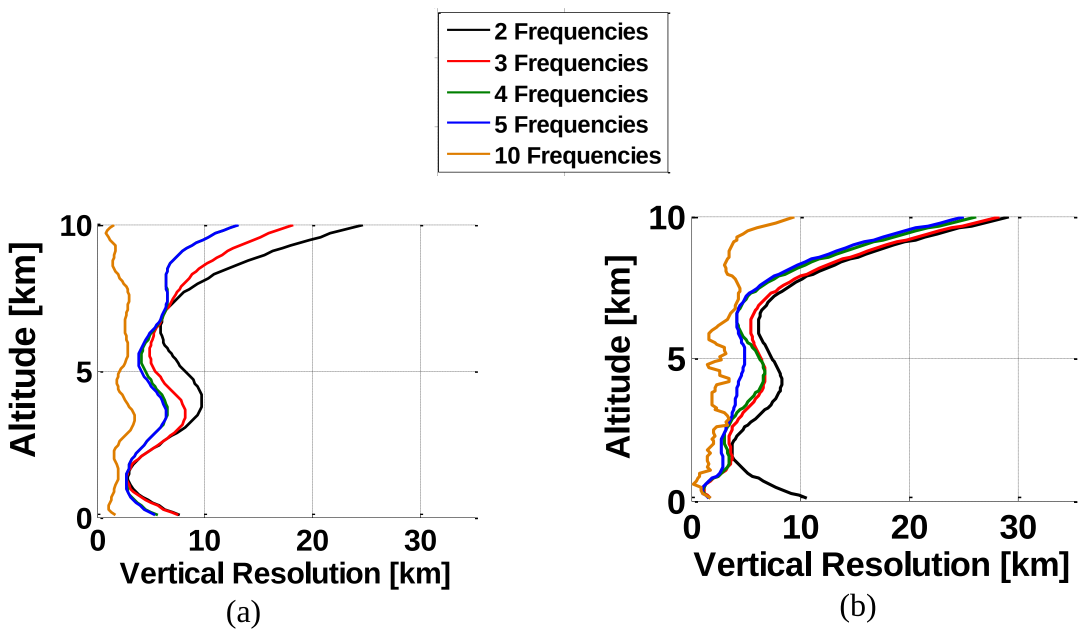

Figure 14: Vertical resolution for water vapor profile retrieval from a ground-based radiometer as a function of altitude for (a) winter and (b) summer daytime.

The weighting functions corresponding to the frequencies contributing the greatest number of independent pieces of information as well as improving the vertical resolution for water vapor profile retrieval are shown in Figure 15.

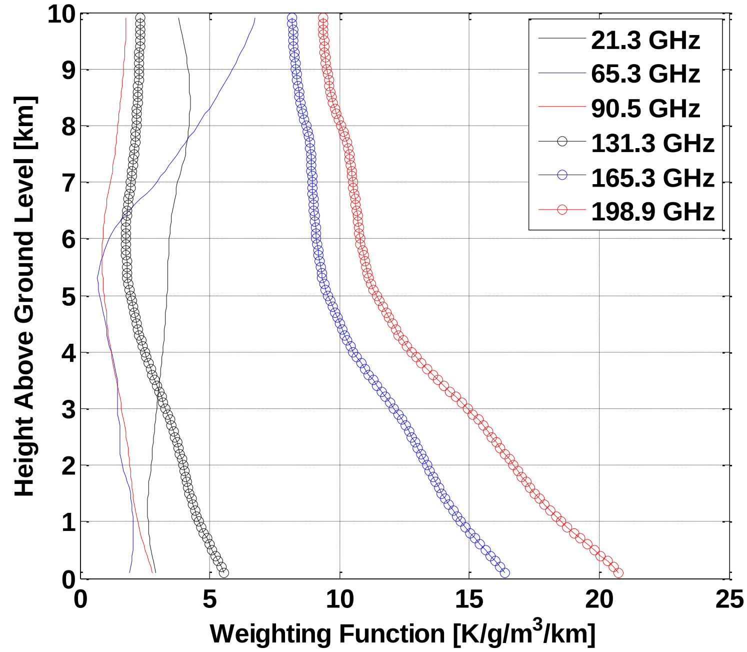

Figure 15: WFs for the frequencies selected for water vapor profile retrieval from a ground-based radiometer measurements in the range from 10 to 200 GHz.

Weighting functions corresponding to 131.3, 165.3 and 198.9 GHz show that these measurement frequencies are sensitive to water vapor in the lower parts of the troposphere and hence are complementary to 21.3 GHz for estimation of water vapor profiles. Frequencies closer to the strong water vapor absorption line are more sensitive to changes in water vapor close to the ground. The weighting function at 198.9 GHz is highly sensitive to small changes in water vapor, as stated by Cimini et al. [43] and Racette et al. [58]. This and similar frequencies are useful to retrieve the water vapor profile in very dry climates, such as the polar regions [43]. Measurements corresponding to 90.5 GHz in the window region from approximately 85 to 110 GHz have been used to estimate the total precipitable water, as described by Payne et al. [59].

4.3.3 Determining Measurement Frequencies for Ground-based Temperature Profiling

Temperature profiles have been retrieved from satellite-based radiometric measurements in the 50 – 70 GHz range [12], i.e., near the oxygen absorption lines centered at 60 GHz.

Measurements at frequencies further away from the 60 GHz oxygen complex provide information about the temperature at lower altitudes, based on the temperature weighting functions. Frequencies near the higher-frequency millimeter-wave oxygen absorption line at 118.75 GHz have not been used extensively for temperature profiling. Also, the window region frequencies between these absorption lines have not been analyzed in detail for temperature retrieval. To include them in this study, the entire frequency range of 10 to 200 GHz has been analyzed to determine sets of frequencies that provide the maximum amount of information on tropospheric temperature profiles.

Similar to the retrieval of water vapor profiles, retrieval of temperature profiles also requires the maximum number of independent pieces of information (or minimum redundancy) to improve accuracy and sensitivity to changes in temperature as a function of altitude. The major contributing frequencies were selected by applying a feature selection algorithm similar to that used for water vapor selection in Section 4.3.2 to the temperature weighting functions corresponding to frequencies in the 10 to 200 GHz range.

The first 10 selected frequencies are listed in Table 2 and shown in Figure 16. Frequencies close to 60 GHz have greater information content and provide more independent measurements than those close to the oxygen absorption line at 118.75 GHz. For all weather conditions considered in this study, the frequency ranges of 55 – 65 GHz and 116 – 120 GHz are selected, which are close to the 60 GHz oxygen complex and the 118.75 GHz oxygen absorption line, respectively.

Table 2: First 10 frequencies (in GHz) selected for temperature profile retrieval from ground-based measurements for winter day/night and summer day/night conditions

Winter Day	60.1	118.1	55.7	119.3	67.3	119.7	63.3	116.9	67.7	116.1
Winter Night	60.5	118.1	63.3	62.5	118.9	116.9	64.9	55.3	65.7	66.1
Summer Day	60.1	117.7	62.5	116.5	64.5	118.1	118.5	119.3	119.7	116.1
Summer Night	60.1	118.1	62.5	116.5	119.3	117.7	119.7	61.7	64.5	116.1

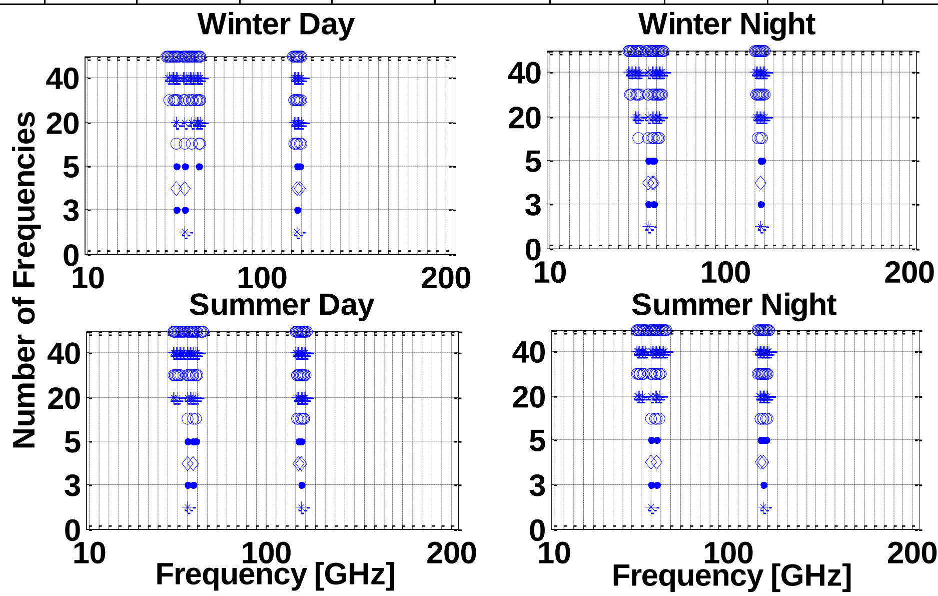

Figure 16: Main contributing frequencies for temperature profile retrieval from a ground-based radiometer determined using the feature selection method for the frequency range of 10 to 200 GHz. The width of the horizontal axis divisions is 5 GHz.

The selected frequencies were analyzed to determine the number of independent pieces of information by calculating their number of DOF, as shown in Figure 17. The number of DOF increases approximately linearly with the increase in the number of frequencies selected up to 10 and then more slowly than linearly up to 20. The number of DOF starts to saturate near or above 30 selected frequencies. The maximum mean DOF is in the range of 6 – 7 for temperature profile retrieval from zenith-pointing ground-based radiometers, under nearly all clear-sky weather conditions considered in this study.

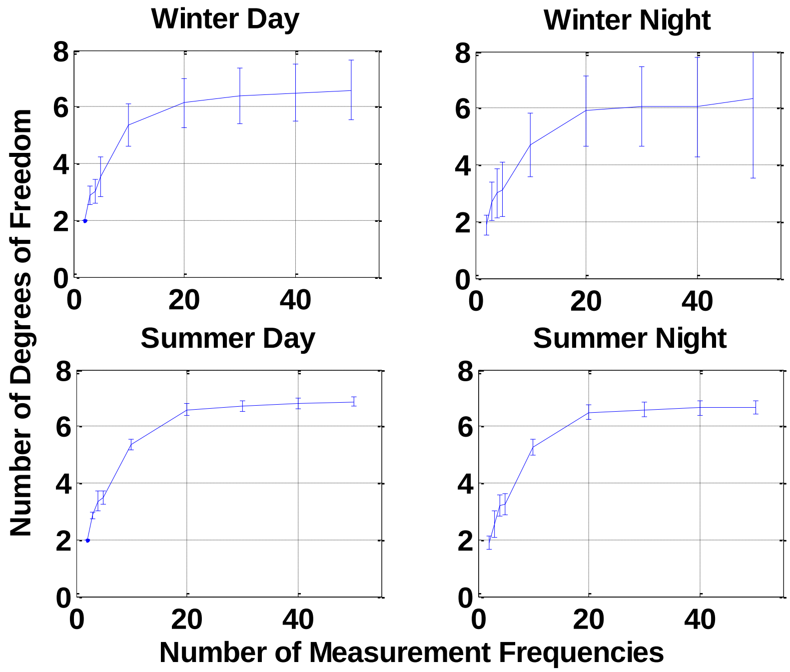

Figure 17: Number of DOF for temperature profile retrieval from a ground-based radiometer under four different clear-sky weather conditions, i.e. winter day/night and summer day/night, for the frequency range of 10 to 200 GHz.

However, the mean maximum number of DOF is slightly higher for summer (6.7) than for winter (6.4), which is similar relationship as that in Section 4.3.2 (Figure 13) for water vapor measurements. This is due to the greater variability of temperature profiles in summer than in winter. After examining the number of DOF, the vertical resolution was analyzed for the selected frequencies for temperature profiling, similarly to what was done for water vapor profiling. The spread of averaging kernel is determined for first 2, 3, 4, 5 and 10 frequencies selected for temperature profiling during daytime, as shown by the black, red, green, blue and orange curves, respectively, in Figure 18, (a) for winter and (b) for summer. There is a general degradation in vertical resolution as the altitude increases. However, the vertical resolution decreases as number of frequencies selected increases. The vertical resolution for 10 measurements is approximately 0.2 to 0.5 km from the ground to 4 km above ground level.

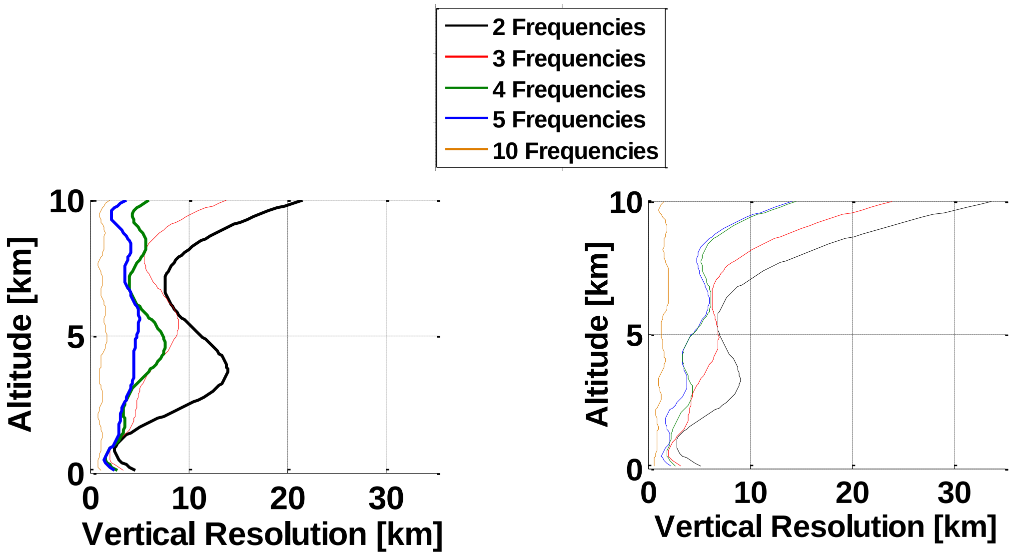

(a) (b)

Figure 18: Vertical resolution for temperature profile retrieval from a ground-based radiometer as a function of altitude for (a) winter and (b) summer daytime.

Figure 19 shows the weighting functions for the frequencies selected for temperature profile retrieval. Most of the weighting functions are most sensitive to temperature changes in the lowest 2 km of the troposphere.

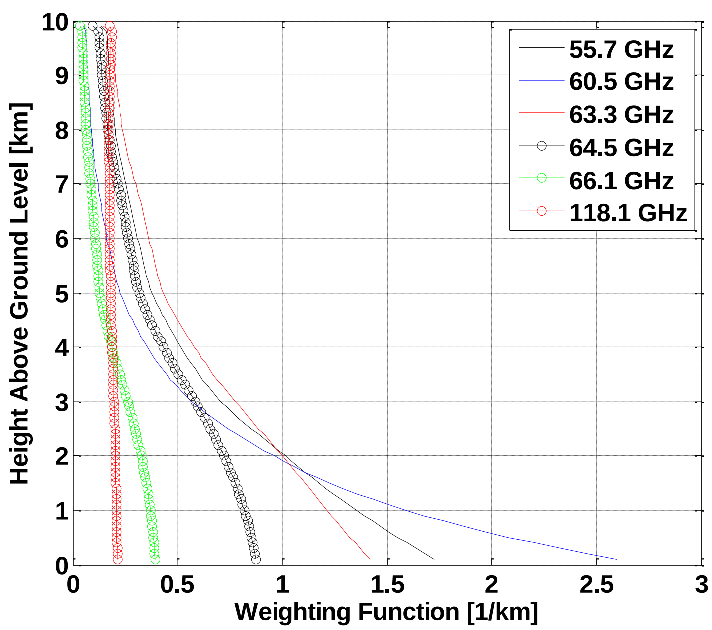

Figure 19: Temperature WFs for frequencies selected for temperature profiling retrieval from a ground-based radiometer in 10 to 200 GHz range.

The 55.7, 60.5 and 63.3 GHz frequencies are most sensitive to changes in temperature from the ground to 2 km above ground level, while the frequencies 64.5 and 66.1 GHz (further from the 60 GHz oxygen complex) are generally more sensitive to changes in temperature over the height range of 0 to 4 km. None of the weighting functions studied have much sensitivity to changes in temperature above about 7 km above general level.

4.4. Analysis of Water Vapor and Temperature Measurements from a Nadir-Pointing Airborne Radiometer

This section focuses on determining the measurement frequencies in the 10 to 200 GHz range to provide the maximum number of independent pieces of measurements for water vapor and temperature profile retrievals for a nadir-pointing airborne microwave radiometer. For the study in Sections 4.4.1 and 4.4.2, the background temperature is assumed to be 290 K and the emissivity of the sea surface to be 0.5. However, in Section 4.4.3 B an analysis has been performed to determine the variability in number of DOF taking into account variations in sea surface and land surface emissivity. The altitude of the aircraft is assumed to be at least 10 km above ground level.

4.4.1 Determining Measurement Frequencies for Airborne Water Vapor Profiling

The branch and bound feature selection algorithm was applied to water vapor weighting functions in the 10 to 200 GHz range to determine the major contributing frequencies for retrieval of water vapor profiles. The first 10 selected major contributing frequencies for a nadir-pointing airborne radiometer are listed in Table 3 and shown in Figure 20. The plots show that there are major contributions for frequencies range 180 to 200 GHz for all clear-sky weather conditions studied, but there are also some significant contributors in the window region in the range of 130 to 165 GHz. Measurements in this frequency range can be used for accurate retrieval of profiles of water vapor in the upper troposphere (5 – 10 km) where the water vapor density is less than 0.5 g/m^3. This is because frequencies close to the strong water vapor absorption line are highly attenuated, even with a small amount of water vapor is present. However, the atmosphere is more transparent near the weak water vapor absorption line (in the range of 20 to 23 GHz), so 21.3 GHz can be used for retrieval of water vapor profile in the lowest 10 km of the troposphere.

Table 3: First 10 frequencies (in GHz) selected for water vapor profile retrieval from airborne measurements for winter day/night and summer day/night conditions

Winter Day	179.3	184.1	182.5	180.1	183.3	183.7	184.7	180.9	180.5	166.9
Winter Night	190.5	198.9	181.3	174.9	182.9	175.3	180.5	191.3	184.1	185.7
Summer Day	175.7	179.7	187.3	178.9	183.7	186.5	186.9	187.3	182.5	146.5
Summer Night	162.1	187.3	179.3	184.9	186.5	182.5	179.7	186.1	183.7	21.3

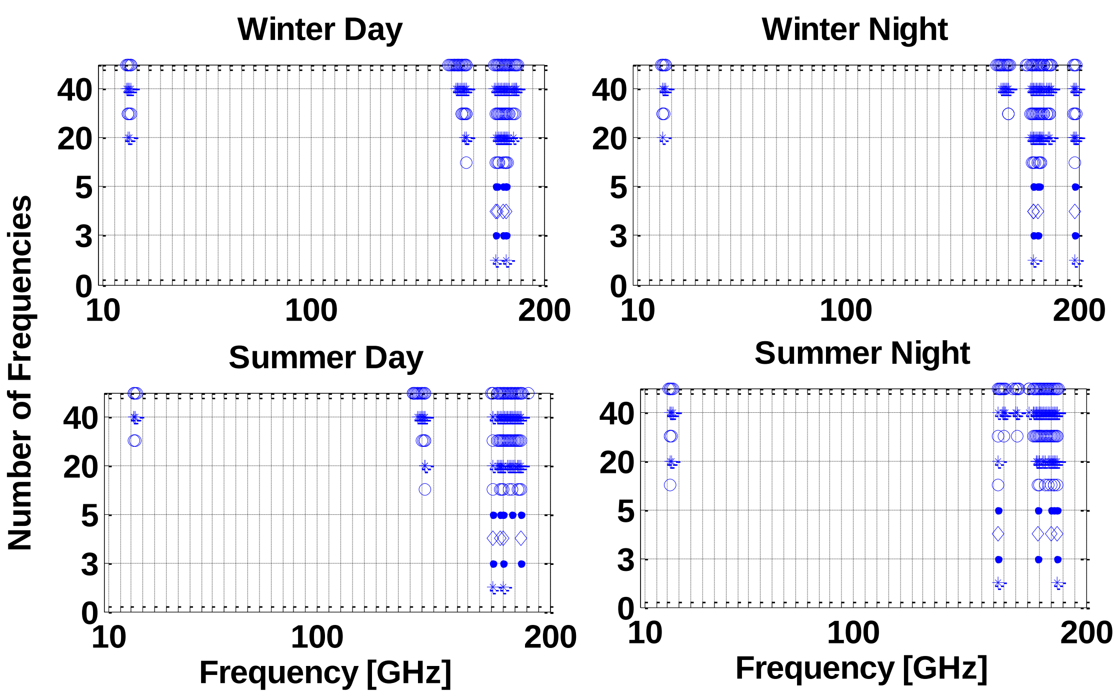

Figure 20: Main contributing frequencies for water vapor retrieval from airborne measurements selected using the feature selection method for frequency range 10 to 200 GHz. The width of the horizontal axis divisions is 5 GHz. The bandwidth is 100 MHz.

The number of DOF calculated for each value of *n* (from 2 to 50) corresponding to all weather conditions is shown in Figure 21. Maximum mean DOF for all weather conditions studied is approximately 8 – 9, lowest for winter night and highest for summer day. The maximum mean DOF is higher than that for zenith-pointing ground-based radiometer.

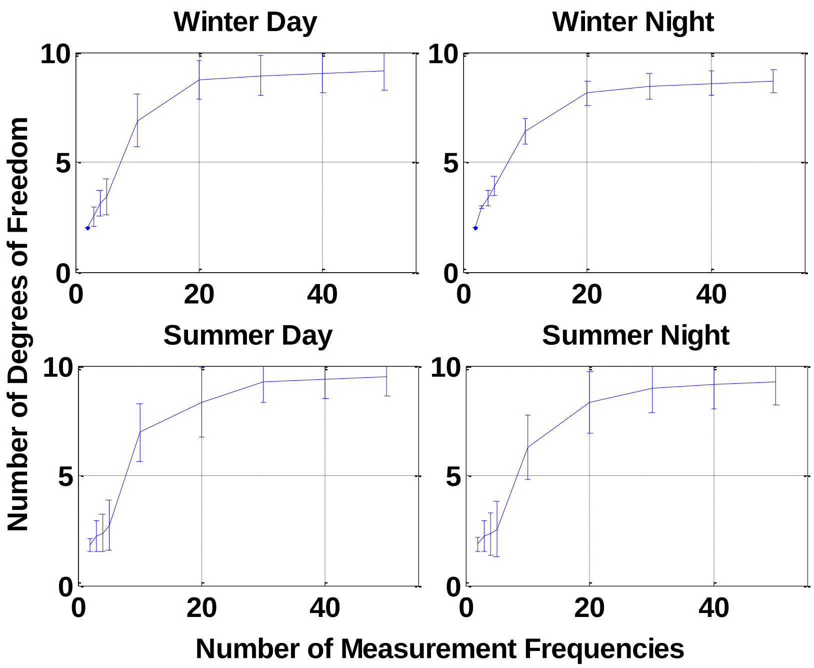

Figure 21: Number of DOF for water vapor profile retrieval from airborne measurements under four different weather conditions, i.e. winter day/night and summer day/night, for the frequency range of 10 to 200 GHz.

The vertical resolution is computed for frequencies selected for water vapor profile retrieval using a nadir-pointing airborne radiometer. The spread of the averaging kernel determined for first 2, 3, 4, 5 and 10 frequencies selected for daytime is shown by black, red, green, blue and orange curves, respectively, in Figure 22, (a) for winter and (b) for summer. The vertical resolution in this case is better at 10 km above ground level than at ground level due to the difference in the radiative transfer integral, resulting in nadir-pointing airborne and space-borne radiometers providing more information in the upper troposphere. The vertical resolution is best for 10 measurements and is approximately 0.2 to 0.5 km from 6 to 10 km above ground level for winter, while it is 0.2 to 1 km for summer. The vertical resolution degrades closer to the ground.

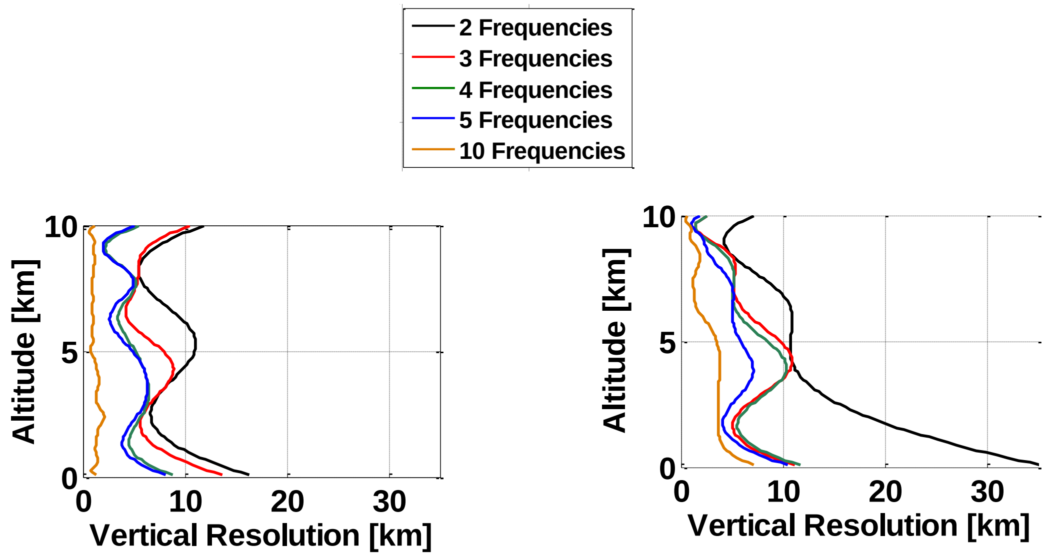

(a) (b)

Figure 22: Vertical resolution for water vapor profile retrieval from airborne measurements as a function of altitude for (a) winter and (b) summer daytime.

Weighting functions corresponding to the major contributing frequencies are shown in Figure 23.

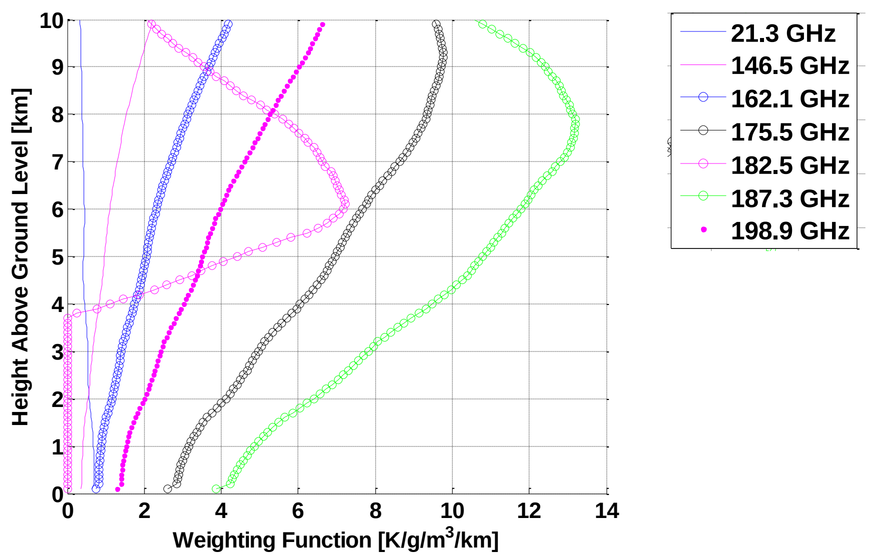

Figure 23: Water vapor weighting functions for frequencies selected for water profile retrieval from nadir-pointing airborne measurements in the range of 10 to 200 GHz.

Those corresponding to frequencies close to the strong water vapor absorption line at 183.31 GHz as well as the window channels peak at various altitudes, are most sensitive to changes above 4 km altitude and can be used for retrieval of water vapor profiles in the upper troposphere.

4.4.2 Determining Measurement Frequencies for Airborne Temperature Profiling

Analysis of the temperature weighting functions in the range of 10 to 200 GHz results in the first 10 frequencies selected for a nadir-pointing airborne radiometer shown in Table 4 and Figure 24.

Table 4: First 10 frequencies (in GHz) selected for temperature profile retrieval from airborne measurements for winter day/night and summer day/night conditions

Winter Day	60.1	117.7	54.9	56.9	56.5	118.1	64.5	59.7	55.3	52.9
Winter Night	60.1	117.7	55.3	56.9	56.5	118.1	64.5	57.7	59.7	54.9
Summer Day	60.1	117.7	55.7	55.3	118.1	60.5	59.7	56.9	56.5	54.9
Summer Night	60.1	117.7	55.3	56.5	118.1	60.5	59.7	56.9	55.7	54.9

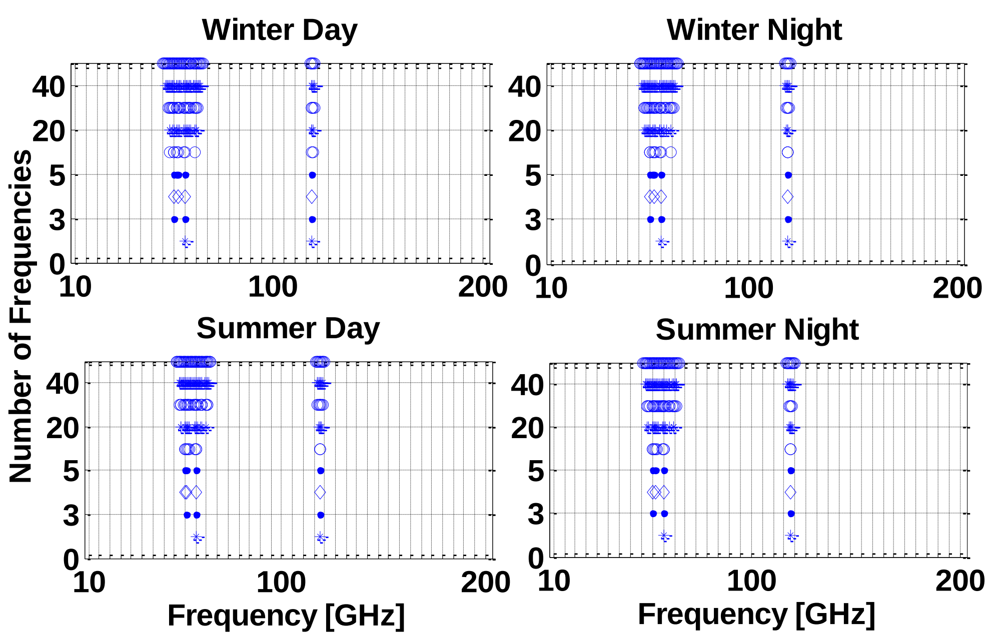

Figure 24: Main contributing frequencies for temperature profile retrieval from airborne measurements selected using the feature selection method for the frequency range 10 to 200 GHz. The width of the horizontal axis divisions is 5 GHz. The bandwidth is 100 MHz.

They show that frequencies close to the 60 GHz and 118.75 GHz temperature absorption lines provide the greatest amount of information for temperature profile retrieval from nadir-pointing airborne radiometers. The number of independent pieces of information from the selected frequency set can be determined by calculating their number of DOF for each weather condition studied, as shown in Figure 25. The maximum mean number of DOF for all weather conditions is in the range of 5 – 6. The number of DOF increases when the number of measurements is increased from 2 to 20, but there is no significant increase in DOF above 20 measurements.

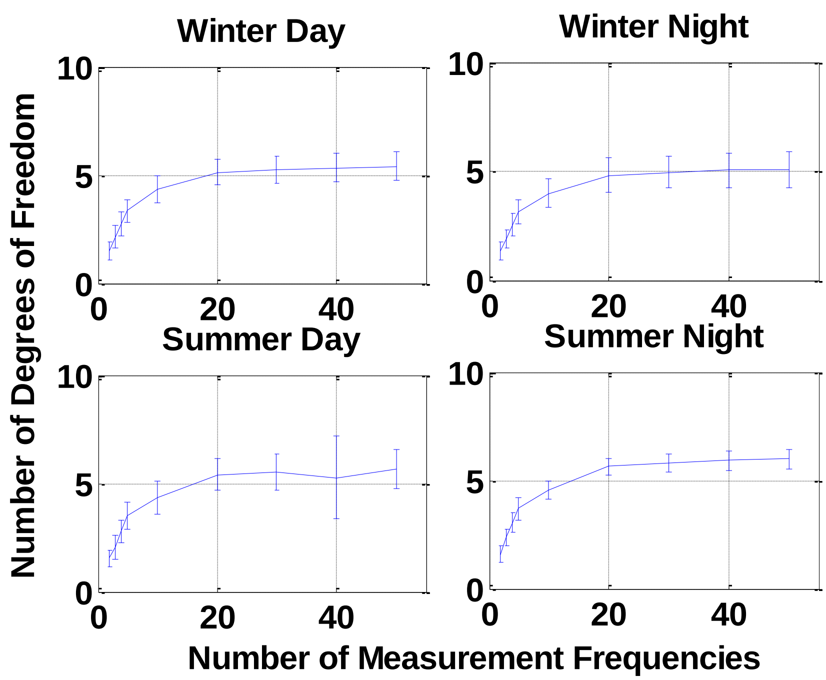

Figure 25: Number of DOF for temperature profile retrieval from airborne measurements under four different weather conditions, i.e. winter day/night and summer day/night, for the frequency range of 10 to 200 GHz.

The spread of the averaging kernel is computed for temperature profile retrieval from nadir-pointing airborne radiometer measurements. The vertical resolution is determined for first 2, 3, 4, 5 and 10 frequencies selected shown by the black, red, green, blue and orange curves, respectively, in Figure 26. Similar to water vapor retrieval from nadir-pointing airborne measurements, the vertical resolution in this case is better at 10 km above ground level than it is at ground level. The vertical resolution is best for 10 measurements and is approximately 0.2 to 0.5 km in winter from 6 to 10 km above ground level and 0.2 to 1 km in summer.

Weighting functions for the major contributing frequencies are shown in Figure 27. The weighting functions corresponding to 55.3, 56.9 and 60.1 GHz peak at various altitudes well above ground level and hence can be used to retrieve temperature profiles.

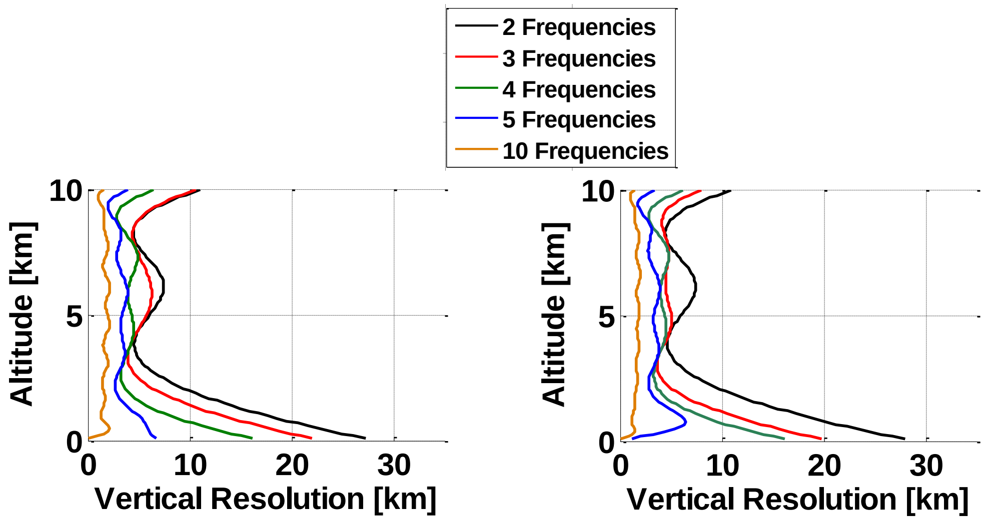

(a) (b)

Figure 26: Vertical resolution for temperature profile retrieval from airborne measurements as a function of altitude for (a) winter and (b) summer daytime.

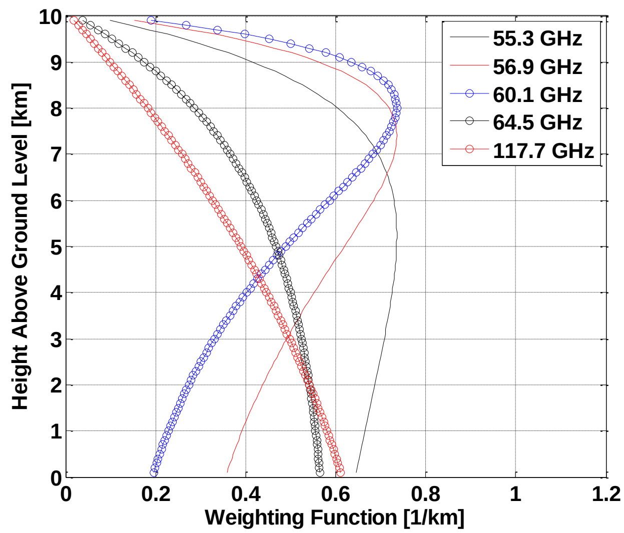

Figure 27: Temperature WFs from nadir-pointing airborne measurements frequencies in the range of 10 to 200 GHz.

The weighting functions at 64.5 and 117.7 GHz are more sensitive to temperature in the lowest 2 km of the troposphere and therefore are complementary to the frequencies closer to the 60 GHz oxygen complex.

4.4.3 Effect of Variation in Measurement Noise and Uncertainty on the Number of Independent Measurements and Vertical Resolution

A. Effect of Variation in Measurement Noise on the Number of DOF

All the previous results have been calculated assuming a radiometric resolution of 0.5 K and a diagonal matrix $\bar{\bar{S}}_\varepsilon$. However, in this section an analysis has been performed to determine the variation in number of DOF for 50 measurement frequencies selected using the branch and bound selection algorithm described in Section 4.2.1 for a zenith-pointing ground-based radiometer when the instrument noise is varied from 0.1 to 1.2 K. The results are shown in Figure 28.

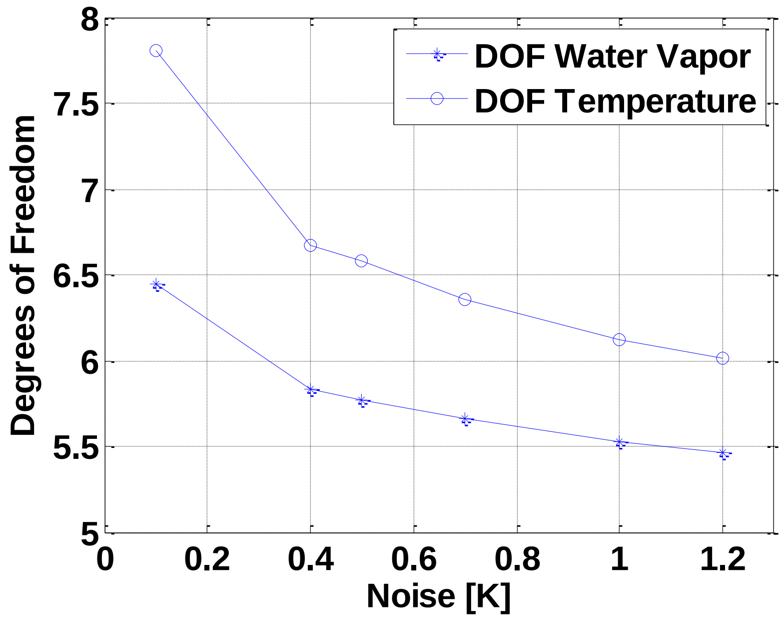

Figure 28: Variation in number of DOF for a range of instrument noise values for a zenith-pointing ground-based microwave radiometer.

The number of DOF decreases from 7.8 to 6 for temperature measurement frequencies while the number of DOF decreases from 6.45 to 5.5 for water vapor measurement frequencies as the instrument noise is increased from 0.1 to 1.2 K. Therefore, an increase in instrument noise has a negative effect on the number of DOF, as expected.

B. Effect of Variation in Measurement Uncertainty on the Number of DOF for an Airborne Radiometer

Airborne microwave radiometer measurements are affected by variations in atmospheric conditions as well as by the emissivity of the land and sea surfaces. Measurements performed by an airborne microwave radiometer can be represented by Eqn. (IV.14)

$$T_{B_{Measured}} = T_{B_{Ideal}} + \varepsilon_{T_B} \quad \text{(IV.14)}$$

where $T_{B_{Measured}}$ is the measurement, $T_{B_{Ideal}}$is the measurement due to atmospheric parameters and $\varepsilon_{T_B}$is the uncertainty associated with the measurement, representativeness error and radiative transfer model errors. The uncertainty in the measurement is due to the instrument noise and uncertainty associated with the land and sea surface emissivity as shown in Eqns. (IV.15) and (IV.16)

$$\varepsilon_{T_B} = \Delta T_B + T_{BSurface\ uncertainty} \quad \text{(IV.15)}$$

$$\varepsilon_{T_B} = \Delta T_B + (1-\epsilon)T_B^{\downarrow} + \epsilon T_{ph} + \varepsilon_r \quad \text{(IV.16)}$$

where ΔT_B is the uncertainty due to measurement noise, ϵ is the land emissivity, $T_B^{\downarrow}$ is due to down-welling brightness temperature measured at ground level, T_{ph} is surface temperature and ε_r represents the uncertainty due to representativeness error and radiative transfer model errors.

Emissivity models of land and sea surfaces can be used to reduce the emissivity uncertainty. However, some residual error will persist. The effect of uncertainty on the number of DOF of measurements is analyzed and is shown in Figure 29. The figure shows the variation in the number of DOF for 50 measurement frequencies when the measurement uncertainty is increased from 0.1 to 10 K the number of DOF decreases from 10.9 to 4.9 for water vapor measurement frequencies as the uncertainty is increased from 0.1 to 10 K. Similarly, the number of DOF for temperature measurement frequencies decreases from 6.7 to 2.2 as the uncertainty is increased from 0.1 to 10 K. Lower values of uncertainty estimate the effect of variation in sea surface emissivity. However, high values of uncertainty estimate the effect of variation in land surface emissivity.

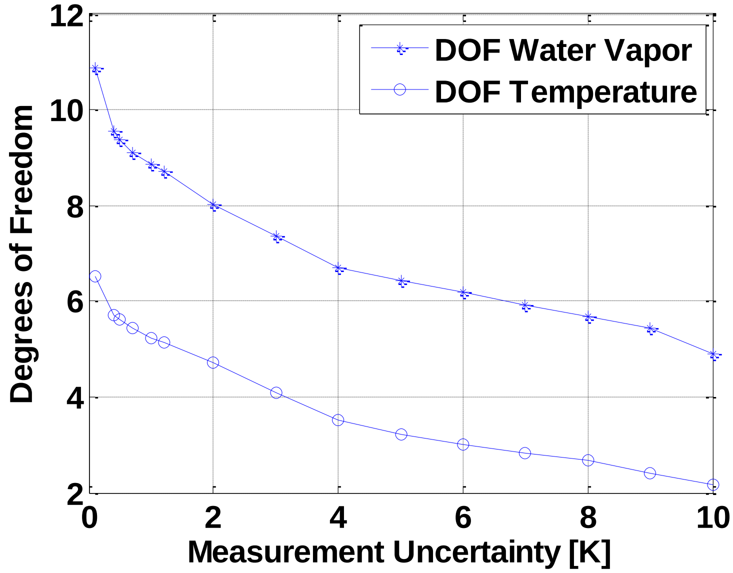

Figure 29: Variation in the number of DOF for a range of measurement uncertainties for a nadir-pointing airborne radiometer at 10 km above ground level.

C. Effect of Variation in Measurement Uncertainty on the Number of DOF and Vertical Resolution

The vertical resolution of the measurements has been optimized in Sections 4.3 and 4.4 using Backus-Gilbert method without taking the measurement error into account. Measurement error affects the vertical resolution as well as the number of DOF. Therefore, a study has been performed in which the measurement noise is varied from 0.1 to 1.2 K and its impact on number of DOF and vertical resolution at 2 km above ground level for a ground-based radiometer and 8 km above ground level for an airborne radiometer is analyzed for n = 2, 5, 7, 10 and 20 measurements. To include the impact of noise, the gain function is changed according to Eqn. (IV.17) and substituted into Eqn. (IV.9)

$$\bar{g}_a(z) = \frac{\left(\bar{\bar{Q}}_a(z) + \bar{\bar{S}}_\varepsilon\right)^{-1}\bar{u}}{\bar{u}^T\left(\bar{\bar{Q}}_a(z) + \bar{\bar{S}}_\varepsilon\right)^{-1}\bar{u}} \tag{IV.17}$$

The results of the analysis are shown in Figure 30 and Figure 31, which relate the number of DOF to vertical resolution for ground-based and airborne radiometers, respectively. The leftmost end of each curve in Figure 30 shows the case when the noise is maximum and the rightmost end of the curve shows the case when the noise is minimum. As the noise of the system is decreased, the number of DOF increases and the vertical resolution at 2 km above ground level improves.

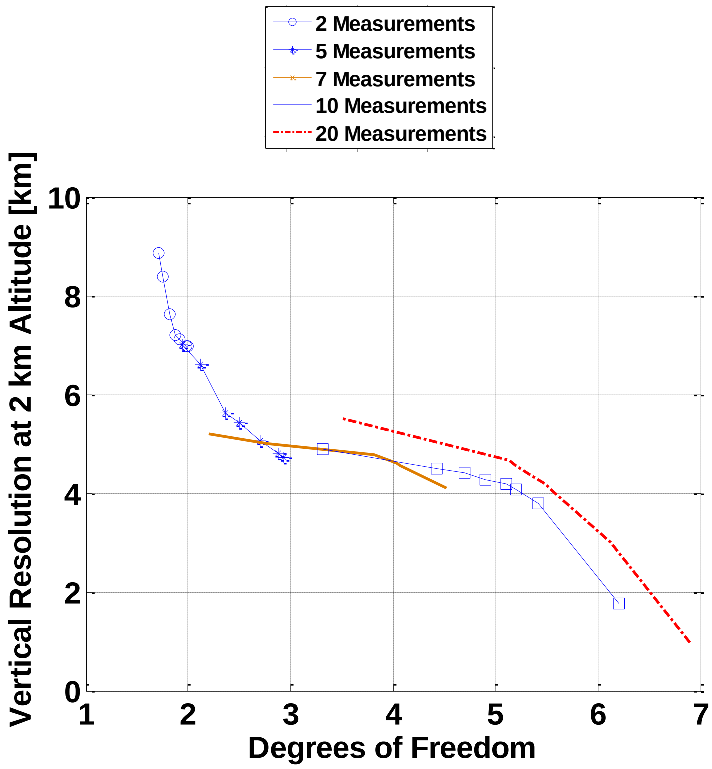

Figure 30: Variation in the number of DOF and vertical resolution with noise for zenith-pointing ground-based radiometer.

For two measurement frequencies for a ground-based radiometer, as the noise is reduced from 1.2 to 0.1 K, the number of DOF increases from 1.7 to 2 while the corresponding vertical resolution improves from 8.8 to 7 km. Similarly, for 7 measurement frequencies the number of DOF increases from 2.5 to 4.5 and the vertical resolution improves from 5.4 to 4. For 10 measurements, the vertical resolution improves from 4.8 to 1.7 km and the number of DOF increases from 2.8 to 6.3. For 20 measurements, the number of DOF increases from 3.5 to 6.9 while the vertical resolution improves from 5.6 to 1 km.

Figure 31 shows that for two measurements for airborne radiometer, as the noise is reduced from 1.2 to 0.1 K, the number of DOF increases from 1.7 to 2 while the corresponding vertical resolution improves from 5.6 to 4.6 km for 8 km above ground level. Similarly, for 5 measurement frequencies the number of DOF increases from 2.2 to 3.7 and vertical resolution improves from 4.6 to 3.5.

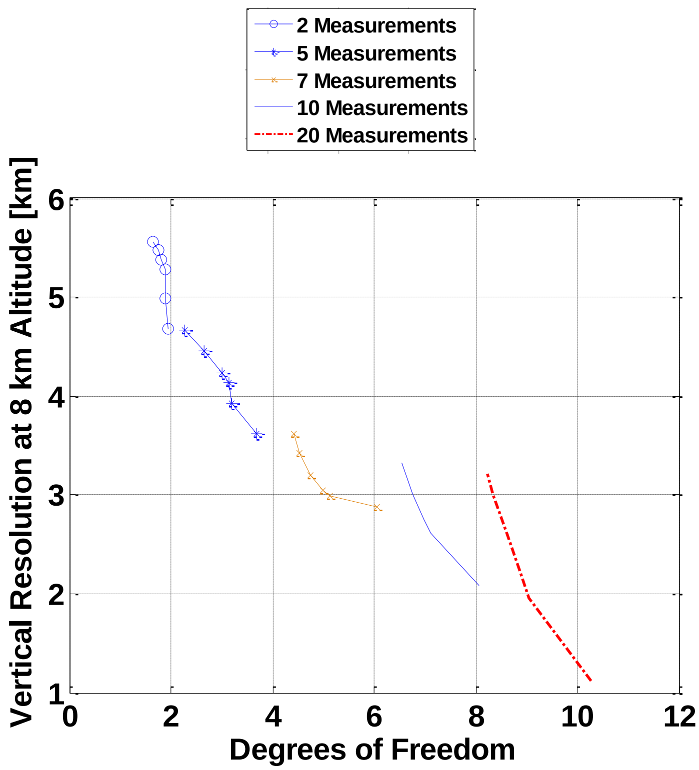

Figure 31: Variation in DOF and vertical resolution with noise for nadir-pointing airborne radiometer.

For 10 measurements, the vertical resolution improves from 3.6 to 2.9 km and the number of DOF increases from 4.5 to 6.1. For 20 measurements, the number of DOF increases from 8.5 to 10.9 while the vertical resolution improves from 3.6 to 1.2 km. These plots show that for assessing vertical resolution the important parameter is the number of DOF. Fewer frequency channels with smaller uncertainty have similar performance to a large number of frequency channels with greater uncertainty.

4.5. Orthogonalizing Water Vapor and Temperature Measurements

The feature selection method has been used to determine the frequencies that have the highest number of DOF in the frequency range 10 to 200 GHz. However, it is important to note that there are a number of frequencies in that range at which the measured brightness temperature has contributions from both water vapor and temperature. This is because the absorption lines for water vapor and temperature are sometimes similarly close to those frequencies, particularly in the window regions. Therefore, it becomes important to determine the particular frequency channels for measuring water vapor or temperature, i.e., the frequencies for which water vapor and temperature contributions are orthogonal, to identify those with contributions to brightness temperature from water vapor that are significantly larger than those from temperature, and vice-versa. To accomplish this, the percentage contribution to the brightness temperature due to water-vapor absorption is computed using Eqn. (IV.18).

$$\text{Percentage water vapor contribution} = \frac{T_{Bwv}}{T_{Btotal}} \times 100 = \frac{\rho . W_{wv}}{T . W_T + \rho . W_{wv}} \times 100 \tag{IV.18}$$

This relationship is used to compute the fractional contribution of water vapor to the total brightness temperature for each frequency. It has already been observed that water vapor provides a strong contribution to brightness temperature measurements in the frequency ranges of 20 – 23 GHz and 165 – 200 GHz.

These frequency ranges can be used to determine the major fractional contributing channels. To calculate the contribution, 10 radiosonde measurements were performed at the ARM site. The contribution from water vapor is shown in blue in Figure 32, and the contribution from temperature is shown in red. Frequencies in the ranges of 20 – 23, 80 – 108 and 175 - 184 GHz have water vapor contributions of more than 90%. Temperature contributes only 10% or less to the total brightness temperature in those frequency ranges. For the frequency ranges of 50 - 70 and 115 – 130 GHz the contribution due to temperature is stronger than that due to water vapor. Frequencies in the ranges of 57 – 60 and 115 – 121 GHz have temperature contributions of more than 90% and 60%, respectively. The results presented in Figure 32 are due to ground base radiometer. Similar results were also found for aircraft based instrument.

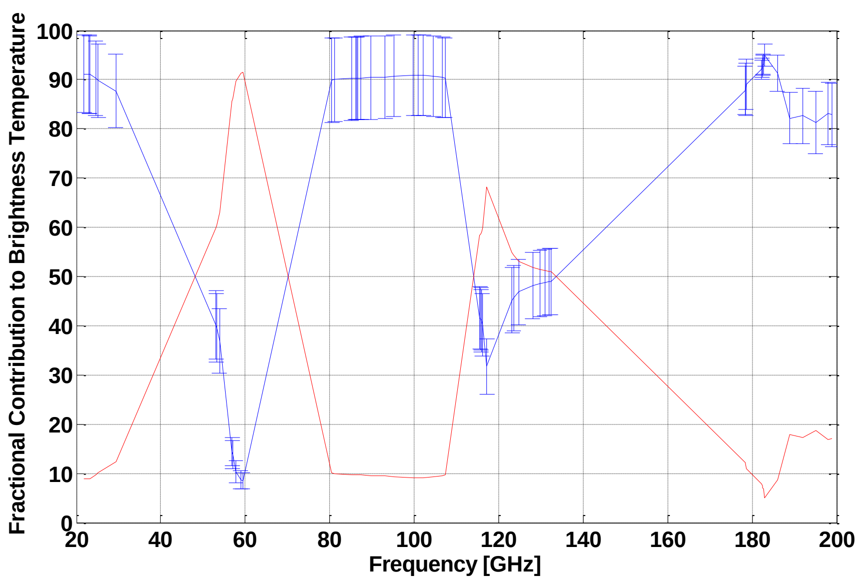

Figure 32: The fractional contributions of water vapor and temperature effects on total brightness temperature measurements.

4.6. Conclusions

Feature selection methods have shown that the frequency ranges of 20 – 23 GHz, 85 – 90 GHz and 165 – 200 GHz provide the maximum number of independent pieces of information for water vapor profile retrieval from zenith-pointing ground-based microwave radiometer measurements. The same frequency ranges are useful for water vapor profile retrieval from nadir-pointing airborne radiometers. On the other hand, for temperature profiling from ground-based measurements, the frequency ranges of 55 – 65 GHz and 116 – 120 GHz provide the maximum number of independent pieces of information. For temperature profile retrieval from nadir-pointing airborne measurements, nearly the same frequency ranges are needed, but the millimeter-wave frequency range is more narrowly focused near 118.75 GHz.

To determine the number of independent pieces of information and consequently the number of frequencies useful for retrieval of water vapor, the number of degrees of freedom has been determined for the selected frequencies in each case. From this analysis, it is found that a limited number of frequency measurements can be used to achieve fine vertical resolution and good accuracy of retrieved water vapor profiles. The maximum number of independent pieces of information is 5 – 6 for water vapor profiling and 6 – 7 for temperature profiling from zenith-pointing ground-based radiometer measurements. For nadir-pointing airborne measurements, the maximum number of independent pieces of information is 8 – 9 for water vapor profiling and 5 – 6 for temperature profiling. If additional measurement frequencies are chosen beyond these limits, they will provide redundant information since that information is linearly dependent on that already measured at other frequencies. Noise analysis has shown that increasing measurement uncertainty and instrument noise reduce the number of DOF. Similarly, measurement uncertainty degrades the vertical resolution. It was also found that vertical resolution is directly related to the number of DOF.

Chapter V Optimization of Background Information for Retrieval Algorithms Using Ground Based Microwave Radiometer Measurements

This chapter explores the potential to use ground-based, zenith-pointing K-band radiometer measurements along with optimized background data sets consisting of radiosonde profiles to detect dynamic changes and gradients in water vapor profiles. To explore this capability, the HUMidity EXperiment 2011 (HUMEX11) was conducted at the U.S. Department of Energy's (DOE) Atmospheric Radiation Measurement (ARM) Southern Great Plains (SGP) site near Lamont, OK, USA.

The results illustrate that in a retrieval algorithm the choice of the size of the background data set measured near the radiometer measurement time and the choice of atmospheric layer thickness affect the ability to remotely sense dynamic changes in water vapor. In general, it is found that background data sets of larger size provide better accuracy in a statistical sense but inhibit the ability to detect gradients.

5.1. Introduction

Tracking dynamic changes in water vapor profiles is important to predict the timing and location of cloud formation as well as the initiation of convective storms. These storms develop on a time scale of 30 to 60 minutes in locations where the water vapor is highly variable [60] [61] [62]. Since convective initiation is highly sensitive to the amount of total column or, equivalently, precipitable water vapor (PWV), it is important to remotely sense PWV with fine temporal and spatial resolution. In particular, water vapor profile measurements with fine resolution in the planetary boundary layer are needed to analyze detailed, dynamic changes in the atmosphere [63].

Instruments currently used to measure water vapor profiles include radiosondes and Raman lidar as well as microwave radiometers. Radiosondes provide water vapor measurements with fine vertical resolution (on the order of a few tens of meters) for the initialization of numerical weather prediction (NWP) models. However, the repeat time of radiosonde launches is not sufficient to track the dynamic evolution of tropospheric water vapor. Another instrument that can provide profile information to improve NWP models is Raman lidar [64]. These measurements have similar vertical resolution to that of radiosondes in the lowest 3 km of the troposphere and have temporal resolution of approximately 10 minutes [65]. Infrared radiometers, such as atmospheric emitted radiance interferometers (AERI), are useful for retrieval of water vapor and temperature profiles. Similarly, satellite based microwave radiometer measurements are used to determine precipitable water vapor, water vapor profiles, cloud liquid water and wet path delay. Finally, ground-based microwave and millimeter-wave radiometers operate at frequencies near the water vapor absorption lines at 22.235 GHz and 183.31 GHz, respectively, to retrieve water vapor profiles [66] [43]. These instruments have fine temporal resolution; however, the accuracy of retrieved profiles varies depending on the retrieval algorithm and the thermodynamic parameter being retrieved. Westwater [28] described various retrieval techniques for estimation of water vapor and temperature profiles. Solheim [16] compared the performance of various retrieval algorithms i.e., Newtonian iteration method, regression method, neural networks and Bayesian maximum probability estimation technique, for retrieval of water vapor, temperature and liquid water profiles. Cimini et al. [66] and Hewison [12] focused on quantifying and improving the vertical resolution of retrieved water vapor and temperature profiles. Scheve and Swift [17] compared water vapor profiles retrieved from K-band microwave brightness temperature measurements to those retrieved from Raman lidar measurements.

Here, water vapor profiles are retrieved from K-band radiometer measurements using Bayesian optimal estimation [14] with an emphasis on detecting water vapor gradients in the lower troposphere that are dynamically evolving. For that purpose, background data sets of varying sizes are used to determine the statistical variability of atmospheric water vapor. The retrieved profiles are compared with water vapor profiles retrieved from a co-located Raman lidar. These Raman lidar measurements are assumed to be of high enough quality to be taken as "truth". Therefore, the error is defined as the difference (i.e., deviation from "truth") between a profile retrieved from microwave radiometer measurements and that retrieved from Raman lidar.

5.2. Humidity Experiment 2011

The HUMidity EXperiment 2011 (HUMEX11) was conducted at the U.S. Department of Energy (DOE)'s Atmospheric Radiation Measurement (ARM) Southern Great Plains (SGP) Climate Research Facility in Lamont, OK for three weeks in the summer of 2011, during the periods of July 7-15 and August 3-15.

5.2.1 Purpose and Goals

This field campaign was designed to assess the ability to remotely sense dynamic changes and gradients in atmospheric water vapor profiles retrieved from K-band microwave brightness temperatures and to compare them with water vapor profiles retrieved from Raman lidar. Measurements were performed under various atmospheric conditions during clear skies, including stable conditions as well as rapidly evolving conditions shortly after rain showers in the area. The measurements were performed after a total rainfall of 12 to 40 mm over 6 to 12 hours on certain days and when the water vapor density in the lowest 1 km above ground level (AGL) was between 8 and 19 g/m^3. These weather conditions are typically associated with high water vapor variability, providing a wide range of conditions for tuning water vapor estimation techniques and sensing dynamic changes in water vapor profiles. After precipitation events, the radiometer was operated after the sky was clear and clouds had moved out of the radiometer's field of view. Target accuracies for the retrievals were similar to the requirements shown in Table 5 for the planned National Polar-orbiting Operational Environmental Satellite System (NPOESS) Conical-Scanning Microwave Imager/Sounder (CMIS), which was canceled due to cost and schedule overruns [67].

Table 5. Requirements based on the Algorithm Theoretical Basis Document for the planned but canceled NPOESS Conical-Scanning Microwave Imager/Sounder (CMIS) and for the ground-based GPS network deployed at the ARM SGP site [68].

	Height Above Ground Level	**Water Vapor Uncertainty (in clear conditions)**
NPOESS	From ground to 4 km	20% or 0.2 g/kg
	From 4 km to 9 km	35% or 0.1 g/kg
GPS	From ground to 3 km	20% or 0.2 g/kg
	From 3 km to 6 km	30 – 35% or 0.15 g/kg

5.2.2 Experiment Description and Measurements Performed

During HUMEX11, two K-band, multi-frequency Compact Microwave Radiometers for Humidity profiling (CMR-H) [21] [5] were deployed at the ARM SGP site. One of the two was co-located with a Raman lidar, enabling precise comparisons of profiles retrieved from the K-band brightness temperatures to those retrieved from the Raman lidar data. The other radiometer was deployed 10 km to the northwest, near Lamont, OK. The map showing location of radiometers is shown in Figure 33 and the pictures showing the deployment of the radiometers are shown Figure 34.

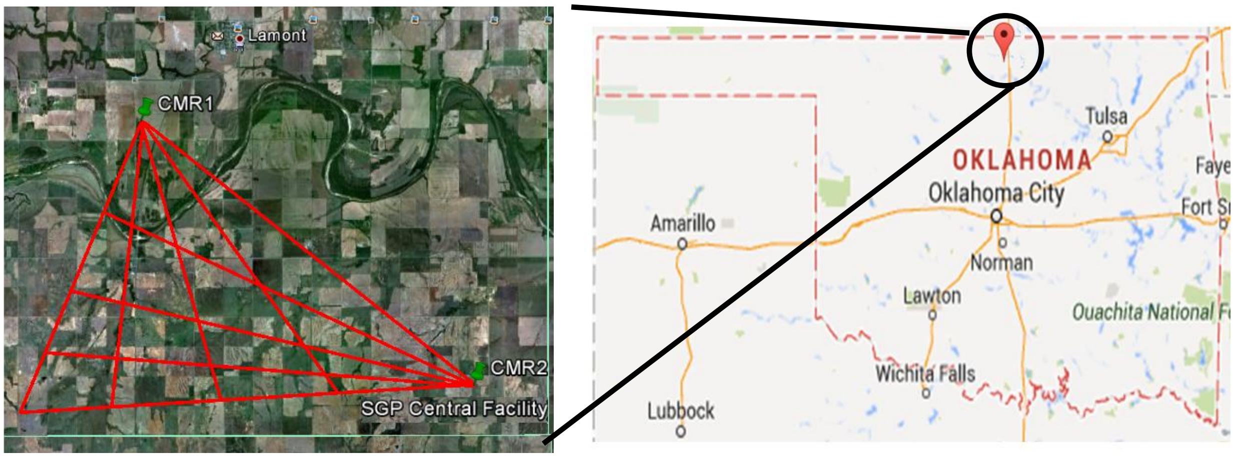

Figure 33. (Left) Map showing the location of the radiometers in Oklahoma, USA. (Right) Zoomed out view of the HUMEX11 site in Oklahoma, USA.

These microwave radiometers sampled atmospheric volumes using mechanical scanning over a range of both elevation and azimuth angles. Data measured during HUMEX11 was used to retrieve water vapor profiles.

The CMR-H K-band radiometers were developed at the Microwave Systems Laboratory (MSL) in the Electrical and Computer Engineering Department at Colorado State University (CSU) using Monolithic Microwave Integrated Circuit (MMIC) technology with a low noise amplifier-based front-end [21]. The radiometers operate at four frequencies near the K-band water vapor absorption line, i.e. 22.12, 22.67, 23.25, and 24.5 GHz with bandwidths of 110, 120, 120 and 200 MHz, respectively.

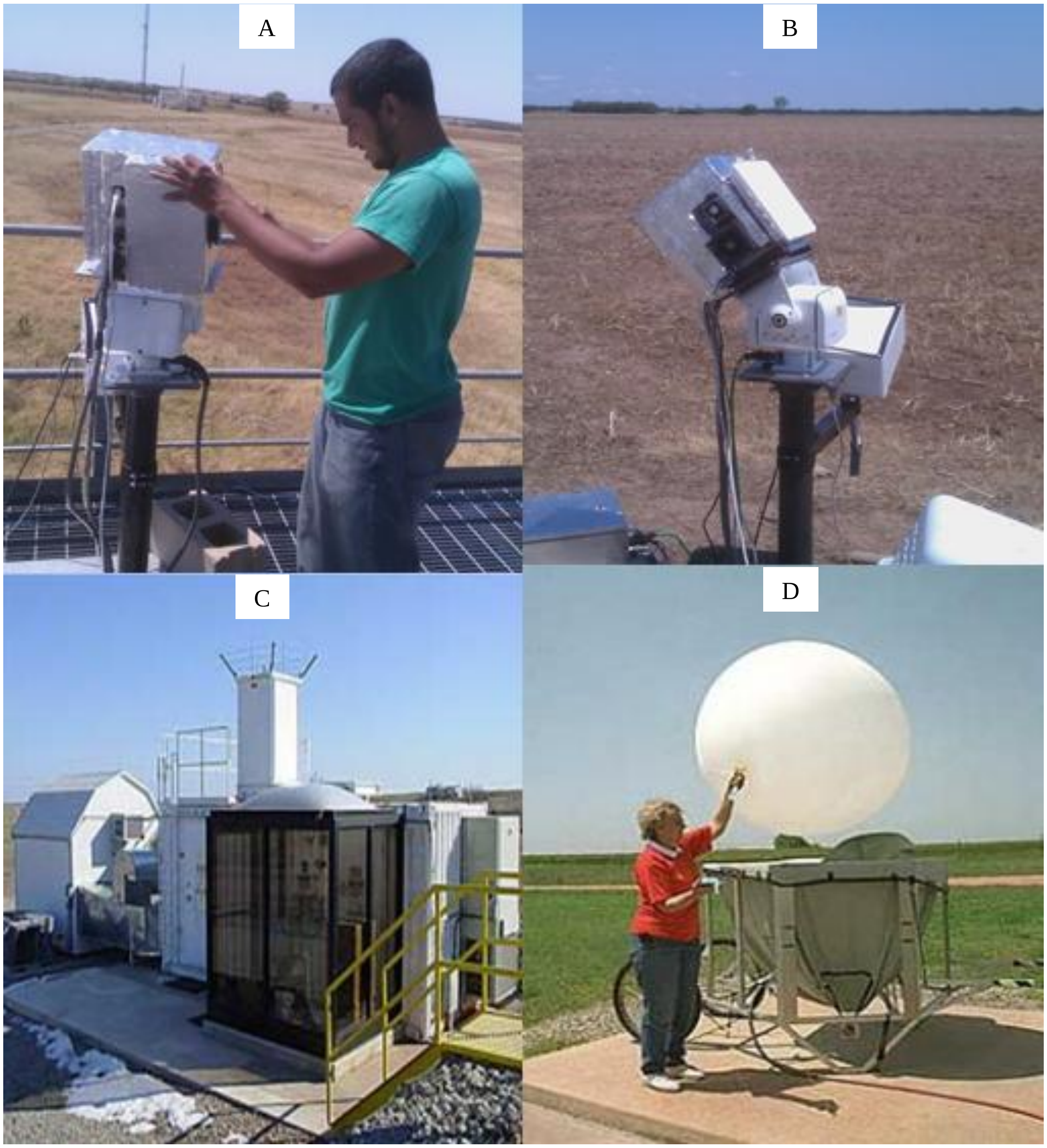

Figure 34. (A) Deployment of a Compact Microwave Radiometer for Humidity profiling (CMR-H) (B) Tipping curve (C) Raman lidar and (D) Launch of radiosonde at the ARM Southern Great Plains (SGP) Central Facility during HUMEX11

Jacobians, or weighting functions, for these frequencies are shown in Figure 35. The profile used to calculate this weighting function is based on the average profile measured by radiosondes launched from the ARM SGP site on August 8, 2011. The radiometric resolution (ΔT) of the CMR-H is 0.2 K for a 3-s integration time. The 3-dB antenna beamwidth for CMR-H is 3-4°. The radiometer's system noise temperature at the four measurement frequencies is in the range of 550 – 800 K. The calibration precision at 298 K (while observing a microwave absorber at ambient temperature) is approximately 0.2 K for all four frequencies [69].

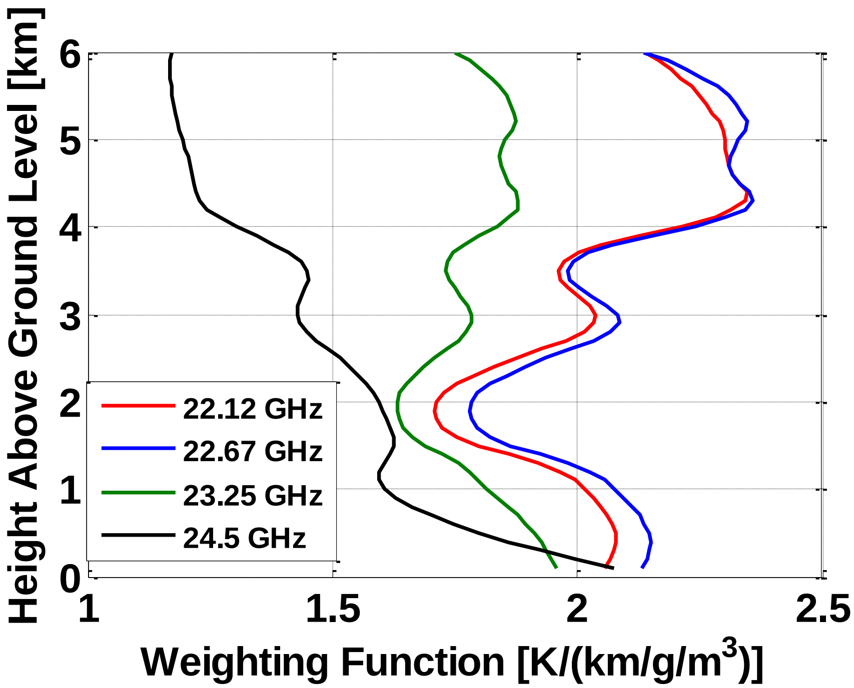

Figure 35: Jacobian or Weighting functions for CMR-H frequencies.

Calibration of the CMR-H brightness temperature measurements is performed by observing two objects of known brightness temperature. The “hot” calibration target is a microwave absorber at ambient temperature, and the “cold” calibration source is the cosmic microwave background temperature of 2.73 K at these frequencies, using tipping curve measurements extrapolated to zero atmospheres [70]. While performing a two point calibration the radiometer measures two different scenes of known temperatures $T_{A,1}$ and $T_{A,2}$, which are related to the measured voltage by the Eqns. (V.3) and (V.4)

$$V_{output,1} = aT_{A,1} + b \tag{V.1}$$

$$V_{output,2} = aT_{A,2} + b \tag{V.2}$$

- $V_{output,1}$ and $T_{A,1}$ correspond to measurement and antenna temperature while looking at the microwave absorber

- $V_{output,2}$ and $T_{A,2}$ correspond to the extrapolated value of measurement and cosmic background temperature of 2.73 K, respectively.
- a is the calibration gain and b is the offset.

The value of a and b can be calculated by using Eqns. (V.3) and (V.4),

$$a = \frac{V_{output,1} - V_{output,2}}{T_{A,1} - T_{A,2}} \tag{V.3}$$

$$b = \frac{T_{A,1}V_{output,2} - T_{A,2}V_{output,1}}{T_{A,1} - T_{A,2}} \tag{V.4}$$

For determining $V_{output,2}$ corresponding to cosmic background temperature $T_{A,2}$, six zenith angle scans at 0°, 25°, 35°, 50°, 55°, 65° and 70° were performed under clear sky conditions. Those zenith angles correspond to 1, 1.1, 1.22, 1.47, 1.7, 2.1 and 2.6 air masses. Measured voltages at the zenith angles are used to extrapolate to a voltage for zero air mass which corresponds to cosmic background temperature of 2.73 K, similar to a radiometer looking upward at the top of the atmosphere. The results of tipping curve calibration for the CMR-H frequencies are shown in Figure 36.

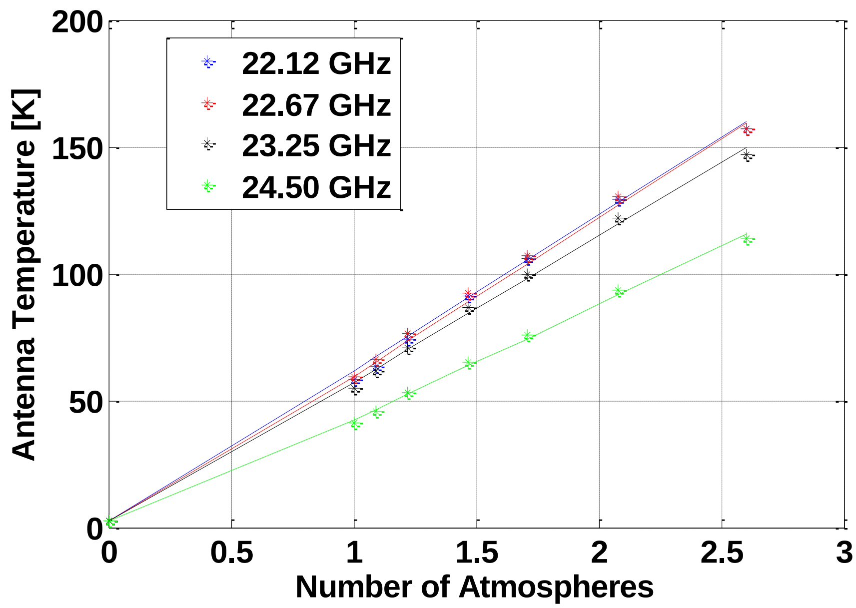

Figure 36. Tipping-curve calibration performed at the four frequencies of CMR-H

Furthermore, additional instruments were deployed at the ARM SGP site, including wind profilers [71], an atmospheric emitted radiance interferometer (AERI) [6], microwave radiometers [72] [73] [51] [74], and in-situ weather station sensors. Radiosondes were launched from the ARM SGP Central Facility every six hours. This provides an opportunity to compare the retrieved results with data from other co-located instruments.

5.3. Sensitivity of Retrieved Water Vapor Profiles

The atmospheric layer thickness and background data set size have a substantial effect on the root mean square (RMS) error and on the ability to detect dynamic changes in the retrieved water vapor profiles.

5.3.1 Water Vapor Profile Retrievals for Different Layer Thicknesses

The retrievals were performed for 100-, 200-, 400- and 500-m layer thicknesses using the data sources mentioned in Section 3.1.2 as well as the initialization profile. As alluded to in Section 3.1 of, initialization profiles were obtained from radiosonde data, with a typical vertical resolution of 10 to 20 m. The initialization profiles were vertically averaged to correspond to the layer thickness of the retrieval. For example, when using an initialization profile of 100-m layer thickness for the retrieval, the radiosonde water vapor profile was vertically averaged to 100 m [41].

The background data set here consists of measurements from 64 radiosondes that were launched during the daytime at the ARM SGP site during the months of July and August, 2011. Radiosonde data from these two months were used as two separate background data sets for retrievals during each of the two respective months. Results described in Sections 5.3 to 5.4 are for 40 retrieved profiles using measurements performed over three weeks during the field experiment. These profiles were retrieved using various layer thicknesses and compared with Raman lidar profiles to quantify the RMS error for each of them. Figure 37 (a) shows a profile retrieved for August 9, 2011 at 17:50 UTC from Raman lidar measurements. Data from radiosonde launched at 16:30 UTC is used as the *a-priori* for the retrieval of the water vapor profile from the radiometer measurements. Ground-based in-situ measurements were used throughout this study to constrain the surface temperature, humidity and pressure for the retrieved profile.

To calculate the error as a function of height, the Raman lidar-retrieved values have been averaged to the same vertical layer thickness as the radiometer estimates. Figure 37 (b) shows the associated difference between radiometer-retrieved and Raman lidar-retrieved profiles for 100-m, 200-m, 300-m and 500-m layer thicknesses, showing that this difference is larger than 1 g/m^3 for layer thickness of 100 and 200 m in the lowest 2.2 km of the troposphere.

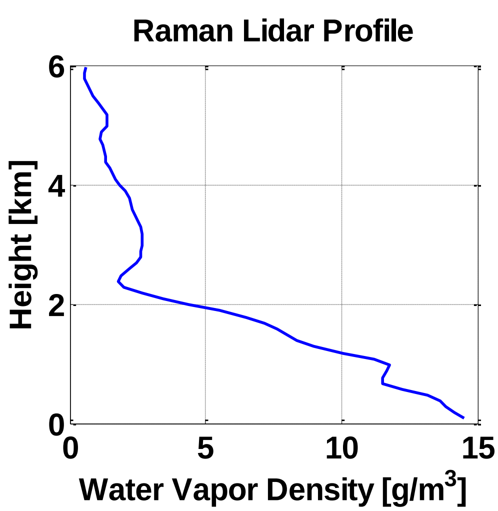

(a)

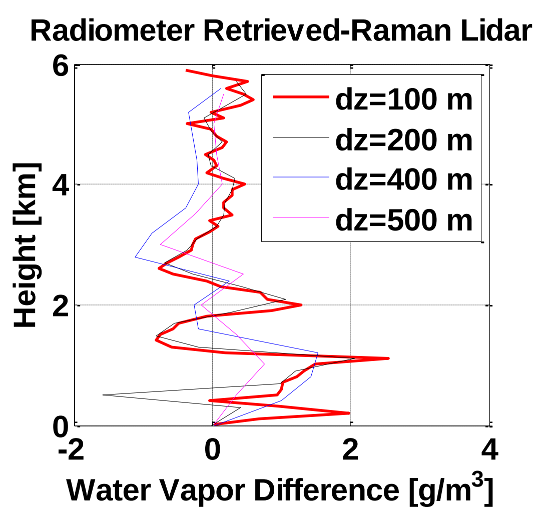

(b)

Figure 37: (a) Raman lidar profile at 17:50 UTC on August 9, 2011; (b) difference between radiometer-retrieved and Raman lidar-retrieved profiles for 100-, 200-, 400- and-500 m layer thicknesses.

This difference decreases with increasing altitude above ground level. As the layer thickness is increased, the difference decreases as well. The profiles with 400 and 500 m layer thickness significantly smooth out the vertical variations in the water vapor profile, thereby reducing the error. The errors in the retrieved profile with respect to the Raman lidar profile averaged over the lowest 3 km of troposphere, i.e. the most significant part of the atmosphere in terms of water vapor variability, are 19.3%, 16.7%, 13.9% and 8.2% for 100-m, 200-m, 400-m and 500-m layer thicknesses, respectively. The total error of a profile (hereafter "total percentage error in PWV") was determined as the sum of the absolute values of errors at all levels up to and including 6 km AGL. The total errors of 40 estimated profiles are used to determine the mean and standard deviation of the total percentage error for each layer thickness from 100 m to 500 m in 50-m increments. The results are shown in Figure 38. As the layer thickness increases from 100 m to 500 m, the mean total percentage error decreases from 27% to 13% and the standard deviation decreases from 4.5% to 2.3%. Figure 38 shows an inverse relationship between the layer thickness and the total percentage error. In other words, the thinner the atmospheric layers are, the greater the overall estimation error is.

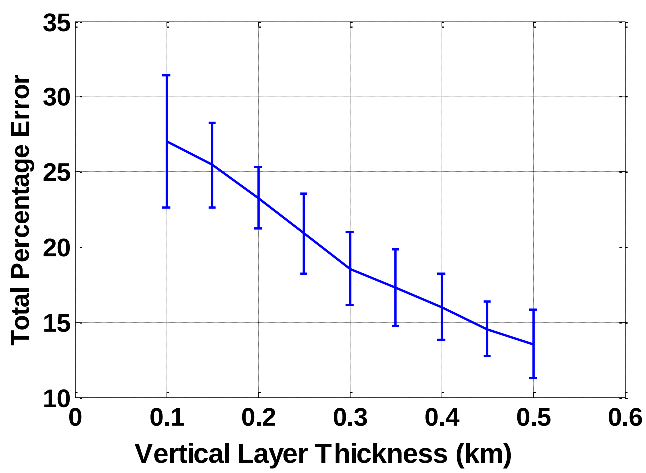

Figure 38: Mean total percentage error in PWV (calculated as the difference between radiometer-retrieved and Raman lidar-retrieved water vapor profiles) as a function of layer thickness using 64 radiosonde observations as background information.

The accuracy of retrieved profiles depends to a great extent on the quality of the initialization profile, background information and measurement error covariance matrices.

Typically, the retrieved profile follows the trend of the initialization profile. If the initialization profile (here the radiosonde profile used for the retrieval) is substantially different from the actual water vapor profile, the error of the retrieved profile will be large. In that case, the retrieval process might not be able to capture gradients or aspects of the actual water vapor profile. So, the initialization profile needs to have statistical properties that are similar to those of the actual profile.

5.3.2 Variation in Predictability with Change in Background Data Set Size and Atmospheric Layer Thickness

The retrieval accuracy has been evaluated based on the mean and standard deviation of total percentage error in the retrieved water vapor profiles for background data set sizes ranging from two to 110 profiles. A background data set containing less than 10 profiles does not have sufficient statistical significance, but the analysis has been performed to improve understanding of its impact on the retrieval. The covariance matrices were calculated using background data sets containing two to 110 profiles with an increment of two. Each increment added one profile taken before the measurement and one taken after. These profiles were chosen to be as close to the time of measurement as possible. For example, for the radiometer measurement at 14:00 UTC on August 8, 2011, the two radiosonde profiles chosen were at 12:00 UTC and at 18:00 UTC on August 8, 2011. The radiosondes were launched four times daily at 0, 6, 12 and 18 UTC. If two additional profiles were added to the data set, to use similar times of day to represent diurnal conditions similar to when the radiometer measurement was taken, they would be at 18:00 UTC on August 7, 2011, and at 12:00 UTC on August 9, 2011, and so on. This method of choosing an equal number of radisonde profiles before and after the retrieval time is particularly applicable to this study. This would not be possible if the radiometer measurements were used to retrieve water vapor profiles on a real-time basis. In that case, radiosonde profiles taken before the retrieval time would be available for use as the background data set.

For small background data set sizes, the time interval between initialization profile and retrieved profile has a substantial impact on the retrieval accuracy. The ability to detect changes in retrieved water vapor profiles is partially determined by the size of the background data set used and by the quality and applicability of the *a-priori*. The accuracy depends to a certain extent on the background data set size and also on the time interval between the radiometer measurement and the radiosonde profiles in the background data set as well as the layer thickness used for the retrieval. Therefore, the accuracy of the retrieval for a variety of background data set sizes is analyzed for varying layer thicknesses. This analysis involved using a background data set taken close in time to the radiometer measurement so that the background information covariance matrix would be representative of the variability near this time.

As before, water vapor profiles were retrieved for 40 measurement times while varying the layer thickness from 100 to 500 m as well as the size of the background information covariance matrix from two to 110. Figure 39 (a), 39 (b) and 39 (c) show the mean error and its' standard deviation (shown by the curve and error bar, respectively) calculated using 40 retrievals for data set sizes of 16, 32 and 64, respectively, and layer thicknesses of 100 m (left panel), 250 m (middle panel) and 500 m (right panel). Figure 39 shows that, for any particular layer thickness studied, as the size of the background data set increases, the bias of the retrieval decreases. For any particular background data set, as the layer thickness is increased the uncertainty of retrieval also decreases. In addition, there is an optimum data set size for minimum standard deviation. The bias is related to the mean error, and the standard deviation is related to the uncertainty of the retrieval. Figure 39 shows that the results are consistent with the qualitative discussion in Section 3.1.3.

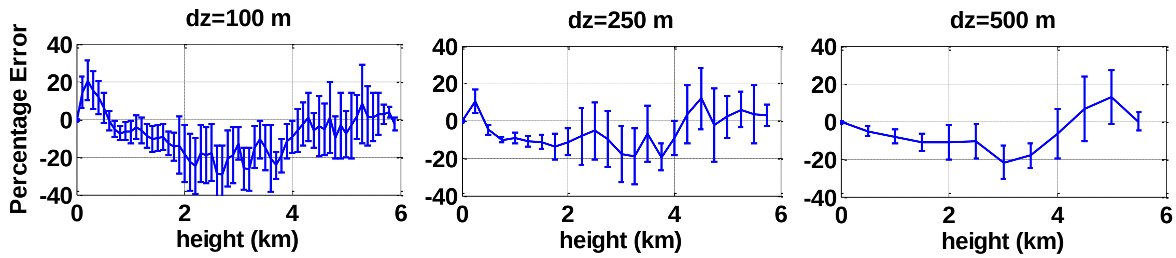

(a)

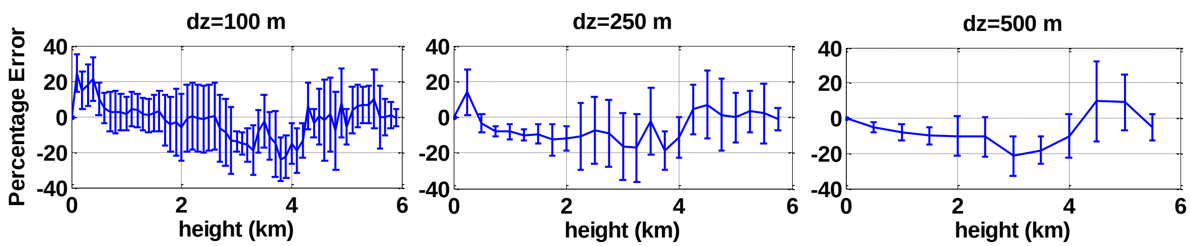

(b)

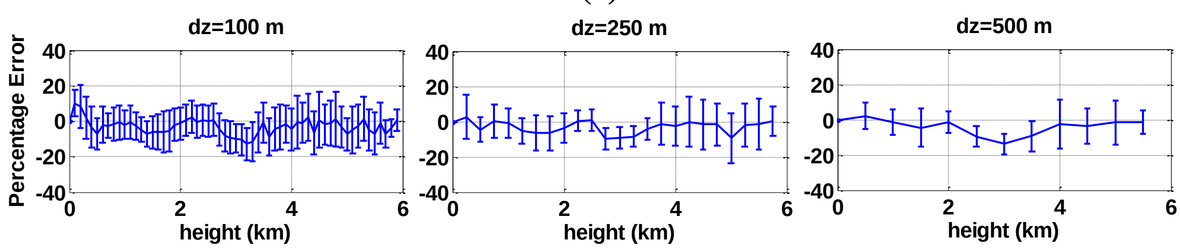

(c)

Figure 39: Mean and standard deviation percentage error radiometer-retrieved of profiles with respect to Raman lidar-retrieved water vapor profiles for 100-m, 250-m and 500-m layer thickness and background data set sizes of (a) 16 elements, (b) 32 elements, and (c) 64 elements.

5.3.3 Change in Total Percentage Error with Change in Background Data Set Size

This study was performed to find the optimal background data set size to minimize the total percentage error while maintaining the ability to detect changes in the gradients of the water vapor profile. The total percentage errors were calculated for retrievals using each background data set size, where the background data set was taken close to the radiometer measurement time. The mean and standard deviation of percentage errors for data set sizes from two to 110 (as well as 1500) are shown in Figure 40 as red and blue curves for layer thicknesses of 100 m and 500 m, respectively.

A. Total Percentage Error for 100-m Layer Thickness

Figure 40 shows that for a 100-m layer thickness and a background data set size of four, the total percentage error is 38.5%. Although the background covariance matrix calculated from a data set of 4 profiles is not statistically significant, it has been included in the study for completeness. The mean total error decreases as the background data set size increases and reaches a minimum of 27% for a background data set size of 40. This is because the retrieved profiles are stationary with respect to the background data set of 40 profiles, and the background data set is related to the current atmosphere. When the size of the background data set taken close in time to the radiometer measurement is 40 for 100-m layer thickness, it is inferred from the minimum error that the statistics used in the covariance matrix agree with the variability associated with the actual water vapor profile. Throughout Figure 40, the standard deviation associated with each percentage total error is shown by the error bars. The total error increases when the background data set size is greater than 40 profiles because the retrieved profile is no longer stationary with respect to the background data set, and the weather conditions associated with the background data set are different from those during the radiometer measurement. The *a-priori* statistics do not describe the water vapor profile accurately since the background atmospheric conditions have changed.

For a data set size larger than a certain threshold, i.e. 1500 profiles as shown in Figure 40, the mean error becomes nearly constant at 36% mean total error, as shown by the long dashed red horizontal line. Similarly, when a Markov covariance matrix, which emulates a synthetic atmosphere [14], is used as a background information matrix, the mean error is 42%, as shown by the short-dashed red horizontal line. The total error would not have this trend if the selected data set for background covariance matrix calculation was not related to the atmospheric condition during the measurement.

B. Total Percentage Error for 500 m Layer Thickness

Similar to Section 5.3.3 (A), Figure 40 shows that the error for 500-m layer thickness and a background data set size of four has a total percentage error of 17%, while the background covariance matrix for a data set size of four is not statistically significant but is used for completeness. The error decreases as the background data set size increases until it reaches a minimum of 9% for a data set size of 50–55. After the total error reaches a minimum, it then begins to increase as the number of profiles in the background data set increases. The error becomes nearly constant at 13% (as shown in the long-dashed blue horizontal line) for a background data set size of 1500 or greater, due to the stationarity effect discussed in Section 5.3.3 (A).

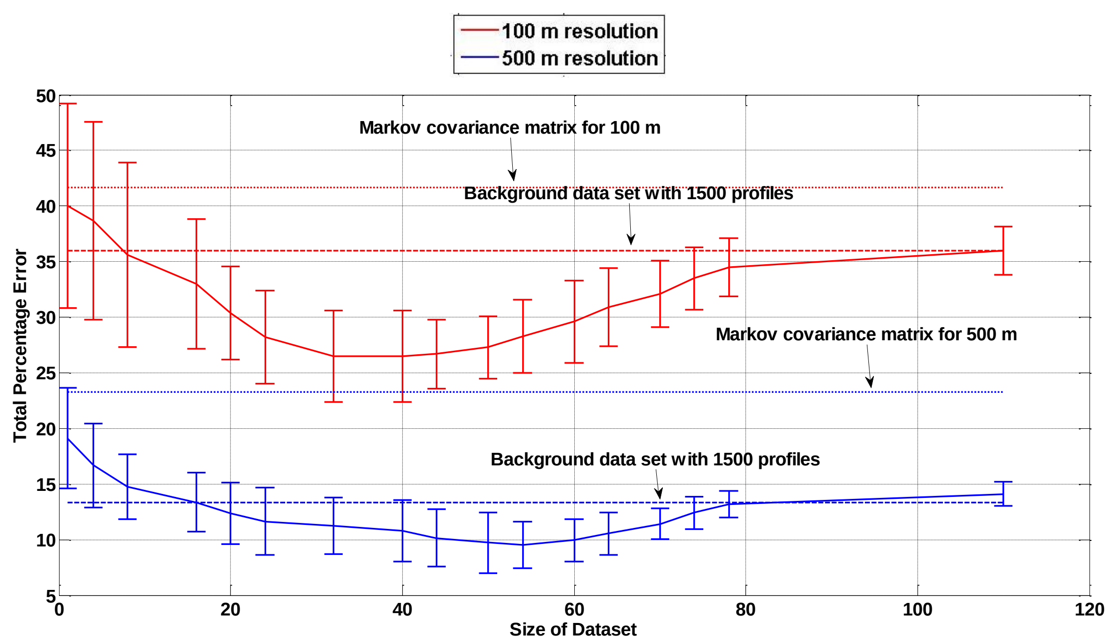

Figure 40: Mean total percentage error and its' standard deviation for retrieved profile (for layer thicknesses of 100 m and 500 m) as a function of the size of the background data set. The total percentage error for a background data set size of 1500 (for layer thicknesses of 100-m and 500-m) is represented by red and blue horizontal lines at 36% and 13%, respectively.

The mean error using a Markov covariance matrix as the background covariance matrix for 500-m layer thickness is 23% as shown by the short-dashed blue horizontal line. It is important to observe that the retrieval errors for 500-m thick layers are lower than for 100-m thick layers. However, the retrieval for 500-m layer thickness not only averages the error associated with the retrieval but also averages the important information about dynamic changes. To retrieve information about dynamic changes, it is better to use 100-m layers instead of 500-m layers.

A similar analysis was performed by using a background data set which was taken from the September 2008 and the background data set size was varied from 2 to 110 to determine the total mean error. The results of this analysis are shown in red in Figure 41 for 500-m layer thickness. The mean total errors are substantially larger than those when the background data set is taken close to the measurement time during July and August of 2011. This is because the background data set taken from 2008 is not stationary with the atmospheric water vapor during the radiometer measurement.

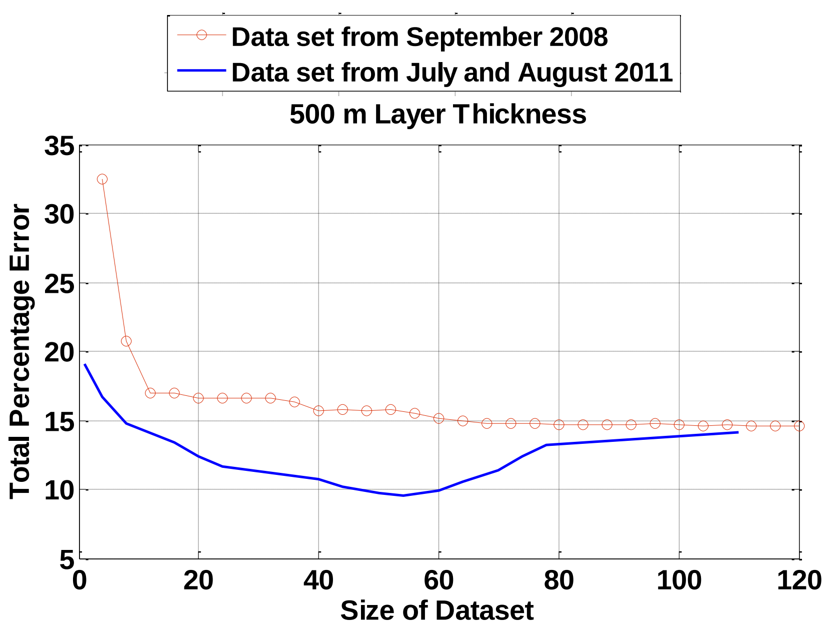

Figure 41: Mean total percentage error and its' standard deviation for retrieved profile (for layer thickness of 500 m) as a function of the size of the background data set.

The difference between the errors in Figure 41 is largest at 16% for a background data set size of four and decreases as the background data set size is increased. The difference is smallest when the background data set size is larger than 110 profiles. This is because the variability between data sets of four profiles taken at two different times is very different. However, the variability between data sets of 110 profiles from two different times tends to be quite similar.

C. Analysis of Variability Content Associated with Background Information Covariance Matrix

The covariance matrix ($\bar{\bar{S}}_a$) is computed using Eqn. (V.5):

$$\bar{\bar{S}}_a = E(\bar{\bar{A}} - \langle\bar{\bar{A}}\rangle)(\bar{\bar{A}} - \langle\bar{\bar{A}}\rangle)^T \tag{V.5}$$

where $\bar{\bar{A}}$ is the background data set and $\langle\bar{\bar{A}}\rangle$ represents the mean profile computed from the background data set.The matrix $\bar{\bar{S}}_a$ has dimension of *NxN*, where *N* is the number of layers (vertical levels) regardless of the number of profiles that has been used to calculate it (in this study, *N*=60 for each of 100-m and *N*=12 for 500-m layer thicknesses). As the size of the background data set is increased, the elements of $\bar{\bar{S}}_a$ also change. Figure 42 shows the $\bar{\bar{S}}_a$ for 100-m layer thickness using background data set with 2, 40, 60 and 1400 profiles.

An eigenvalue analysis [16] of the background information covariance matrix was performed to determine its variability content for the purpose of detecting dynamic changes in the water vapor profile while minimizing the error. For the eigenvalue analysis, the length of $\bar{\bar{A}}$ is increased from two to 110 using the background data set measured during HUMEX11 and $\bar{\bar{S}}_a$ is calculated for each background data set ($\bar{\bar{A}}$) size. The eigenvalue analysis of the covariance matrix corresponding to each background data set gives a vector of *N*-eigenvalues. When the background data set size is varied from 2 to 110, it results in 109 vectors of *N*-eigenvalues each. The results presented here show the normalized eigenvalue trajectory [17] for the covariance matrices for layer thicknesses of 100 m and 500 m for Figure 43(a) and Figure 43(b), respectively.

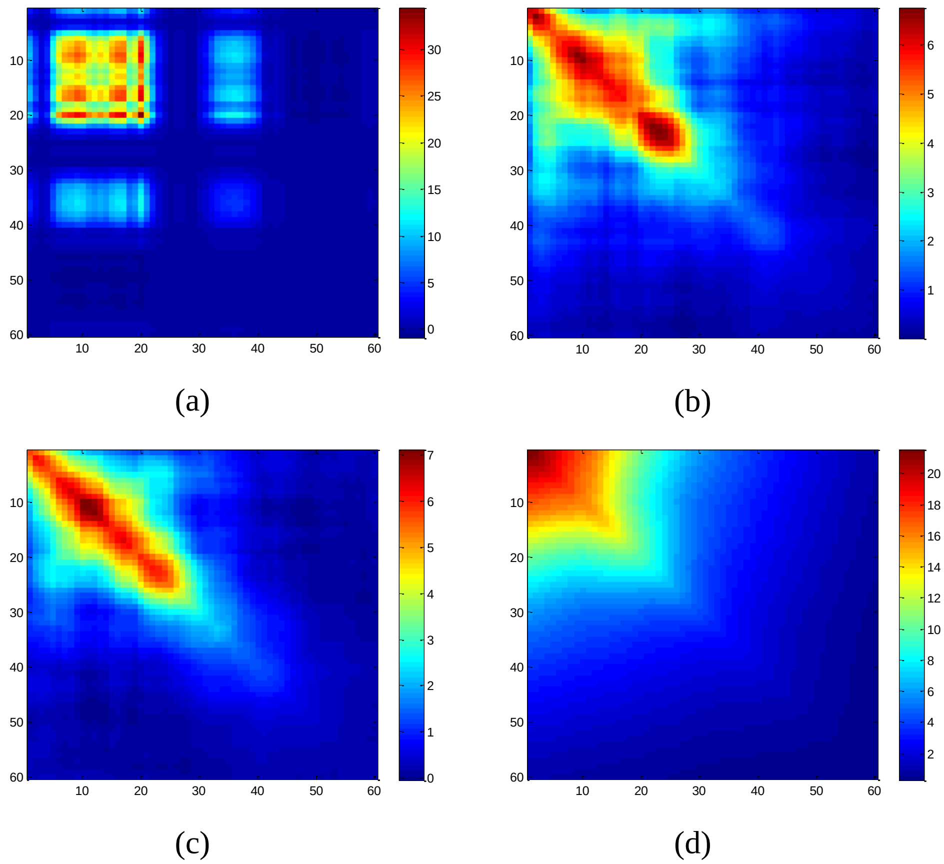

Figure 42: Covariance matrix ($\bar{\bar{S}}_a$) calculated for 100-meter layers (N=60) using (a) two profiles, (b) 40 profiles, (c) 64 profiles and (d) 1000 profiles.

The number of curves corresponds to the N layers in the retrieval, while each curve extends from two to 110, i.e. the number of profiles used to calculate $\bar{\bar{S}}_a$. Trajectories of each curve represent the evolution of the eigenvalues as the background data set size increases, where each curve (e.g., red, green, and blue curves Figure 43(a)) represents the trajectory of an individual normalized eigenvalue corresponding to one atmospheric layer as the number of profiles is increased from two to 110. In Figure 43, as the number of water vapor profiles in the background data set is increased, the eigenvalue increases and reaches a maximum at approximately 25-35 and remains above 0.8 for about 35 profiles for both 100-m and 500-m layer thicknesses.

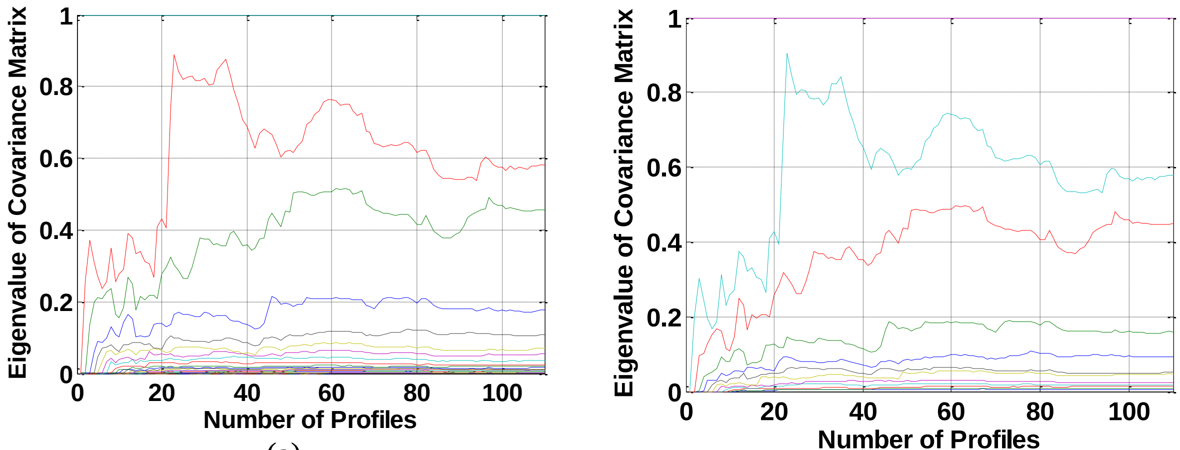

(a) (b)

Figure 43: The eigenvalue analysis of the data set as the number of water vapor profiles is increased from two to 110 for layer thicknesses of (a) 100 m and (b) 500 m. The red curve in Figure 43(a) represents the trajectory of a normalized eigenvalue as the number of profiles is increased from two to 110. Each curve represents the trajectory of a normalized eigenvalue.

A similar eigenvalue analysis was performed using 1400 water vapor profiles as a background data set for calculating the background information covariance matrix. The data set included radiosonde launches from the same location during 2008 and 2009 correspond to different weather conditions than during HUMEX11. The normalized eigenvalue analysis results are shown in Figure 44. It should be noted that the maximum value is 0.3 for a background data set size of 35 - 40. The maximum eigenvalue is substantially lower than that in Figure 44. However, the optimum data set size (the data set that contains most variability) is still similar to that in Figure 43. Increasing the number of profiles for calculating the background covariance matrix increases the accuracy of the retrieval (average profile) until the number of profiles in the background data set reaches 500.

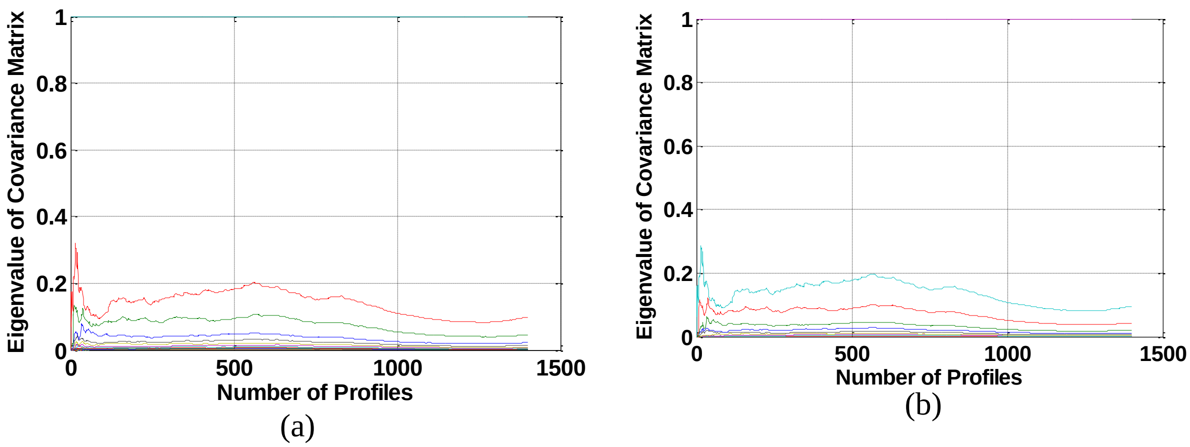

Figure 44: The eigenvalue analysis of the data set as the number of water vapor profiles is increased from two to 1400 for layer thicknesses of (a) 100 m and (b) 500 m. The red curve in Figure 43 (a) represents the trajectory of a normalized eigenvalue as the number of profiles is increased from 2 to 1400.

In this work, the eigenvalues are a measure of the variability associated with the background covariance matrix ($\bar{\bar{S}}_a$) used for the retrieval algorithm. In that case, In that case, the number of profiles used to calculate $\bar{\bar{S}}_a$ for which the eigenvalues reach a maximum has two interpretations:

- The background dataset is correlated with the atmospheric state during the measurement time, e.g., in Figure 43 profiles are close in time to the retrieval, and the peak indicates maximum variability according to the current atmosphere, which will provide a better retrieval. It is clear from the results that when a background dataset with fewer than 10 profiles is used, it does not have enough significance and the retrieval error is high, as shown in Figure 40. However, when the dataset is in the range of 40-60 profiles that have been taken close to the measurement time (as shown in Figure 40 and Figure 41), it provides information about the variability of the water vapor profile during the radiometric measurement. Therefore, the retrieval will be useful for detecting dynamic changes, as shown in Figure 40 and Figure 41.

- The background dataset is not correlated with the atmospheric state during the measurement time. In Figure 44 this maximum would be considered noise i.e., atmospheric fluctuations that are not related to the radiometric observations. In this case, the best option is to perform the retrieval when the data set has enough significance and the values of the eigenvalues are low (i.e., the size of the dataset needs to be large). Using a large dataset has the effect of averaging out the variability of the atmosphere (smoothing) as shown in Figure 42 (d) for 1000 profiles. In that case, the retrieval will tend toward a "standard atmosphere", so the retrieval algorithm will have a good performance when measuring a "standard atmosphere" i.e., the information contained in $\bar{\bar{S}}_a$. However, the retrieval will have difficulty detecting dynamic changes in water vapor because $\bar{\bar{S}}_a$ does not containthe necessary information to do so. This is where the distinction between the retrieval accuracy and the ability to detect dynamic changes is meaningful, i.e.to distinguish between these two types of effects.

Therefore, as shown in Figure 43, a background data set size of 25-35 provides maximum information about the variability of water vapor profiles. For a background data set size greater than 100 profiles, the eigenvalues of the covariance matrix are nearly constant for changes in background data set size; therefore, additional profiles provide no new information about water vapor variability. However, there is a noticeable discrepancy between the eigenvalue peak at a background data set size of 25-35 (in Figure 43), and the minimum total error obtained (from Figure 40), which occurs at a background data set size equal to 40-55. This is because a balance exists between the variability associated with the $\bar{\bar{S}}_a$ matrix and its significance. This means that the maximum information is provided by using 25-35 profiles in the background data (from Figure 43). However, this data set is not sufficiently large to provide the optimum information about water vapor variability in the atmosphere to minimize the error of the retrieval.

As already mentioned in the theoretical discussion of the background information covariance matrix in Section 3.1.3, the number of independent vectors in the covariance matrix obtained using only two profiles (Figure 42a) is similar to one, which is clear from the vertical and horizontal patterns (most the rows and columns of the matrix are scaled versions of the same vector). Therefore, all the *N* eigenvalue trajectories start at zero, which correspond to eigenvalues for background data set with 2 profiles. This is due to the fact that limited information will be obtained when calculating the covariance matrix of two consecutive atmospheric profiles since the atmosphere does not change significantly between the times at which two consecutive radiosondes are launched. As a result, the retrieval has poor performance when using a small number of background profiles. It is evident that this $\bar{\bar{S}}_a$ is not statistically significant and is not useful for retrievals but it has been analyzed for completeness of the study. On the other hand, when the number of profiles in the background data set is increased (as in Figure 42 (b) and Figure 42 (c)) the vertical and horizontal patterns disappear (although the covariance matrix has a diagonal symmetry). This improvement results from increasing the number of profiles, which takes into account more states of the atmosphere, so the values of the *N* eigenvalues values, as well as the number of linear independent vectors, increase. Increasing the number of profiles in the background data set used for computing $\bar{\bar{S}}_a$ above a certain value causes the vertical and horizontal patterns to reappear (as in Figure 42 (d)), with a consequent reduction in number of linear independent vectors (or information about water vapor variability). It can be observed that the difference between the $\bar{\bar{S}}_a$ for 40 profiles (Figure 42 (b)) and that $\bar{\bar{S}}_a$ for 1000 profiles (Figure 42 (d)), has an substantial impact on the quality of retrieval. Using the $\bar{\bar{S}}_a$ in Figure 42b results in the retrieval assigning more variability to the layers at 2-3 km altitude, while using the $\bar{\bar{S}}_a$ in Figure 42 (d) results in assigning more variability to the lower layers at 0-1 km altitude.

Therefore, there is a substantial difference between results using $\bar{\bar{S}}_a$ calculated using 40 and 1000 profiles.

From the total percentage error analysis in Figure 40 and the eigenvalue analysis of the background data covariance matrix in Figure 43 and Figure 44, it has been confirmed that the optimum size of background data set is approximately 40 and 60 for 100-m and 500-m layer thickness, respectively. However, these specific optimum sizes can change for different layer thicknesses, time, place, background statistics (a-priori profile and background error covariance) and season of retrieval.

To determine the ability to sense dynamic changes in water vapor profiles, retrievals from radiometer measurements were performed for 100-m layer thickness and background data set sizes of 40 and 1400 profiles. Results of the retrieval for August 13, 2011 are shown in Figure 45 in which they are compared with Raman lidar-retrieved profiles.

The profiles retrieved using a background data set size of 40 profiles track the inversions in the humidity profile at 500–600 m at 15:10 UTC and at 1300–1600 m at 21:10 UTC. Similarly, the slight inversion at 1400–1600 m at 20:00 UTC is also detected. However, the profiles retrieved using background data set sizes of 1400 profiles follow a trend generally similar to the Raman lidar-retrieved profiles but do not include the fine gradients and inversions in the lowest 1 km of the troposphere. These results show that the retrieval using a background data set size of approximately 40 profiles for 100-m layer thickness is optimal in this case to retrieve water vapor profiles and also to detect the gradients. However, this background dataset of 40 profiles applies to weather conditions during the HUMEX11 experiment. The optimal number of profiles might be different for other weather conditions and locations.

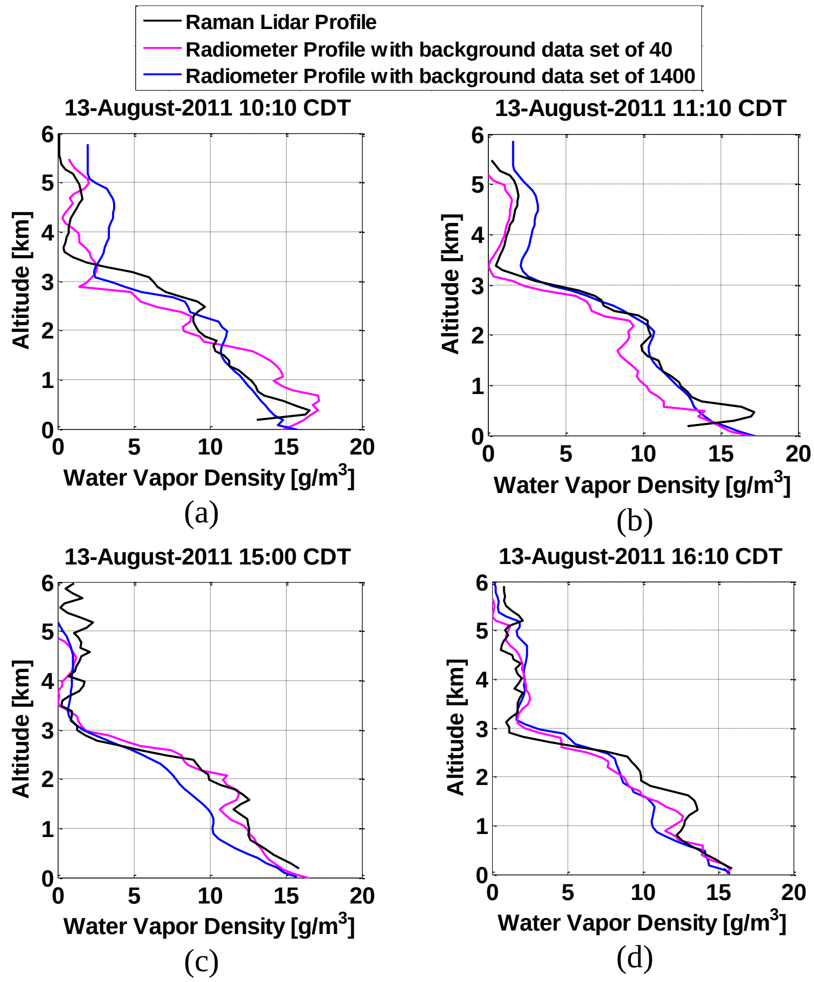

Figure 45: Time series of retrieved water vapor profiles for 100-m layer thickness and background data set sizes of 40 and 1400 in comparison with Raman lidar profiles.

5.4. Variation of Accuracy with Time between Measurement and Initialization Profile

The retrieval accuracy varies significantly with changes in the time interval between the initialization profile (from radiosondes) and the radiometer measurement. This is particularly evident for small background data set sizes (in the range of 50-100 profiles) to detect evolving changes in atmospheric water vapor profiles.

Retrievals were performed for two layer thicknesses of 100 m and 500 m for each retrieval time for a variety of background data set sizes. The retrieval errors were calculated for 100-m and 500-m layer thickness for background data set sizes of 16 and 64. The errors were computed for 40 radiometer measurements, all shown in Figure 46, as a function of time after the corresponding radiosonde launch. The total percentage error at 500 m vertical layer thickness is lower than that at 100 m layer thickness for most cases. Total errors are minimum when the radiometer measurements are close in time to the radiosonde launches. This is because the shape and values of the initialization profile are similar to the actual state of the atmosphere at the retrieval time. Total errors for 500-m and 100-m vertical layer thickness are in the range of 7 – 15% and 12 – 22%, respectively, for the time range of 0 to 150 minutes after the radiosonde launches (for background data set size of 64). Retrievals for 100-m layer thickness which are the longest in time (4-5 hours) after the radiosonde launches have errors in the range of 22 – 30%. The largest error corresponds to 100-m layer thickness and a background data set size of 16.

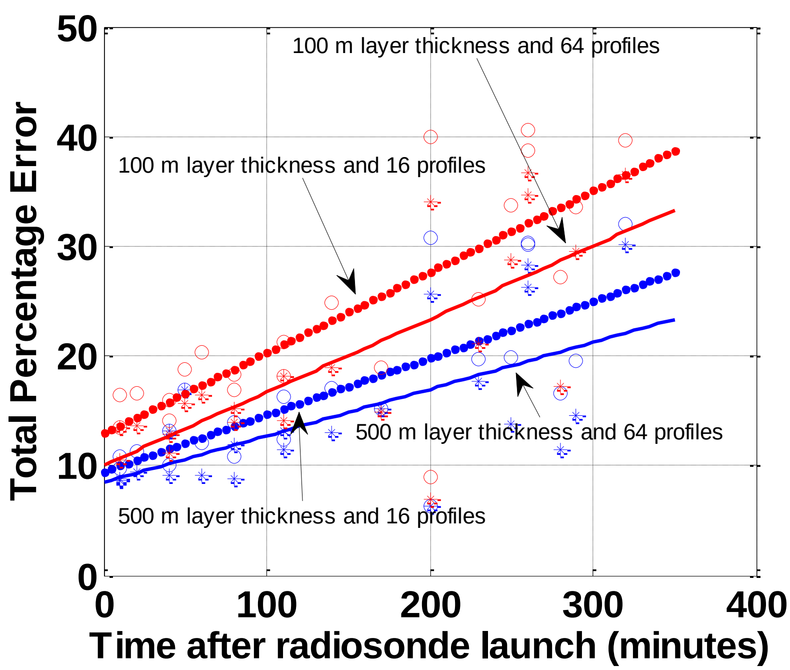

Figure 46: Total percentage error as a function of time between radiosonde launch and radiometer measurement for 100-m and 500-m layer thicknesses as well as background data set sizes of 16 and 64.

Conversely, the smallest error corresponds to the 500-m layer thickness with background data set size of 64. Therefore, as radiometer measurements are performed longer in time after the radiosonde launch, the percentage error increases. The errors are less than the errors mentioned in Table 6 when the *a-priori* data used for the retrieval was taken 150 minutes from the radiometer measurement time. Finally, the likelihood of sensing dynamic changes and gradients in the water vapor profile decreases as the elapsed time since the launch of the most recent radiosonde.

5.5. Conclusions

Water vapor profiles retrieved from radiometer measurements have confirmed that retrievals using atmospheric layers and an optimal size of background data set taken close to the measurement times have a higher likelihood of sensing evolving changes in water vapor profiles than do larger background data sets with thicker layers. Larger background data sets provide better accuracy in a statistical sense, but dynamic changes are not detected. Therefore, a large background data set is less than optimal for sensing dynamic changes in the atmosphere.

For a given atmospheric layer thickness in the range of 100 to 500 m, as the size of the background data set increases from two to 110, the total percentage error of the radiometer retrieval decreases and then increases. In between, there exists an optimum background data set size of 40 – 60 profiles to minimize the total percentage error. Sensing dynamic changes in water vapor profiles and improving retrieval accuracy are quite important while the water vapor profile is evolving. Depending on the weather conditions, the sizes of background data sets and layer thicknesses can be chosen appropriately. For days when the weather conditions are nearly constant, one can use a large background data set with thick layers, while on the days when the weather is quickly evolving, thin layers with a small background data set can be used to detect changes in the atmosphere more effectively.

Chapter VI Data Quality Analysis for Dynamics of the Madden-Julian Oscillation (DYNAMO) Experiment

The Dynamics of the Madden-Julian Oscillation (DYNAMO) field campaign [75] was conducted in the central equatorial Indian Ocean between September 1, 2011 and January 15, 2012 [76] to improve the understanding of Madden-Julian Oscillation (MJO) [77]. This chapter gives an overview of the field experiment and its goals and purpose. A list of various instruments used during the field campaign is mentioned. The radiometer data analyzed as part of this dissertation is also given in this chapter along with the data quality control.

6.1. Purpose and Goals of DYNAMO

MJO is a large-scale atmospheric phenomenon that involves coupling of atmospheric circulation with tropical deep convection. It is initiated by the development of convective clouds over the equatorial Indian Ocean [77]. These clouds propagate east resulting in drying of the atmosphere over central Indian Ocean and suppression of the cloudiness.

MJO impacts tropical cyclones, increases or decreases their activity in all ocean basins, and hence affects their prediction, particularly hurricanes near North America. It also affects the start of monsoon and intra-seasonal fluctuations of rainfall over Asia, Australia, Americas, and Africa. Even though MJO is so important, the forecast of MJO by large-scale models is usually inadequate because of improper parameterization of MJO in models. This is primarily caused due to paucity of basic and important observations in the remote equatorial Indian Ocean.

Therefore, aim of DYNAMO was to improve the quality and quantity of observations available and specifically understand the stages of development of clouds over the Indian Ocean and their associations with recharging of the humidity field in the region after the clouds propagate [77].

The DYNAMO experiment was endorsed by the World Climate Research Program and was led by Prof. Chidong Zhang of the University of Miami. The objectives of DYNAMO [75] are described as:

- performing in-situ observations of the equatorial Indian Ocean region, which are important to improve understanding of the processes affecting MJO initiation
- provide a basis for testing hypotheses which have been already developed and also forming new ones regarding these processes;
- identifying the discrepancies in current numerical models that are resulting in the low prediction skills and poor simulations of MJO initiation and also to improve modeling parameterizations.

6.2. Experiment Description and Measurements Performed

The field campaign involved performing measurements using various ground, ship and aircraft-based in-situ and remote sensing instruments. These were deployed at Diego Garcia (7.3˚S, 72.5˚E), United Kingdom and Gan Islands (0.7°S, 73.2°E), Maldives. In-situ instruments included aircraft launched dropsondes, radiosondes as well as surface-based meteorological sensors (including rain gauge). The remote sensing instruments included radars (operating at various frequencies), wind profilers and radiometers (operating at K and Ka-band). Figure 47 shows the map of the Indian Ocean region where the DYNAMO experiment was performed as well as the islands and ships which were used during the experiments. Ships involved in the DYNAMO included Mirai (Japan), Sagar Kanya (India), Baruna Jaya-III a US Geological Survey, Roger Revelle a US university national oceanographic laboratory system (UNOLS) ship. A P-3 aircraft was used for launching dropsondes. Radiosondes were launched from all ships and land facilities with daily frequencies of 4-8 hours [75].

An array of radars was deployed for the field campaign. This array included both ship- and island-based facilities. The radars collected data that was intended for estimation of vertical structures and variability of diabatic heating and moistening profiles. These profiles are very important for determining the effects of convection on large-scale circulation, to validate numerical models, and also to constrain models used to test hypotheses regarding MJO initiation processes.

Figure 47: Research vessels, aircraft and sites used during the DYNAMO experiment [75].

The array of Doppler precipitation radars provided information about cloud formation and precipitation while the information about thermodynamic processes was provided by the sounding data. Ship based instrument measured upper-ocean mixing and atmospheric boundary layer turbulence. All the measurements formed the integrated data set that is needed to determine air-sea interaction processes during MJO initiation.

As part of the DYNAMO campaign, NCAR deployed the S-PolKa (dual-wavelength S- and Ka-band) radar [78], and the University of Miami deployed a two-channel microwave radiometer (UM-Radiometer), both co-located on Gan Island. A second two-channel microwave radiometer was deployed at the US DOE's (ARM) Site on Gan Island, approximately 8.5 km southeast of the UM-Radiometer, as shown in Figure 48. Both the UM-Radiometer and the DOE radiometer have two frequency channels at 23.8 and 30.0 GHz. In addition, radiosondes were launched eight times daily (every three hours) from the DOE ARM site during DYNAMO to provide in-situ data on atmospheric conditions.

The Ka-band capability of the National Center for Atmospheric Research (NCAR) S-PolKa radar was very useful in studying non-precipitating clouds which are prevalent in the region during the time period leading to MJO initiation.

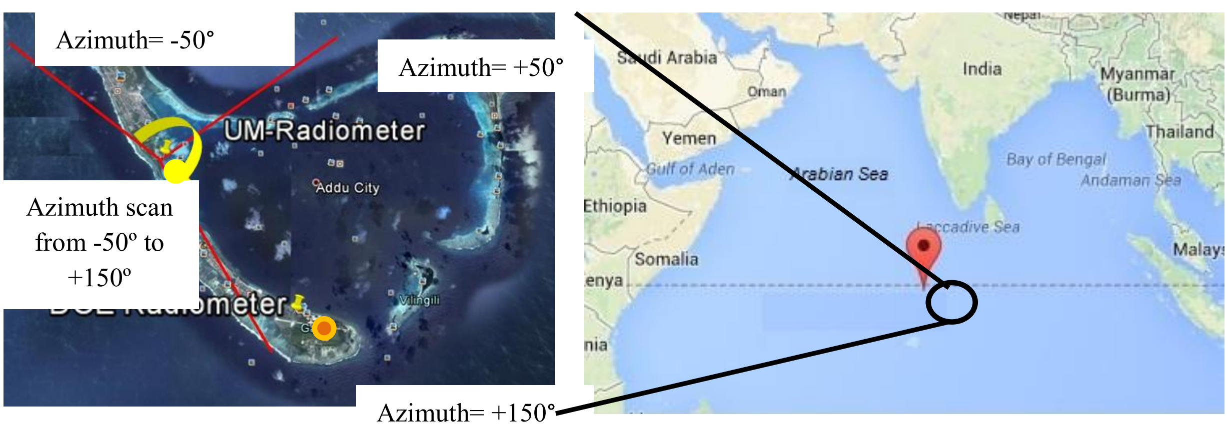

Figure 48: (Left) Locations of the University of Miami microwave radiometer (UM-Radiometer, shown by the yellow disk) and the DOE radiometer (shown by the orange disk) on Gan Island, Maldives. (Right) Zoomed out view of the equatorial Indian Ocean and Maldives.

The S-PolKa radar was deployed to monitor clouds and to measure the types and intensity of precipitation. It performed 360º azimuth scans and elevation scans of 0.5º, 1.5º, 2.5º, 3.5º, 5.0º, 7.0º, 9.0º and 11.0º known as plan position indicator (PPI) as well as vertical cross-sectional scans also known as range height indicator (RHI) scans [79]. The scanning strategy included 8 PPI elevation angles (from 0.5° to 11°) and 55 RHIs with scan angles of 0°–45°. Of the 55 RHIs, 39 were toward the north to the east and 16 were toward the ARM site. The UM-Radiometer performed measurements over a range of azimuth angles from -50º to +150º (referenced to north at 0º) and at elevation angles of 5º, 7º, 9º, 11º, 30º, 45º and 90º. Brightness temperature measurements were performed continuously to estimate slant water path (SWP) and slant liquid water (SLW) under a variety of weather conditions, including clear and cloudy skies as well as precipitation of various types and intensities.

6.3. Analysis of the Radiometer Measurements and Data Quality Control

This section analyzes the brightness temperature measurements for the time period of the DYNAMO field campaign performed by the UM-Radiometer at various elevation angles (as part of the data quality control). Measured brightness temperatures at 23.8 and 30.0 GHz and various elevation angles (5º, 7º, 9º and 11º) are analyzed for the azimuth range of -50º to +150º to determine errors, anomalies and biases. The measurements at 23.8 and 30 GHz are affected by thermodynamic state of the atmosphere where 23.8 GHz measurements are affected mostly by the variation of water vapor in azimuth and elevation angles while measurements at 30.0 GHz are mostly affected by liquid water variation. Figure 49 shows the mean and standard deviation of the measurements performed at both the frequencies. Mean value of the brightness temperatures have an associated trend with respect to the azimuth angles. For all elevation angles maximum value of the mean corresponds to azimuth angles -50º and 150º while the minimum value corresponds to 54º azimuth. The standard deviation for 23.8 GHz is in the range 10-15 K while the standard deviation for 30.0 GHz is in the range 15-30 K. These results in Figure 49 are unexpected since one would expect a uniformly distributed water vapor field in an isotropic atmosphere.

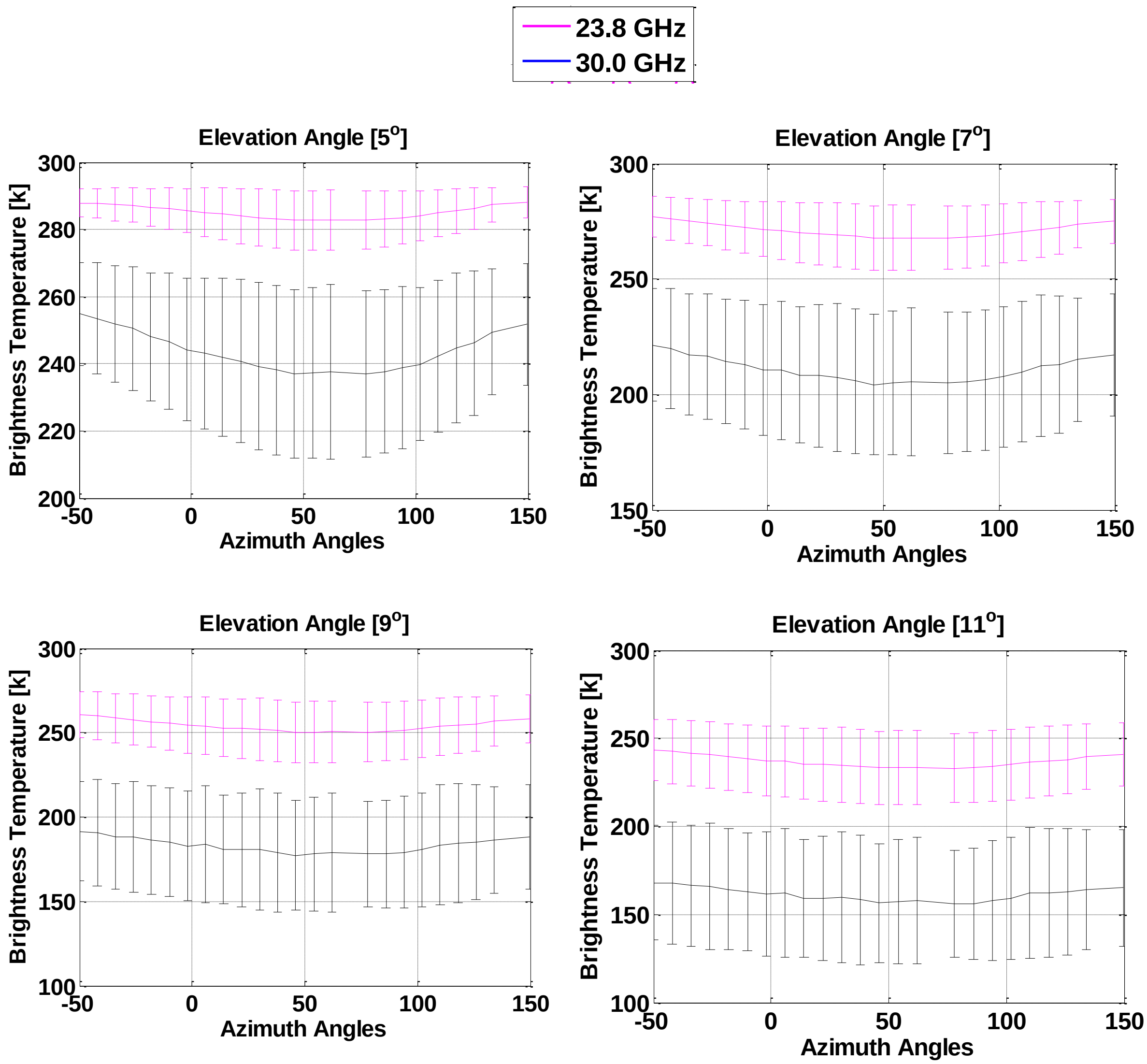

Figure 49: Mean and standard deviation of the measured brightness temperatures at 23.8 and 30.0 GHz for 5º, 7º, 9º and 11º elevation angles from 7-Oct-2011 to 15-Jan-2012.

This anisotropic behavior is analyzed in more detail in Figure 50. Here the variation in brightness temperatures for each elevation angle for 21-Oct-2012 (12:00 to 24:00 UTC) is shown. From this analysis it is confirmed that brightness temperatures measured at low elevation angles have azimuth anisotropy. The brightness temperatures corresponding to the azimuth angle

-50º and 150º are higher than azimuth angles close to 50º. The azimuth angles -35º to -10º and 120º to 140º correspond to the radiometer field of view above ground while the azimuth angle range 0º to 120º corresponds to field of view above water.

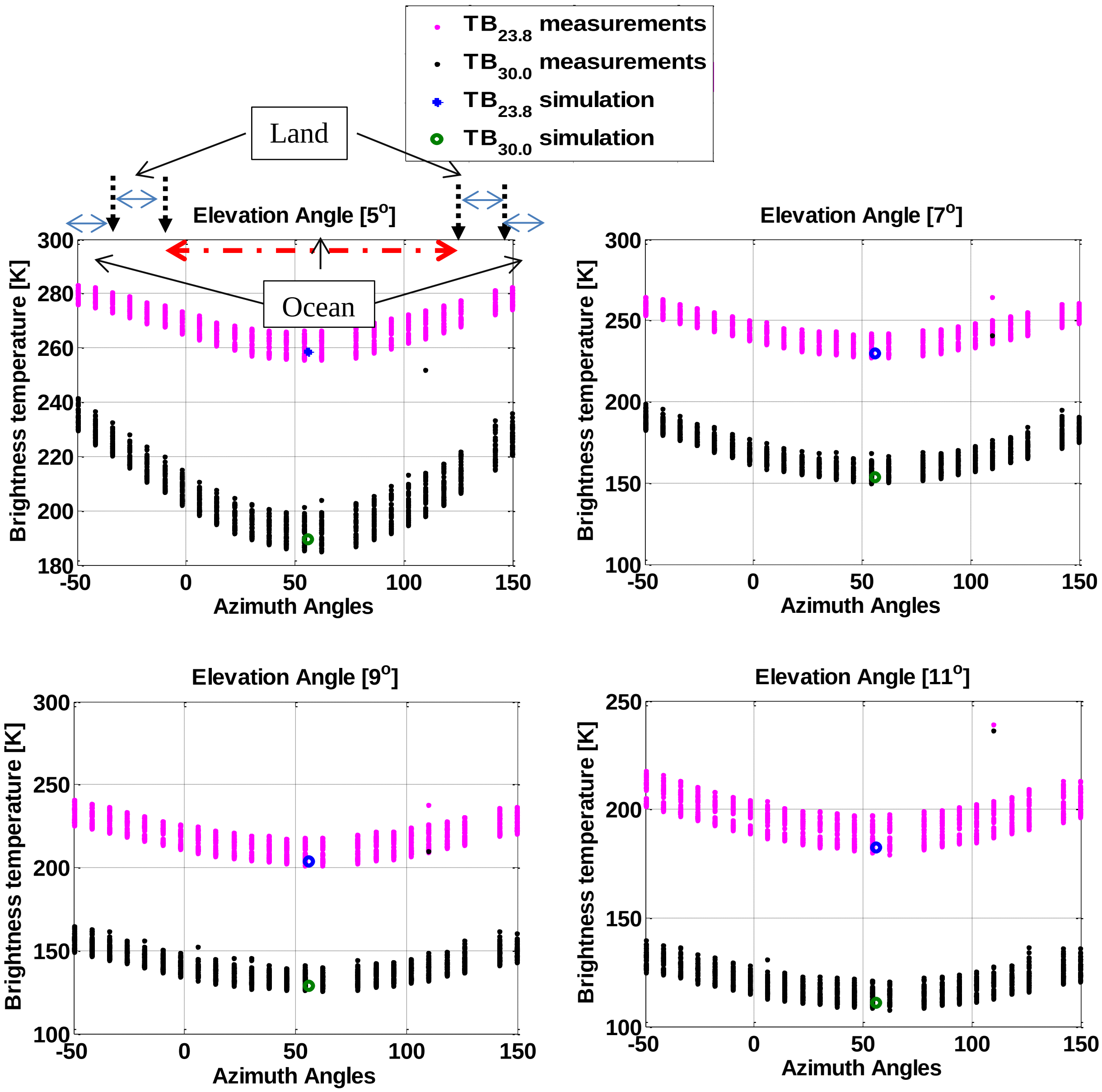

Figure 50: Measurements associated with the azimuth scanning pattern, for 5º, 7º, 9º and 11º elevations for October 21 from 12:00 to 24:00 UTC are compared with brightness temperatures simulated using radiosonde data taken at 14:30 UTC.

For the set of measurements at 23.8 GHz, the difference between the highest (azimuth -50º or 150º) and lowest (azimuth 54º) value of brightness temperatures corresponding to each elevation angle is approximately constant at 20 K as shown in Figure 50. However, the difference between the highest and lowest value of brightness temperatures at 30.0 GHz reduces as the elevation angle increases. The vertical fluctuation in the plots is due to the changes in the atmosphere over the period of 12 hours of measurements and system noise.

This anisotropic behavior of the brightness temperatures with respect to the azimuth angles is analyzed in more detail in the next chapter. Various studies have been performed to determine the source (wind direction, wind speed, land contamination of the antenna brightness temperatures and water vapor at ground level) of this azimuth anisotropy in Chapter VII.

6.4. Conclusions

Data set collected during DYNAMO offers an unique opportunity to explore new techniques of retrieving SWP and SLW at low elevation angles because most of the integrated water vapor and liquid water retrieval algorithms have been developed for zenith pointing radiometer measurements. The new retrieval algorithm and the results have been discussed in Chapter VIII. The UM-Radiometer was collocated with the NCAR's SPolKa radar, and both the instruments were measuring common volume of the atmosphere. The estimated SWP and SLW can be validated by comparison with those retrieved using radar measurements. Another challenge would be to determine the source of the anisotropy observed at the low elevation angles in Figure 49 and Figure 50.

Chapter VII DYNAMO Data Quality Control: Source Analysis of Brightness Temperature Anisotropy

During the Dynamics of the Madden-Julian Oscillation (DYNAMO) [75] campaign a microwave radiometer operating at 23.8 and 30.0 GHz was deployed by the University of Miami (UM) to estimate slant water path and slant liquid water at the Gan Island, Maldives as explained in Chapter VI. While performing the data quality control for measured brightness temperatures during clear sky conditions, anisotropy was observed for the elevation angles 5°, 7°, 9° and 11° at various azimuth angles. The anisotropy here to will be referred to as azimuth anisotropy.

Main goal of this chapter is to analyze the anisotropic behavior of measured brightness temperatures along with various atmospheric parameters like wind direction, water vapor density and wind speed to determine the physical source of this anisotropy. Radio frequency interference (RFI), land contamination and mechanical tilt of the radiometer at all the azimuth angles were also analyzed as possible sources of the anisotropy.

7.1. Brightness Temperature Measurements and Azimuth Anisotropy

An extended analysis has been performed to determine the source of azimuth anisotropy which has been observed in Section 6.3. As part of the analysis brightness temperatures measured on two different days are shown in Figure 51 (a) and (b). Time series of measurements performed on January 7, 2012 are shown in Figure 51 (a). It was a dry day and the crests correspond to end of a scan at 150° and start of a new scan at -50°. The minimum value of measured brightness temperatures is at the azimuth angle of 54° and the observed anisotropy is a persistent phenomenon. However, for some days it is not evident at all.

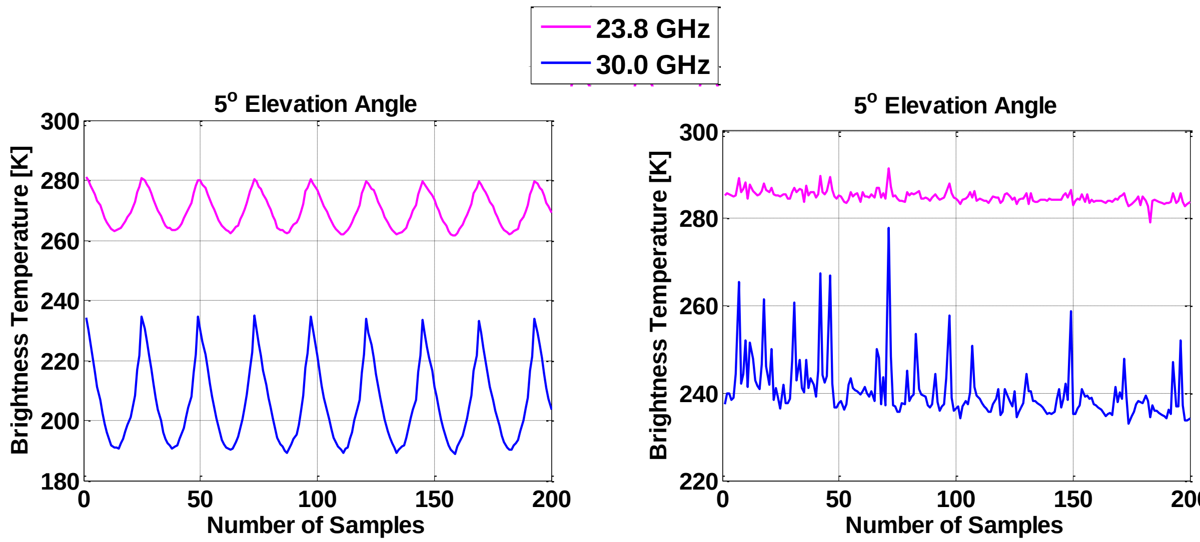

(a) (b)

Figure 51: The time series of brightness temperatures at 23.8 GHz for elevation angle of 5° (a) taken on 7-Jan-2012 and (b) taken on 9-Oct-2011 where x-axis is the time period noon to 14:30 UTC.

This is determined by analyzing the time series of measurements performed on 9-Oct-2011 shown in Figure 51 (b). The measurements do not follow any trend and the brightness temperatures at 23.8 GHz have small variations while measurements at 30.0 GHz vary over time and have a dynamic range of approximately 30 K. Based on the radar measurements and weather prediction for 9-Oct-2011, it was confirmed that the atmosphere around the radiometer had liquid water due to rain and cloud.

7.2. Possible Sources of Azimuth Anisotropy

Various sources of azimuth anisotropy such as atmospheric parameters at ground level i.e., water vapor, wind direction, wind speed and liquid water have been analyzed here. Land contamination, RFI and variation in elevation angles of the radiometer due to the slight movement of the base of the radiometer have also been analyzed as possible sources. For the analysis, a new term anisotropy amplitude has been defined as the difference between brightness temperature measured at azimuth angles of -50° and 54° for each elevation angle.

7.2.1 Study of Atmospheric Parameters to Identify the Source of Anisotropy

The measured brightness temperatures at various azimuth angles indicate that there is possibility of an uneven distribution of water and liquid water in the atmosphere. The relation between anisotropy amplitude and water vapor density, liquid water, wind speed and wind direction at ground level is analyzed. This was done to determine the magnitude of impact of wind on the movement of water vapor and liquid water over the Gan Island.

7.2.1.1 Relationship between Anisotropy and Wind Direction

In this analysis wind direction measurements performed by radiosondes at various altitudes are analyzed for the time period of October 2011 to January 2012 and are shown in Figure 52.

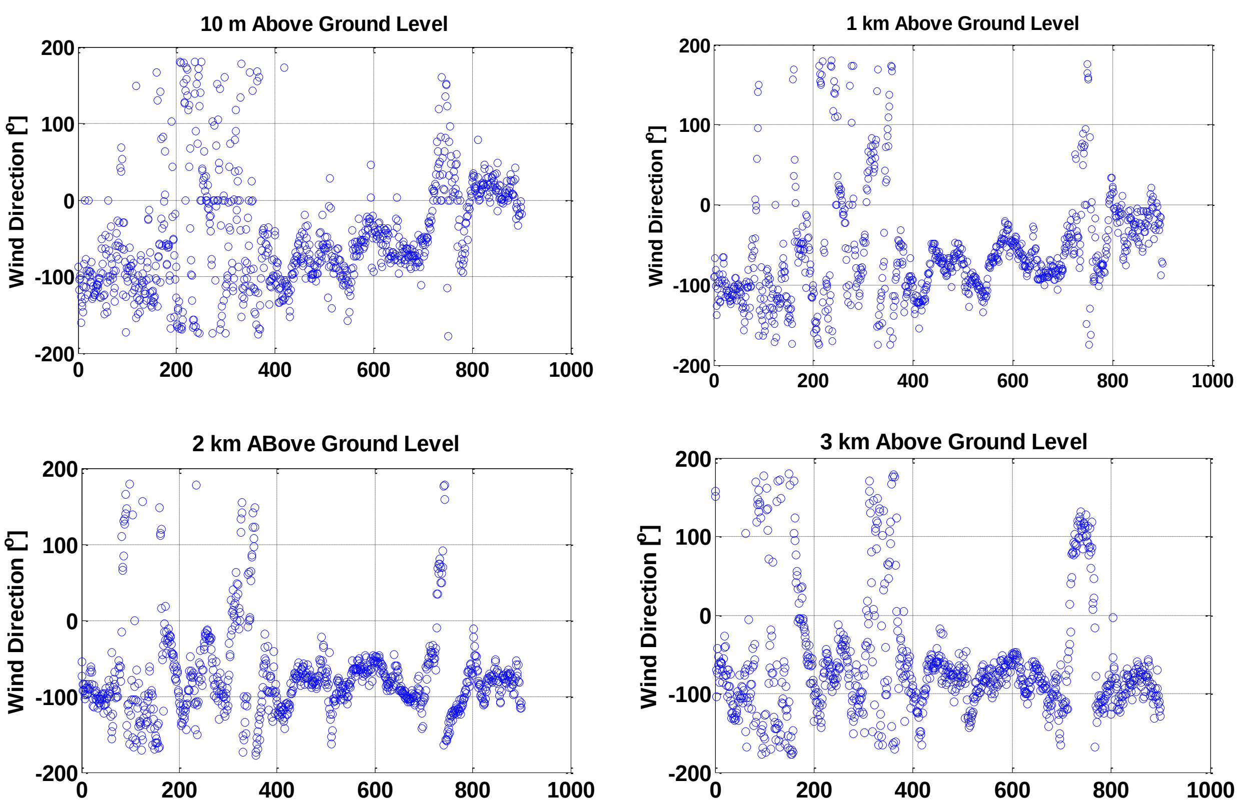

Figure 52: Wind direction measurements performed by radiosondes at approximately 10 m, 1 km, 2 km and 3 km above ground level for the time period October-2011 to January-2012.

Results show that the wind direction values 10 m above ground level are persistently between -180° to 50° for the samples 380 to 900 (corresponding to the time period between 20-

Nov-2011 to 15-Jan-2012) while most of the wind direction values taken at 1, 2 and 3 km above ground level are persistently in the range -180° to 0° as shown in Figure 52. Wind direction samples (380 to 900) at 10 m above ground level have been analyzed along with anisotropy amplitude for elevation angles of 5°, 7°, 9° and 11° which is shown in Figure 53.

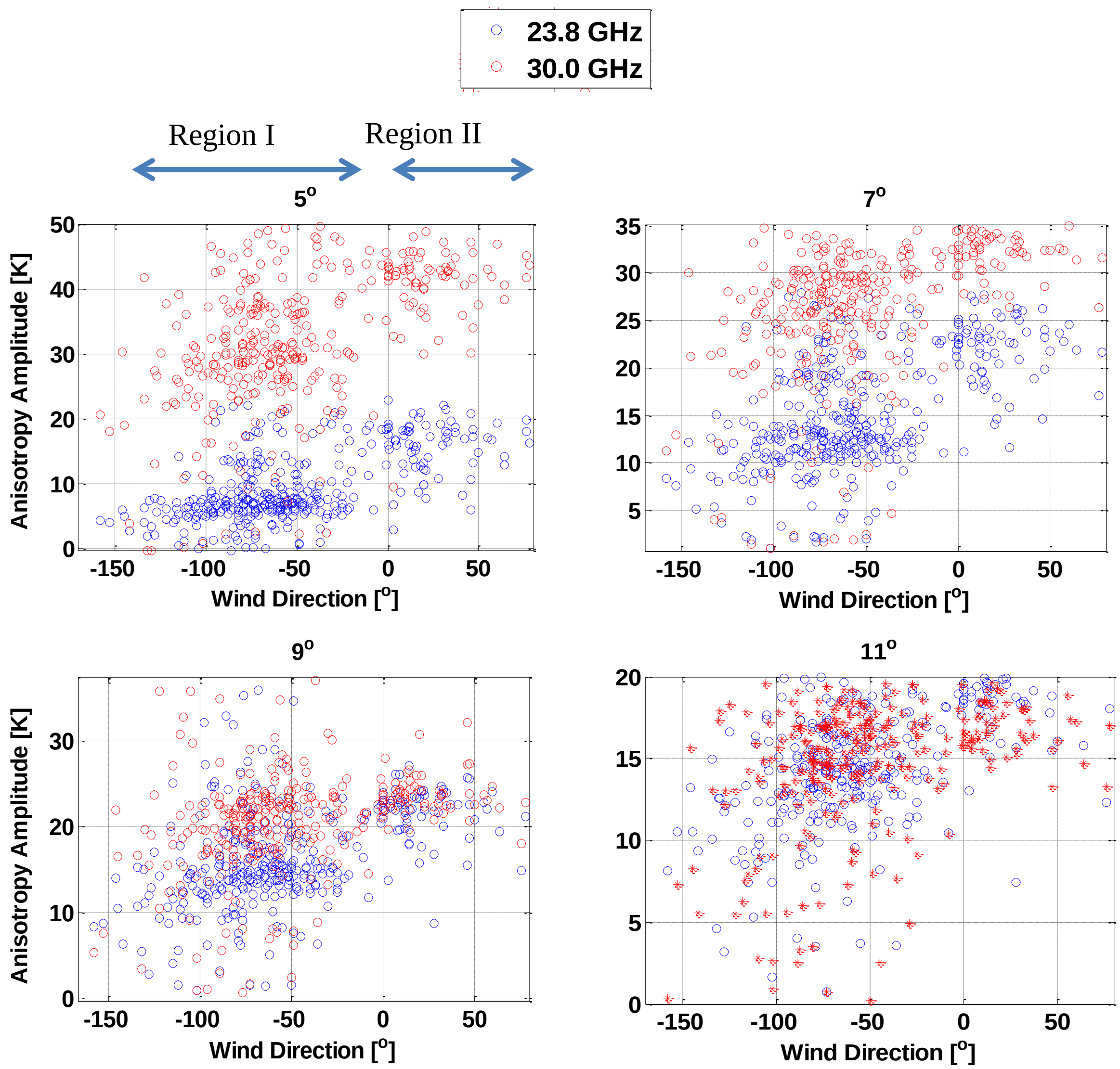

Figure 53: Scatter plot of wind-direction and anisotropy amplitude for each elevation angle and for both frequencies (for time period of 20-Nov-2011 to 15-Jan-2012).

From the figure, two regions can be observed in the scatter plot i.e., wind directions for range -150° to -20° and 0° to 50°. There is a non-linear correlation between anisotropy amplitude and wind direction. This is because all wind direction samples in the range of 380 to 900 are not in the range of -180° to 50°. Figure 53 shows that anisotropy amplitude for 23.8 and 30.0 GHz at 5° elevation angle differ by 20 K while that of 7° and 9° differ by 15 and 5 K, respectively. For 11° elevation angle, the anisotropy amplitude values for both the frequencies are overlapping. Next, the anisotropy amplitudes are binned (bin width of 10°) based on their corresponding wind direction at 10 m above ground level as shown in Figure 54. Binned data for the 4 elevation angles show that there is a non-linear correlation between wind direction and anisotropy amplitude. The same analysis was also performed for difference between the brightness temperatures taken at azimuth angles of 54° and 150° corresponding to elevation angles 5°, 7°, 9° and 11° for the time period of 20-Nov-2011 to 15-Jan-2012. Again a non-linear relationship was found and the results are similar to those in Figure 53 and Figure 54. Therefore, wind direction is one of the possible sources of azimuth anisotropy.

A statistical significance test is used to determine the probability that the observed relationship between the anisotropy amplitude and atmospheric parameter of study (i.e., wind direction) is not due to chance. The test determines if the outcome of this study can lead to a rejection of the hypothesis (null hypothesis) that there is no relationship between two measured parameters based on a pre-specified low probability threshold called P-values. Lower the P-value, higher the probability that the observed relationship between two parameters is not by chance. Null hypothesis rejection threshold is usually set at P-value less than 5-8% (here it is set at 8%). P-values for the correlation between anisotropy amplitude and wind direction at various altitudes are calculated and shown in Figure 55. P-values are lower than the threshold value for altitudes less than 1 km, for elevation angles considered here. Therefore, wind direction in the lowest 1 km of troposphere is correlated to the anisotropy.

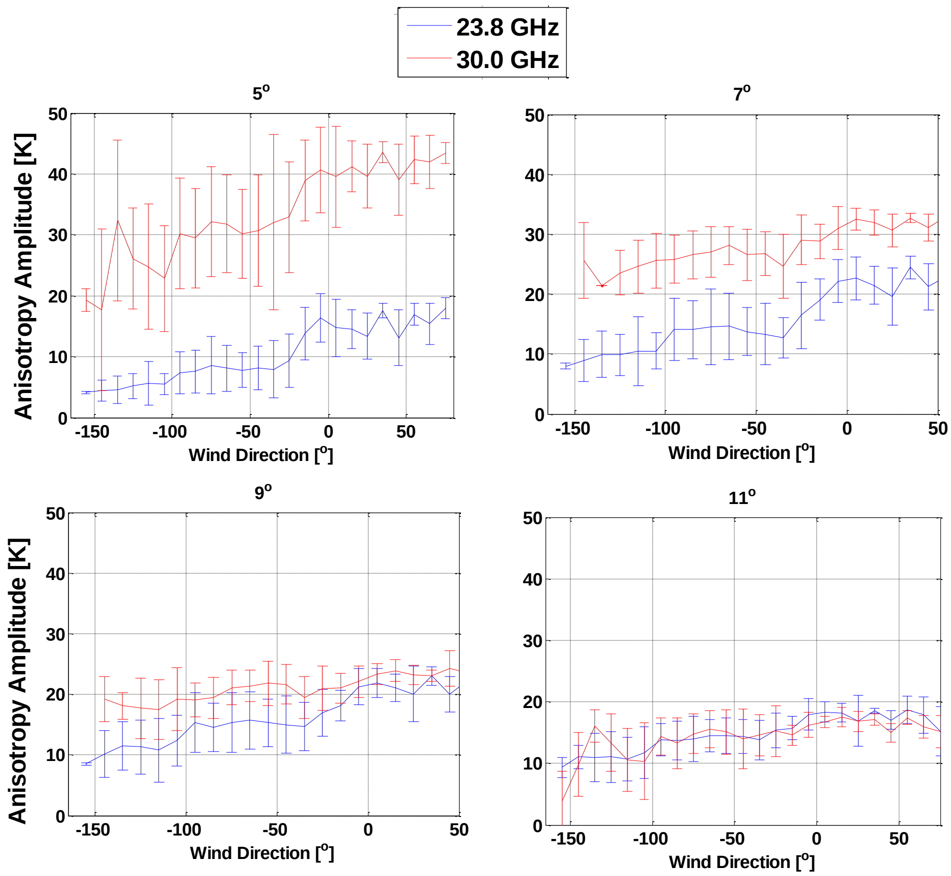

Figure 54: Scatter plot for anisotropy amplitude for corresponding wind-direction for each elevation angle and for both frequencies for time period of 20-Nov-2011 to 15-Jan-2012

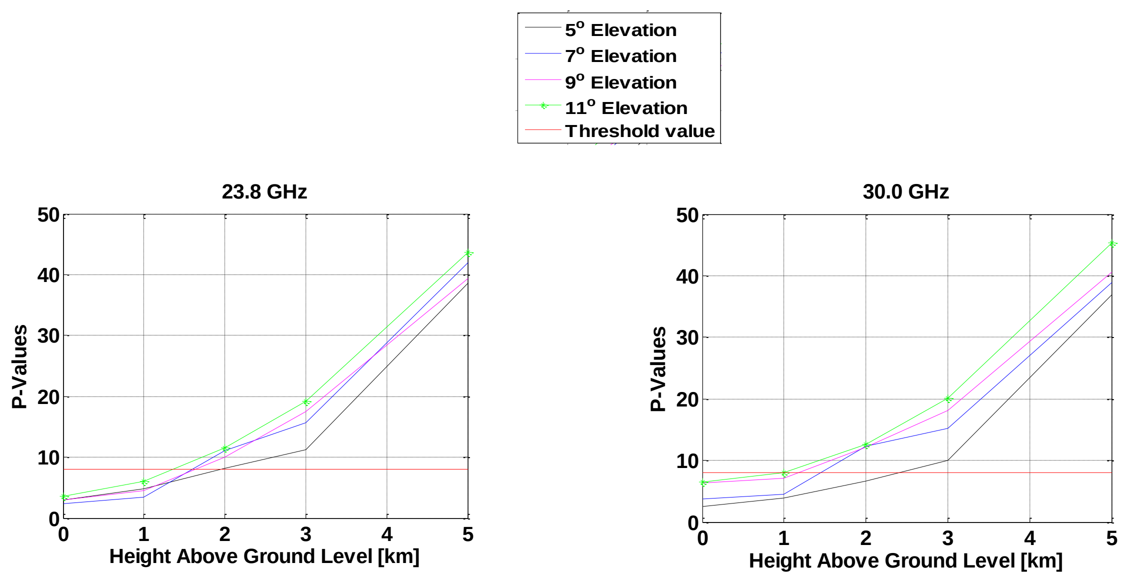

Figure 55: P-values for the correlation between anisotropy amplitude and wind direction at various altitudes for 23.8 and 30.0 GHz.

7.2.1.2 Relationship between Anisotropy and Wind Speed

The wind speed measurements have been analyzed to determine their contribution to azimuth anisotropy. Wind speed at 10 m, 1, 2 and 3 km above ground level are shown in Figure 56 and the values are in the range of 0 to 5 m/s at 10 m above ground level while they are in the range of 15 to 25 m/s for altitudes 1-3 km above ground level.

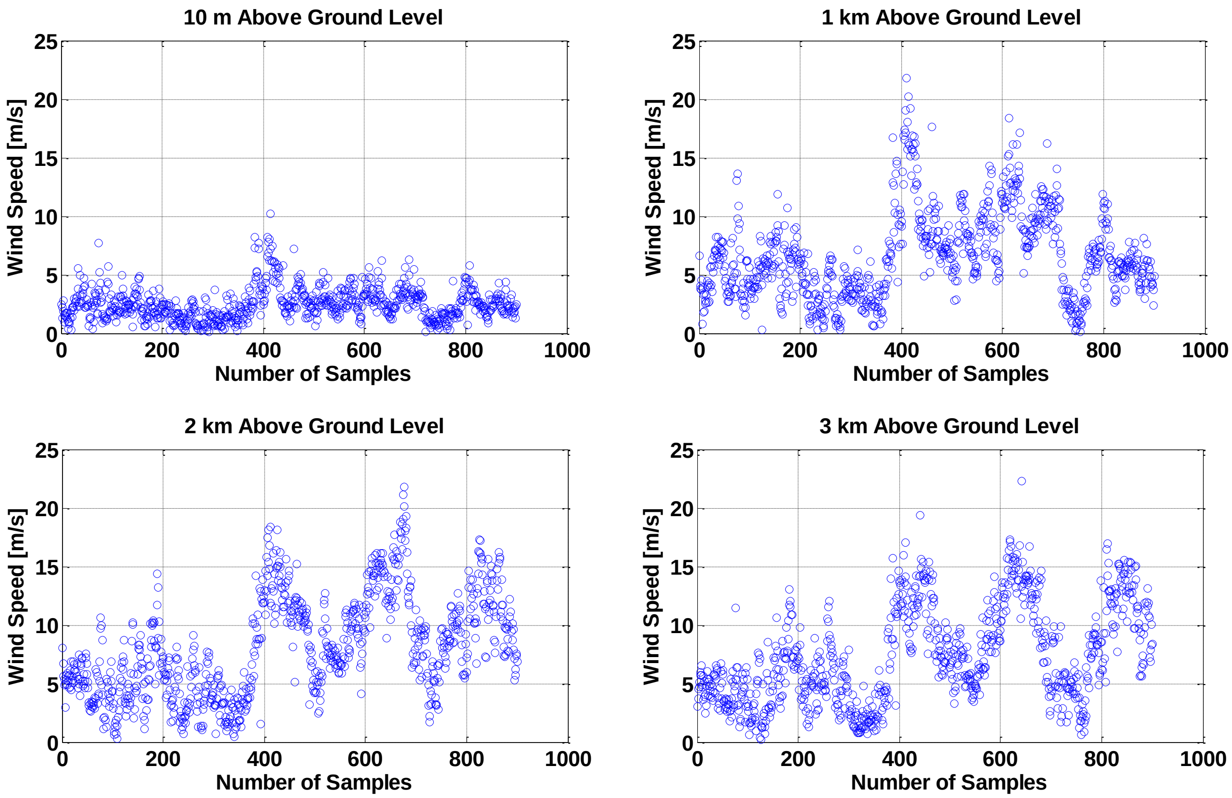

Figure 56: Wind speed taken by radiosondes at approximately 10 m above ground level for the time period October-2011 to January-2012.

In this analysis the binned anisotropy amplitudes are presented along with wind speed at 10 m above ground level as shown in Figure 57. Anisotropy amplitudes for the four elevation angles and two frequencies do not show any trend and are spread out with respect to the wind speed. However, the anisotropy amplitudes corresponding to 5° and 7° elevation angles as well as wind speed range of 5 to 6 m/s increase by 5 to 10 K.

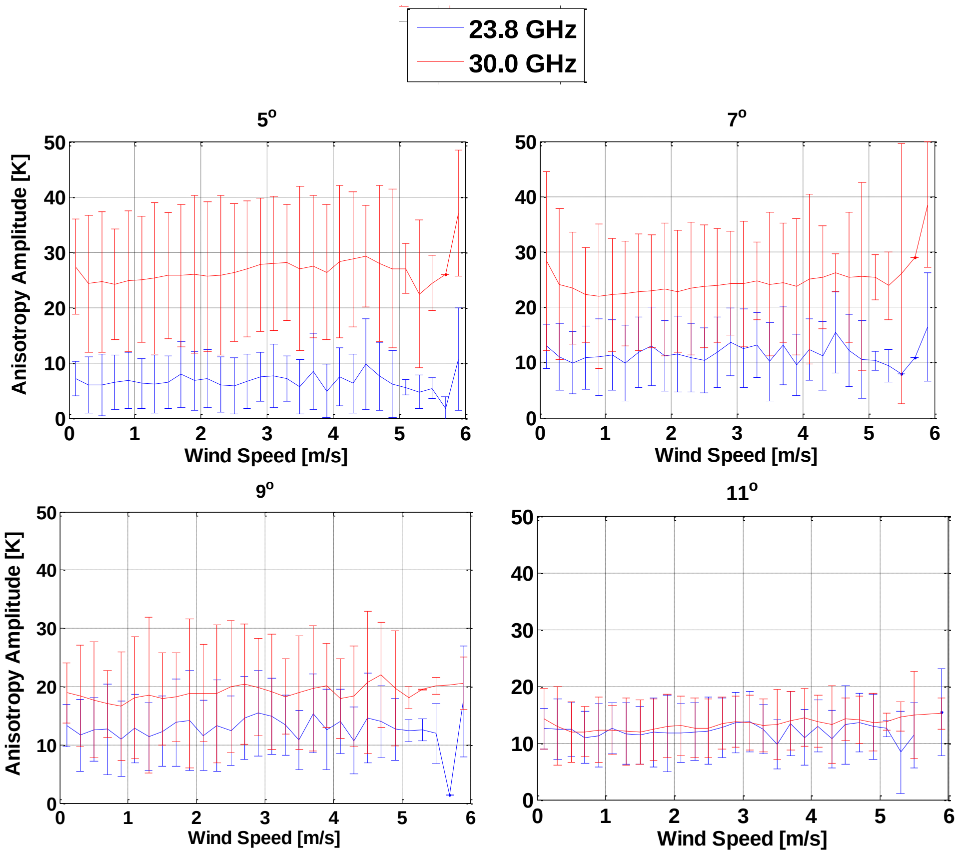

Figure 57: Scatter plot for binned anisotropy amplitude for corresponding wind speed for each elevation angle and for both frequencies for time period of 7-Oct-2011 to 15-Jan-2012

This is because of the samples correspond to wind direction of -50° to 0°. Based on this analysis it is clear that wind speed is not a contributor to anisotropic behavior of measurements. This is particularly confirmed by the statistical significance test where the P-values calculated for the correlation between anisotropy amplitude and wind speed at various altitudes are shown in Figure 58. The P-values are higher than 30% for all the altitude under consideration. So, there is no correlation between wind speed at various altitudes and the anisotropy amplitude. Wind speed is not a source of the azimuth anisotropy.

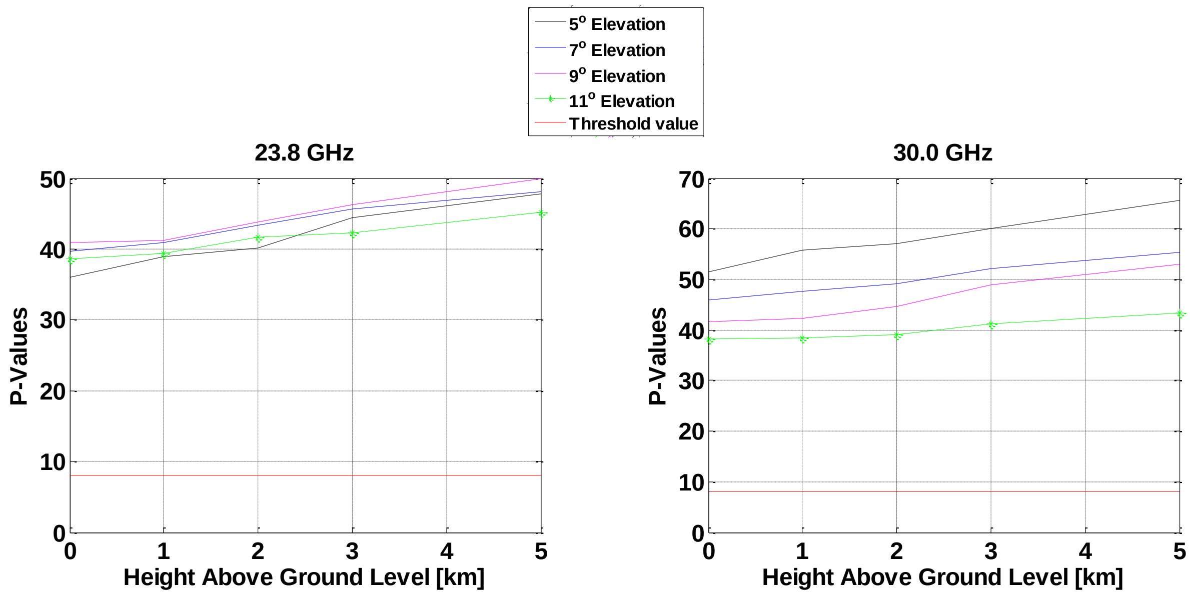

Figure 58: P-values for the correlation between anisotropy amplitude and wind speed at various altitudes for 23.8 and 30.0 GHz.

7.2.1.3 Relationship between Anisotropy and Water Vapor Density

Next water vapor density measurements at 10 m above ground level during October 2011 to January 2012 are used for the study. Water vapor density samples from 1 to 900 are shown along with azimuth anisotropy (between azimuth angles of -50° and 54°) in Figure 59. There is a decreasing trend in the azimuth anisotropy with the increase in water vapor density values. This means that the increase in water vapor density results in increase in brightness temperatures at the azimuth angles of study thus reducing the difference between the measurements i.e., higher the water vapor density lower the anisotropy amplitude.

Calculation of P-value for the correlation between anisotropy amplitude and water vapor density at various altitudes are shown in Figure 60. The P-values are lower than 8% for water vapor density in the altitude range 0 to 800 m. Thus the variation in the water vapor density in the lowest 1 km of the troposphere has an impact on the anisotropy amplitude.

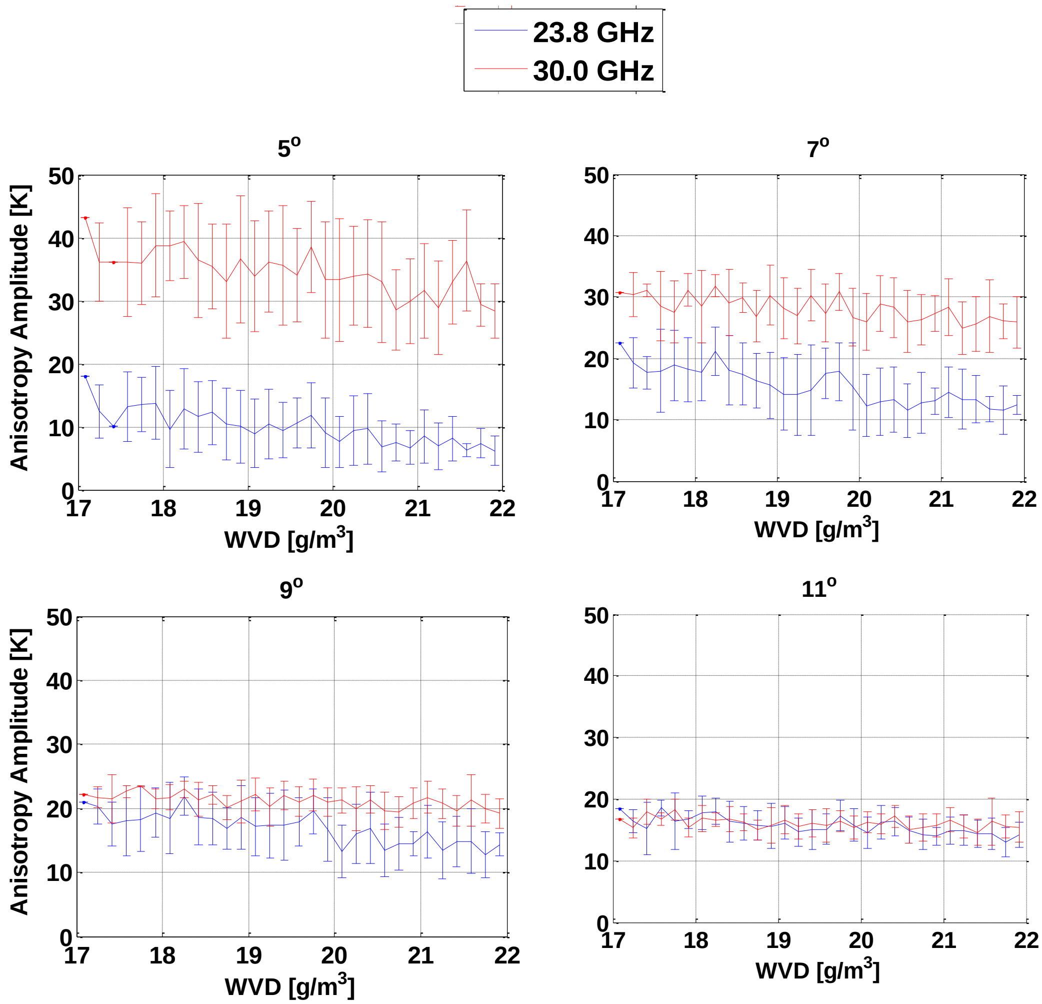

Figure 59: Scatter plot for binned anisotropy amplitude for corresponding water vapor density for each elevation angle and for both frequencies for time period of 7-Oct-2011 to 15-Jan-2012

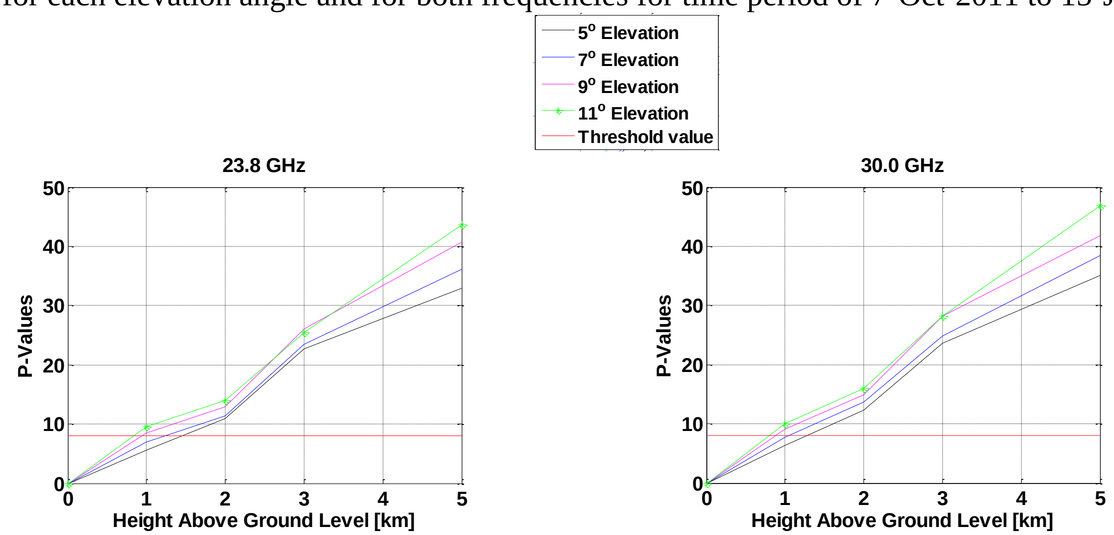

Figure 60: P-values for the correlation between anisotropy amplitude and water vapor density at various altitudes for 23.8 and 30.0 GHz.

7.2.1.4 Relationship between Anisotropy and Liquid Water

Another analysis was performed using liquid water density at 50 m above ground level calculated using radiosondes measurements. The liquid water density samples (1-900) along with azimuth anisotropy are shown in Figure 61. There is a decreasing trend in the azimuth anisotropy with the increase in the liquid water for elevation angles 5° and 7°. This is supported by the results shown in Figure 51 (b) where increase in the liquid water present in the atmosphere results in increase in brightness temperatures at all the azimuth angles of study thus reducing the anisotropy amplitude i.e., higher the liquid water density lower the phenomenon.

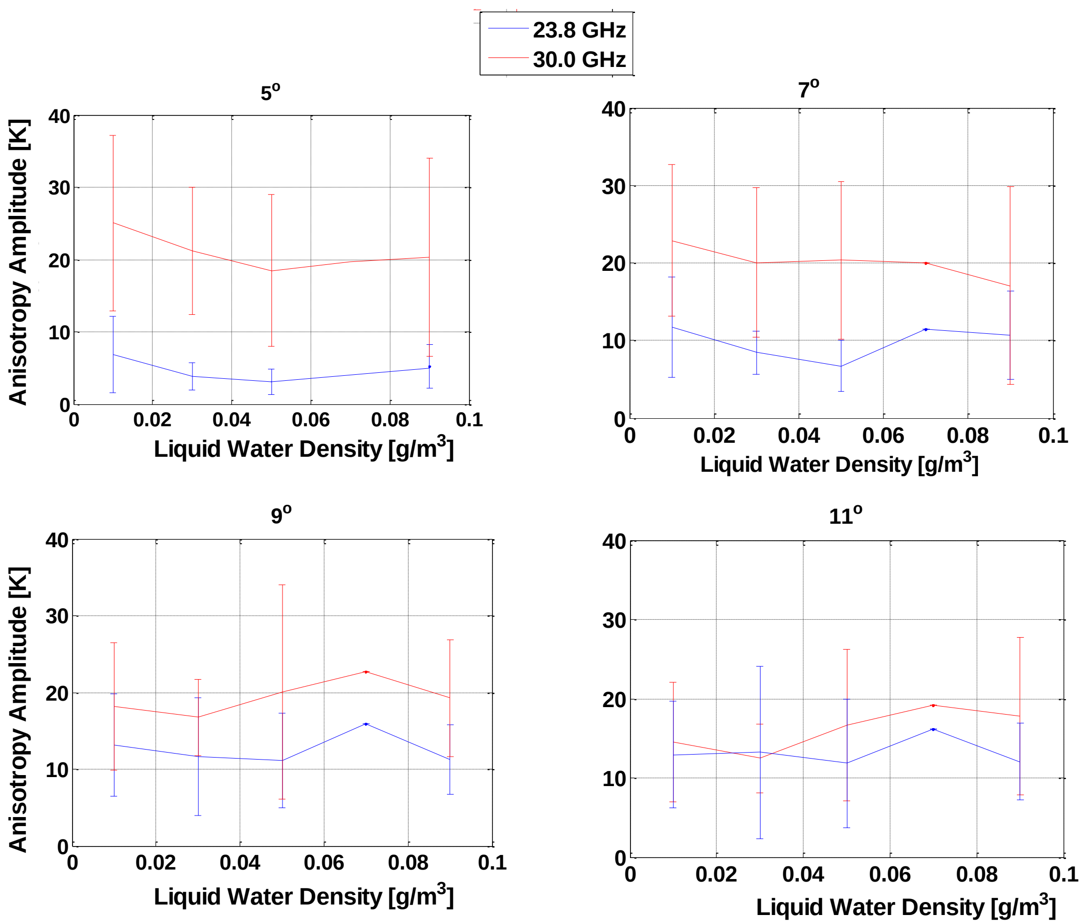

Figure 61: Scatter plot for binned brightness temperature difference for corresponding liquid water density for each elevation angle and for both frequencies for time period of 7-Oct-2011 to 15-Jan-2012 (Brightness temperature difference for azimuth angles -50° and 54°)

P-values calculation for the correlation between anisotropy amplitude and liquid water density at various altitudes are shown in Figure 62. The P-values are higher than 8% for most of the altitudes considered in this case. Thus the liquid water in the lowest 1 km of troposphere does not have an important effect on the anisotropy amplitude.

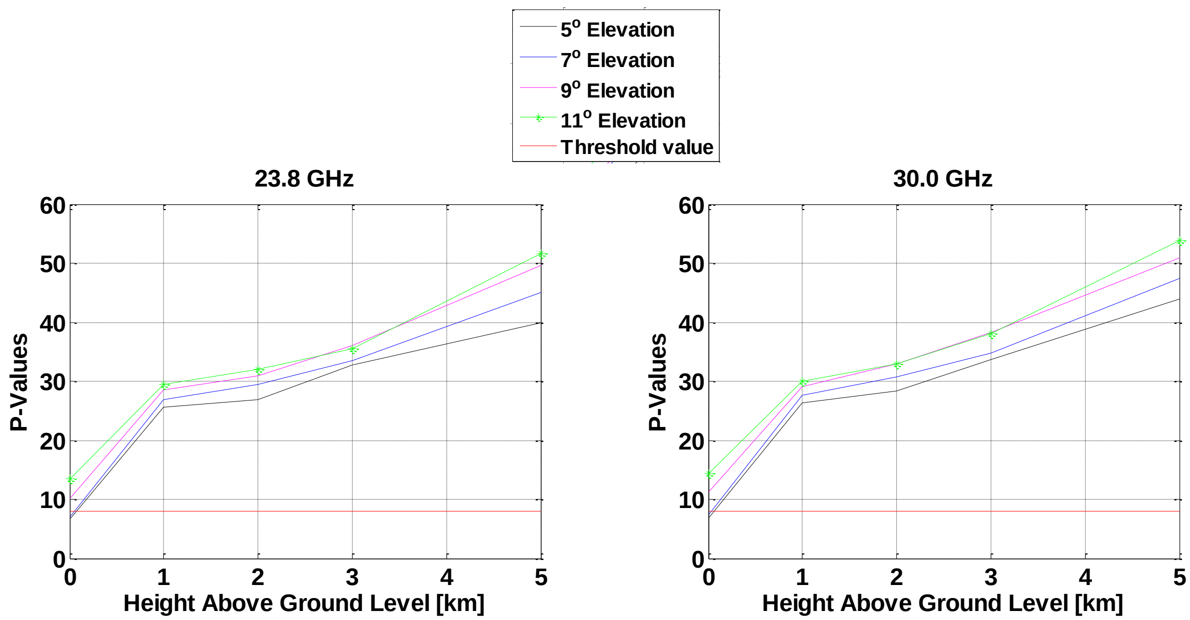

Figure 62: P-values for the correlation between anisotropy amplitude and liquid water at various altitudes for 23.8 and 30.0 GHz.

7.2.1.5 Summary of Azimuth Anisotropy on Atmospheric Parameters

The P-values for relation between azimuth anisotropy and wind direction, wind speed, water vapor and liquid water in the lowest 100 m of the troposphere is summarized in Tables 7 and 8.

Table 7. P-values for determining statistical significance for 23.8 GHz for brightness temperature difference between azimuth angles of -50° and 54°

Elevation Angle	**5°**	**7°**	**9°**	**11°**
Water Vapor	0%	0%	0%	0%
Wind Direction	3.01%	2.31%	2.97%	3.62%
Wind Speed	36.03%	39.70%	40.85%	38.67%
Liquid Water	6.61%	7.12%	10.13%	13.57%

Table 8. P-values for determining statistical significance for 30.0 GHz for brightness temperature difference between azimuth angles of -50° and 54°

Elevation Angles	**5°**	**7°**	**9°**	**11°**
Water Vapor	0%	0%	0%	0%
Wind Direction	2.53%	3.82%	6.39%	6.46%
Wind Speed	51.48%	45.98%	41.63%	38.24%
Liquid Water	6.97%	7.51%	11.29%	14.38%

This correlation between wind direction, water vapor and anisotropy amplitude can be explained to certain extent by the atoll effect [80]. However, the anisotropy amplitude of 20 K or more is significant and can be due to about 20-40% variation in water vapor along the azimuth angles which is a lot in terms of atmospheric variability for water vapor in a distance of about 5-10 km at the same time. Therefore, various possible sources of anisotropy have been explored.

7.2.2 Hypothesis of Land Contamination, RFI and Mechanical Tilt Affecting Measured Brightness Temperatures

7.2.2.1 Hypothesis of Land Contamination

Analysis here involves the verification of hypothesis of land contamination being a possible source of the observed anisotropy because brightness temperatures increase as the field of view of the radiometer gets close to land during azimuth scan. There is a possibility of contributions from land contaminating the antenna side lobes because the lowest elevation angle of measurement is 5° and the antenna half power beamwidth is 3° [73], However, the fact that maximum value of brightness temperatures is measured at an azimuth angle which corresponds to field of view above water is (azimuth of -50° and 150°) contradicts the hypothesis of land contamination and needs more analysis.

In case of land contamination, the contribution from antenna side lobes and consequently measurement will vary with the land temperature. As part of the study, the time series of difference between 4 pm and 4 am land temperature is analyzed for the whole time period of the experiment as shown in Figure 63 (a). The temperature has been measured by in-situ sensor at two meters above ground level. The 4 pm surface temperature is constantly higher than that at 4 am by approximately 4 to 6 °C for the whole time period in most of the cases.

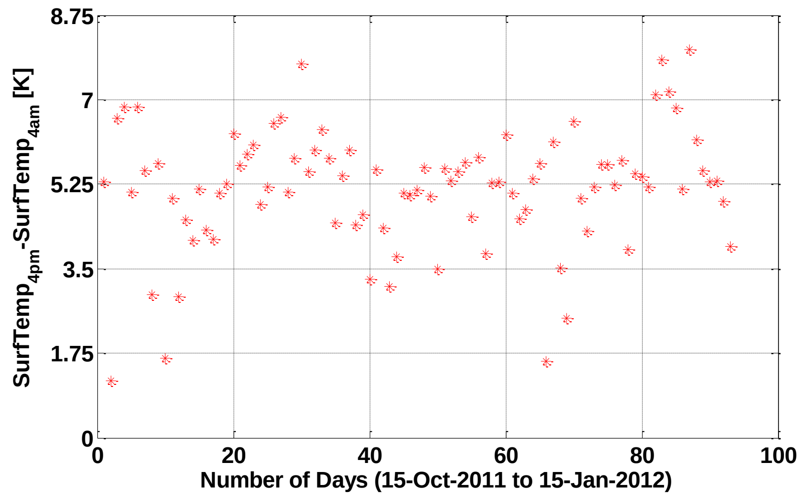

(a)

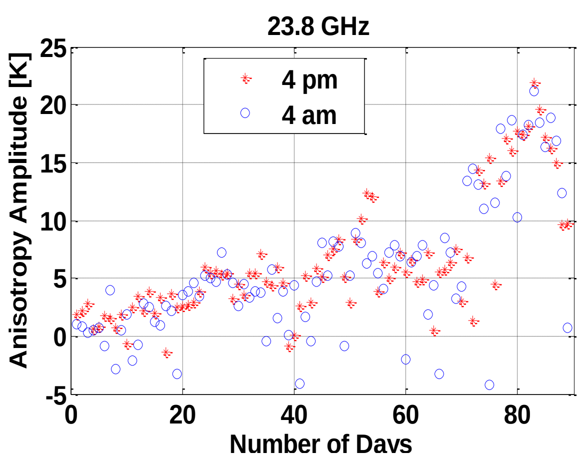

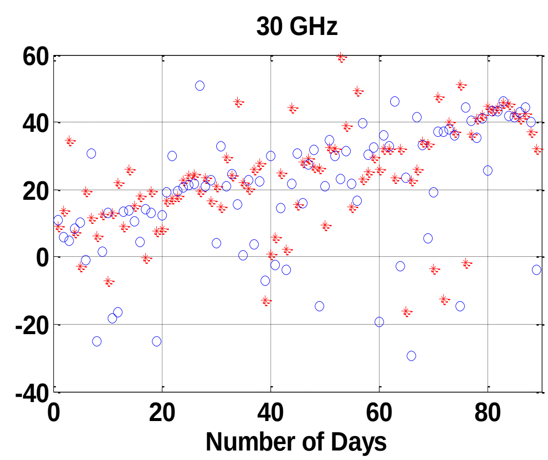

(b) (c)

Figure 63: (a) Difference in surface temperature between 4 pm and 4 am over 3 months. The difference of brightness temperature taken at azimuth angles -50° (high brightness temperatures) and 54° (low brightness temperatures) for 5° elevation angles (b) at 23.8 GHz (c) at 30.0 GHz at 4 pm and 4 am for 3 months.

The skin depth of soil is approximately 3 cm at the microwave frequencies of 23.8 and 30.0 GHz, so land temperature can be assumed to be similar to atmospheric temperature at two meters above the ground. The impact of higher day time temperature on brightness temperature measurements should be obvious in case of land contaminating the measurements. Therefore, anisotropy amplitude is computed for 5° elevation angles from 7-Oct-2011 to 15-Jan-2012 at 4 pm and at 4 am. The time series of anisotropy amplitude for 23.8 GHz is shown in Figure 63 (b) while that for 30.0 GHz is shown in Figure 63 (c). Anisotropy amplitude for both 4 am and 4 pm show a similar increasing trend and pattern for the three months of the experiment. It increases from 5 K to 20 K during the field experiment for 23.8 GHz while it increases from 15 to 50 K for 30.0 GHz for the same period of time. Azimuth anisotropy dynamic range for 30 GHz is approximately 4-5 times higher than at 23.8 GHz. The time series of azimuth anisotropy for day and night as shown in Figure 63 (b) and (c) is not explained by the times series of difference in land temperature (for day and night) in Figure 63 (a).

Based on these results and assumed antenna main beam efficiency an analysis has been performed to verify the contribution from land. Assuming a typical antenna main beam efficiency of 90% for the UM radiometer, the brightness temperature T_B has contributions from various sources based on Eqn. (VII.1)

$$T_B = 0.9T_{atm\_elevation} + 0.05T_{atm\_nonelevation} + 0.05T_{ground} \qquad \text{(VII.1)}$$

where:

- $T_{atm\_elevation}$ is the contribution to total brightness temperature from atmosphere at an elevation angle and is due to the main beam,
- $T_{atm\_nonelevation}$ is the contribution to total brightness temperature from sources other than atmosphere and land due to the side lobe pointing away from land,
- T_{ground} is the contribution to total brightness temperature from land due to the side lobe pointing towards land.

Assuming the worst case scenario where the emissivity is one for ground, a 20 K difference to explain the anisotropy amplitude in brightness temperature would require a difference of 400

K between ground and sea surface temperature. Therefore, land contamination might be present in the measurements especially at the low elevation angles used in this study but it is not the source of the anisotropy.

Another analysis has been performed where measured data has been compared with the simulated data for each elevation angle, 11°, 9°, 7° and 5°. Measurements taken during clear sky conditions at each of the elevation angles are analyzed and presented by circles in Figure 64 as a scatter plot for the 23.8 and 30.0 GHz. This result shows the spectral signature of water vapor for various elevation angles.

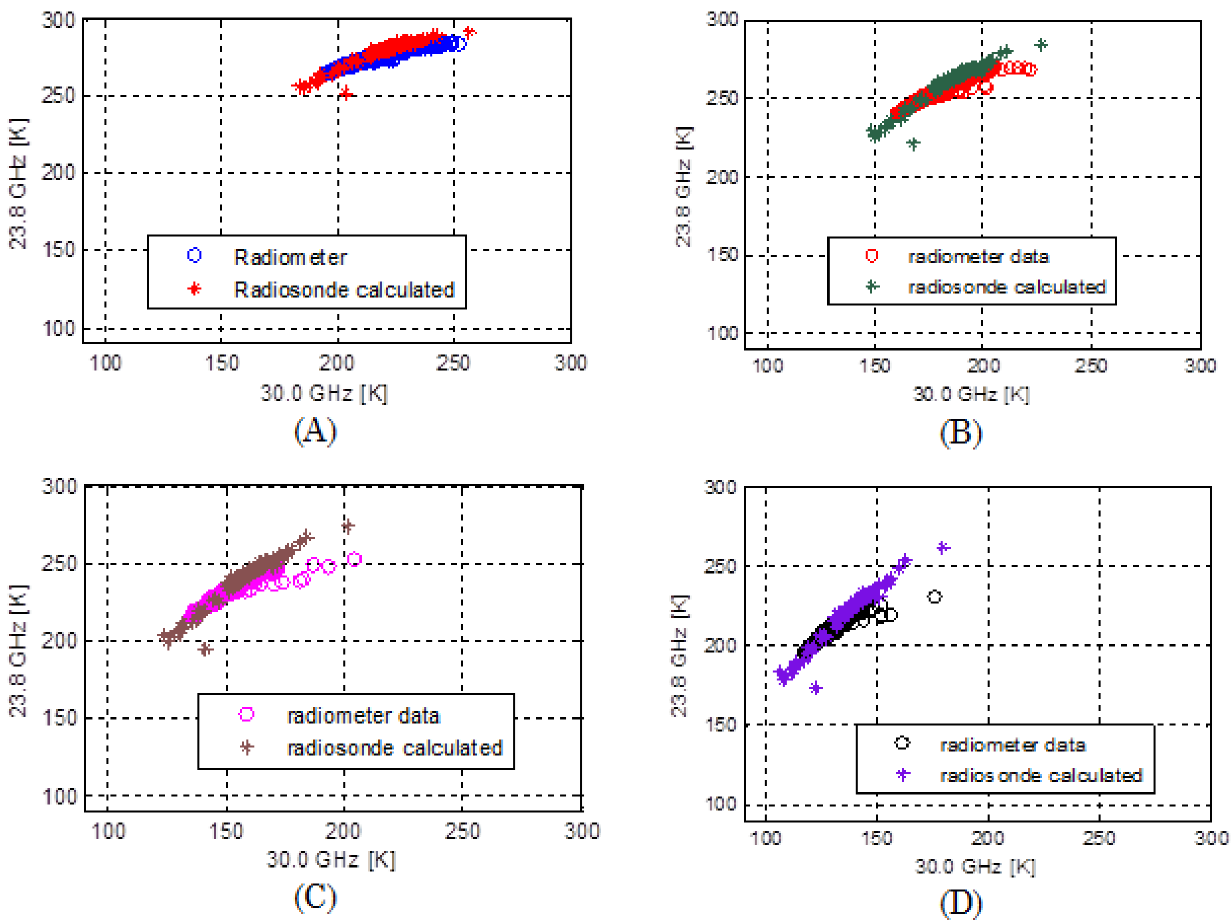

Figure 64: The brightness temperature scatter plot for 23.8 and 30 GHz for elevation angles 5°, 7°, 9° and 11° shown in plots A, B, C and D respectively. The simulated brightness temperatures from radiosondes are also presented along with the radiometer measurements. (50 radiosondes and 500 points).

Radiosonde measurements which are temporally co-located with the radiometer measurements are used to simulate the brightness temperatures for the frequencies 23.8 and 30.0 GHz using radiative transfer equation and are presented by the esteriques.

The scatter plots for 23.8 and 30 GHz based on radiometer measured and radiosonde simulated data show that 80% of the data are comparable particularly when the amount of water vapor present in the atmosphere is low to medium. In case of land contamination most of the simulated brightness temperatures would not be comparable to the measurements and spectral signature will be completely different. Therefore, the hypothesis of land contamination being a source of the measurement anisotropy can be rejected.

7.2.2.2 Radio Frequency Interference as Source of Anisotropy

Analysis has been performed to determine if RFI is a possible source of the azimuth anisotropy observed during clear sky conditions. The measurement can be represented as Eqn. (VII.2)

$$T_A = [1 - \Gamma(\rho)]T_{mr} + \Gamma(\rho)T_x(az) \tag{VII.2}$$

where

- T_A is the measured antenna temperature
- $\Gamma(\rho)$ is the transmisitivity of the atmosphere which changes due to variation in temperature, water vapor and liquid water
- T_{mr} is the mean radiating temperature of the atmosphere
- $T_x(az)$ is the brightness temperature contributor varying with azimuth angle
- az is the azimuth angle varying from -50º to 150º

Based on Eqn. (VII.2) there can be two cases Eqn. (VII.3):

1) Assuming a very wet day, $\Gamma(\rho)$ = 0, the atmosphere appears homogeneous because there is lot of contribution from liquid water and humidity. So the Eqn. (VII.2) can be written as Eqn. (VII.3)

$$T_A = T_{mean} \tag{VII.3}$$

So, there is no pattern in the measured brightness temperatures.

2) Assuming a slightly wet day, $\Gamma(\rho)$ = 0.5, the atmosphere appears inhomogeneous because the contribution varies with the azimuth angle of measurement. Eqn. (VII.2) can be written as Eqn. (VII.4)

$$T_A = 0.5T_{mean} + 0.5T_x(az) \tag{VII.4}$$

There is a pattern in the measurements. Possible sources of RFI:

1) One possible source of RFI could be present at azimuth angles between 200º to 240º as shown by the yellow lines in Figure 65. But there is no land mass in that direction for about 500-1000 km.

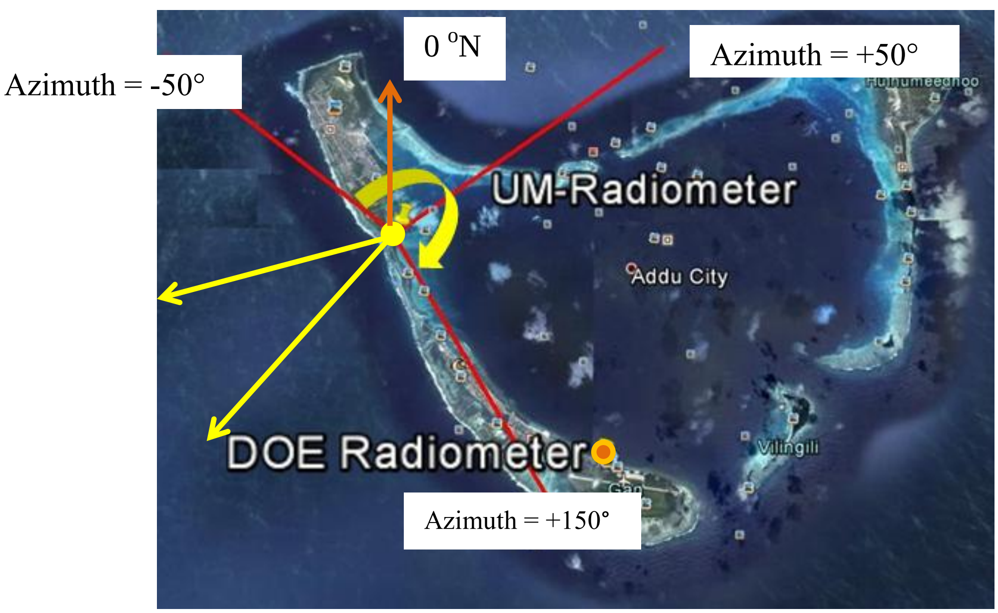

Figure 65: Map of the locations of the University of Miami microwave radiometer (shown by the yellow disk) and the DOE radiometer (shown by the orange disk) on Gan Island, Maldives.

2) SPol-Ka radar: Chances are low since the radar is very close to the radiometer and the signal from this radar would saturate the radiometer channels. If this radar is the RFI source then it has to be due to some kind of leakage and the angular dependence cannot be explained in that case.
3) Ka band radar at the ARM site: The ARM site is about 8.5 km away from the radiometer site and is at an azimuth of about 130º. Therefore, the observed azimuth pattern cannot be created by the emitted signal.

Based on this analysis, it is confirmed that RFI is not a source of the anisotropy.

7.2.2.3 Radiometer Tilt as Source of Anisotropy

Another possible explanation for the observed anisotropy is the tilt in the radiometer during azimuth angle scan for the elevation angles of 5º to 11º. The sand under the base of the radiometer might have moved slightly leading to 0.5º to 1º variation in the elevation angles. Brightness temperatures were simulated at elevation angles of 4º, 4.5º, 5º and 5.5º at 23.8º and 30.0º GHz using a radiative transfer model to estimate the impact of the variation in elevation angles on the measurements as shown in Figure 66. It is observed that a variation of 0.5-1º in the elevation angle produces a change of 10 and 20 K in the simulated brightness temperatures at 23.8 and 30 GHz frequencies, respectively. This is similar to the anisotropy amplitude observed in the measured brightness temperatures. Thus, radiometer tilt is a possible source of anisotropy observed in the measurements. These results corroborate with the results in Figure 63. As can be observed there is a slight tilt for the first 75 days and then a sudden increase in tilt which coincides with the decrease in precipitation events.

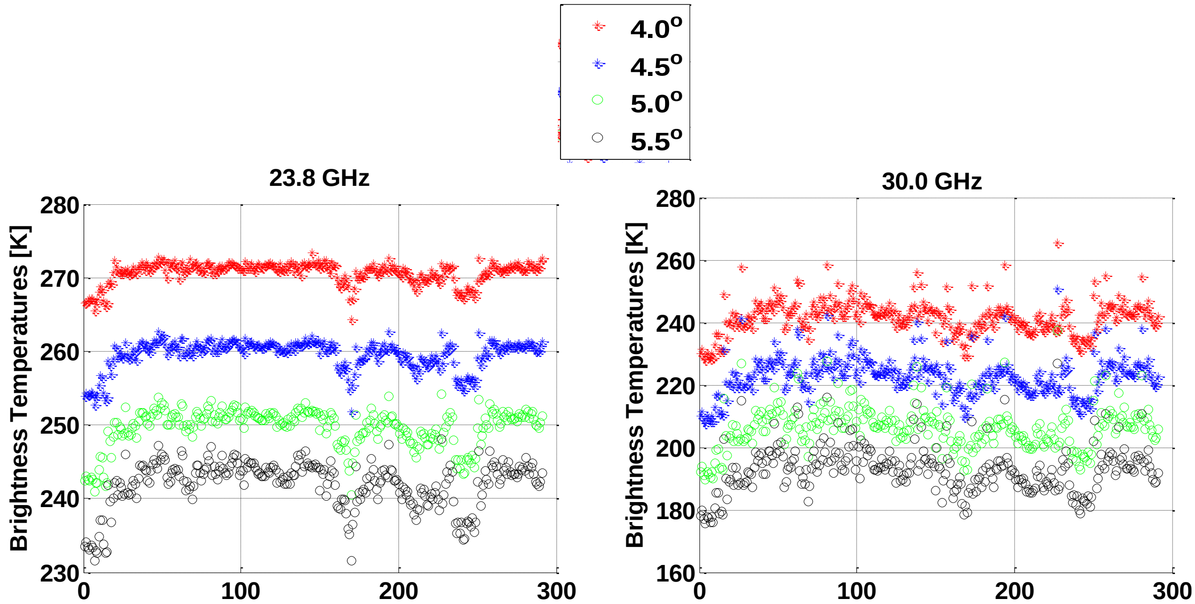

(a) (b)

Figure 66: Variation in brightness temperatures due to changes in elevation angles.

A correlation between the tilt angle and anisotropy amplitude for 23.8 GHz is used to determine the variation in tilt for the whole time period of the experiment as shown in Figure 67 (a). The tilt angles appear to increase as the number of precipitation events reduce and the liquid water in the atmosphere reduces which occurs close to the 75th day of experiment. The tilt angle for the 80th day corresponding to the azimuth angles are shown in Figure 67 (b).

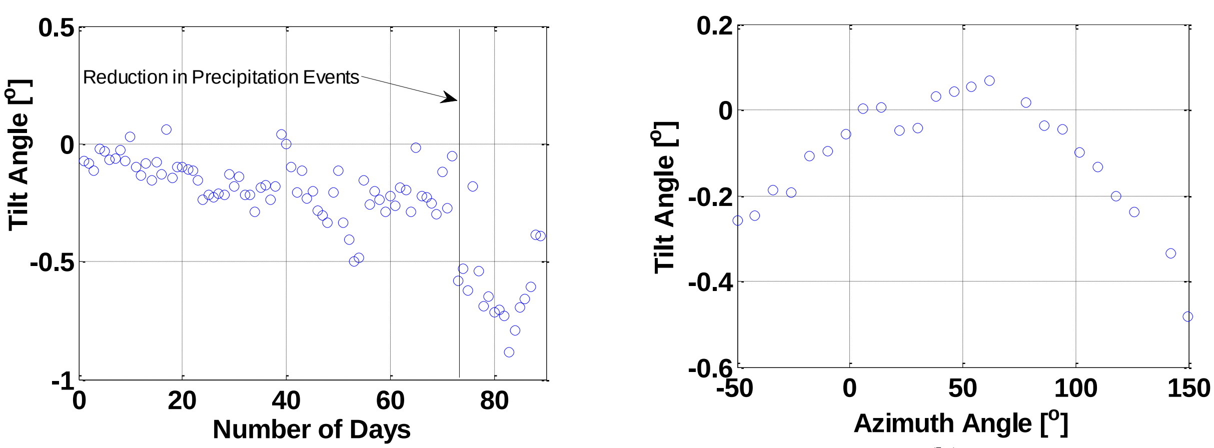

(a) (b)

Figure 67: (a) Variation in tilt angle during the whole time period of the experiment (b) Tilt angle for the azimuth angle range of -50 to 150 at 13:00 UTC on 31-Dec-2011.

To determine the variation in elevation angles with time, tilt angles were calculated for all the measurements corresponding to azimuth angles similar to that in Figure 67 (b).

7.3. Conclusions

Various analyses were performed to determine the possible source/sources of azimuth anisotropy observed in Figure 51. Water vapor and liquid water present in the atmosphere affect measurements at 23.8 and 30 GHz, respectively; hence ground measurements of these parameters were analyzed to determine their correlation with the azimuth anisotropy. Similarly, wind direction and speed at ground level were also analyzed to determine their correlation with the azimuth anisotropy. It was observed that in-situ measurements of wind direction and water vapor are correlated with the azimuth anisotropy while wind speed and liquid are not.

Other possible reasons for the anisotropy i.e., land contamination, RFI and radiometer tilt were also analyzed. It was found that a radiometer elevation angle variation of 0.5° to 1° produces a brightness temperature difference of 10-20 K and 20-30 K for 23.8 GHz and 30 GHz measurement frequencies, respectively. These values of brightness temperatures are similar to the anisotropy amplitude observed in Figure 51. It is inferred from the analysis that the possible sources of azimuth anisotropy are water vapor, wind direction and the tilt of radiometer.

Chapter VIII Slant Water Path, Slant Liquid Water Retrievals and Rainfall Intensity during the DYNAMO Experiment

8.1. Introduction

In this study, vapor-liquid water ratio (VLWR) has been developed and its sensitivity to both water vapor and liquid water has been analyzed. This chapter focuses on the development of a new retrieval algorithm using the VLWR and ground-based brightness temperature measurements for zenith to low elevation angles to estimate slant water path (SWP) and slant liquid water (SLW). This algorithm minimizes the squared differences between the measurements and results from models to estimate the SWP and SLW.

8.2. Definition and Discussion of Vapor-Liquid Water Ratio

Water vapor in the atmosphere strongly influences brightness temperatures at 23.8 GHz due to its proximity to the water vapor absorption line at 22.235 GHz. On the other hand, 30.0 GHz is a window frequency between water vapor and oxygen absorption lines, and is mostly affected by liquid water. Therefore, the vapor-liquid water ratio (VLWR) is defined as the ratio of the brightness temperature measured at 23.8 GHz, $T_{B_{23.8}}$, to that at 30.0 GHz, $T_{B_{30.0}}$ Eqn. (VIII.1)

$$\mathrm{VLWR}(\rho_v, \rho_l, P, T) = \frac{T_{B_{23.8}}}{T_{B_{30.0}}} \tag{VIII.1}$$

where ρ_v is the water vapor density, ρ_l is the liquid water density, P is the atmospheric pressure and T is the physical temperature of the atmosphere.

Since VLWR is sensitive to changes in $T_{B_{23.8}}$ and $T_{B_{30.0}}$, it is sensitive to water vapor density, liquid water density, temperature, pressure and also to scattering, which occurs principally in the presence of large water droplets and/or ice particles. Atmospheric temperature has a minimal effect on brightness temperatures at these frequencies, and the pressure profile is typically slowly varying with time and has a second-order impact. Therefore, VLWR is principally sensitive to changes in water vapor, ρ_v, and liquid water, ρ_l. This method is related to that used by Bosisio et. al. [81] to analyze precipitation events.

A theoretical analysis has been performed to determine the sensitivity of VLWR to water vapor density, ρ_v, and liquid water density, ρ_l. The sensitivities of VLWR to each of these quantities are considered separately to improve understanding of the fundamental relationships among these quantities. The partial derivative of VLWR with respect to either water vapor density or liquid water density is given by Eqn. (VIII.2)

$$\frac{\partial VLWR}{\partial \rho_x} = \frac{\partial \left(\frac{T_{B_{23.8}}}{T_{B_{30.0}}}\right)}{\partial \rho_x} = \frac{T_{B_{30.0}} \left(\frac{\partial T_{B_{23.8}}}{\partial \rho_x}\right) - \left(\frac{\partial T_{B_{30}}}{\partial \rho_x}\right) T_{B_{23.8}}}{\left(T_{B_{30.0}}\right)^2} \qquad \text{(VIII.2)}$$

where ρ_x is the density variable, and x represents v for water vapor density or l for liquid water density.

Brightness temperatures at 23.8 and 30.0 GHz are described using the radiative transfer equation [28] given by Eqn. (VIII.3)

$$T_{B_f} = \int_0^\infty T(s)\, \alpha_f(s) e^{-\tau_f(0,s)} sec(\theta) ds + T_{b0} e^{-\tau_f(0,\infty)} \qquad \text{(VIII.3)}$$

$$\tau_f(0,s) = \int_0^s \alpha_f(s) sec(\theta) ds,$$

where:

- $T(s)$ is the atmospheric physical temperature at height *s* above ground,
- $\alpha_f(s)$ is the absorption coefficient at height *s* above the ground at frequency *f*, and $\alpha_f(s) = \alpha_{fdry}(s) + \alpha_{fvapor}(s) + \alpha_{fliquid}(s)$, in which α_{fdry} is the dry component, and α_{fvapor} and $\alpha_{fliquid}$ are the components due to water vapor and liquid water, respectively,
- τ_f is the atmospheric opacity at frequency *f*,

- T_{b0} is the cosmic background brightness temperature (2.73 K, constant at these frequencies), and
- θ is the zenith angle.

The partial derivative of T_{B_f} with respect to ρ_x is given by Eqn. (VIII.4):

$$\begin{aligned}\frac{\partial T_{B_f}}{\partial \rho_x} &\cong \frac{\partial}{\partial \rho_x}\int_0^{\infty} T(s)\,\alpha_f(s)e^{-\tau_f(0,s)}\,sec(\theta)\,ds \\ &= \int_0^{\infty} T(s)\frac{\partial}{\partial \rho_x}\left[\alpha_f(s)e^{-\tau_f(0,s)}\right]sec(\theta)ds \\ &= \int_0^{\infty} T(s)e^{-\tau_f(0,s)}\left[\frac{\partial \alpha_f(s)}{\partial \rho_x} - \alpha_f(s)\frac{\partial \tau_f}{\partial \rho_x}\right]sec(\theta)ds\end{aligned} \tag{VIII.4}$$

where the cosmic background temperature, T_{b0}, has been omitted due to its minimal impact on the calculated brightness temperature. $\frac{\partial \alpha_f(s)}{\partial \rho_x}$ in Eqn. (VIII.4) consists of a dry component as well as components due to water vapor and liquid water, is given by Eqn. (VIII.5):

$$\frac{\partial \alpha_f(s)}{\partial \rho_x} = \frac{\partial \alpha_{fdry}(s)}{\partial \rho_x} + \frac{\partial \alpha_{fvapor}(s)}{\partial \rho_x} + \frac{\partial \alpha_{fliquid}(s)}{\partial \rho_x} \tag{VIII.5}$$

The partial derivatives of the absorption coefficients at frequency f in Eqn. (VIII.5) are principally dependent on density $\rho_x(s)$ and to a lesser extent on temperature and atmospheric pressure [35]. In addition, those parameters that vary most significantly are the water vapor density and liquid water density, while the atmospheric temperature and pressure vary more slowly. The value of $\frac{\partial \alpha_f(s)}{\partial \rho_x} - \alpha_f(s)\frac{\partial \tau_f}{\partial \rho_x}$ changes with the value of ρ_x and also with the zenith angle of measurement, θ, as shown in Eqn. (VIII.3). The factor $\frac{\partial \alpha_f(s)}{\partial \rho_x} - \alpha_f(s)\frac{\partial \tau_f}{\partial \rho_x}$ is positive when $\frac{\partial \alpha_f(s)}{\partial \rho_x} > \alpha_f(s)\frac{\partial \tau_f}{\partial \rho_x}$, which occurs at low zenith angles, i.e. at high elevation angles. In that case, the measured brightness temperature increases linearly with ρ_x, as shown in Figure 68 and explained in the following subsection. On the other hand, as the zenith angle, θ, increases, i.e.

the elevation angle decreases, the value of the term $\frac{\partial \alpha_f(s)}{\partial \rho_x}$ approaches that of $\alpha_f(s)\frac{\partial \tau_f}{\partial \rho_x}$, resulting in $\frac{\partial \alpha_f(s)}{\partial \rho_x} \approx \alpha_f(s)\frac{\partial \tau_f}{\partial \rho_x}$. Substituting Eqn. (VIII.3) and (VIII.4) into Eqn. (VIII.2), we find:

$$\frac{\partial}{\partial \rho_x}(VLWR) = \frac{A-B}{\left(T_{B_{30.0}}\right)^2} \tag{VIII.6}$$

where:

$$A = T_{B_{30.0}} \int_0^\infty T(s) e^{-\tau_{23.8}(0,s)} \left[\frac{\partial \alpha_{23.8}(s)}{\partial \rho_x} - \alpha_{23.8}(s)\frac{\partial \tau_{23.8}}{\partial \rho_x}\right] sec(\theta) ds \tag{VIII.7}$$

$$B = T_{B_{23.8}} \int_0^\infty T(s) e^{-\tau_{30.0}(0,s)} \left[\frac{\partial \alpha_{30.0}(s)}{\partial \rho_x} - \alpha_{30.0}(s)\frac{\partial \tau_{30.0}}{\partial \rho_x}\right] sec(\theta) ds \tag{VIII.8}$$

The term $\left(T_{B_{30.0}}\right)^2$ exhibits a monotonically positive dependence on both water vapor density, ρ_v, and liquid water density, ρ_l. It changes the magnitude of the slope, but the sign of slope is determined by the relative values of A and B. The two terms A and B are strongly dependent on frequency and depend on both water vapor density and liquid water density. Their values determine whether the overall VLWR in Eqn. (VIII.6) has a positive or negative dependence on ρ_x, as shown in the following two subsections.

8.2.1 Vapor-Liquid Water Ratio Sensitivity to Water Vapor

Analyzing the sensitivity of VLWR to water vapor density involves calculation of $T_{B_{23.8}}$ and $T_{B_{30.0}}$ at a variety of elevation angles ranging from 5º to 90º based on 100 atmospheric profiles measured by radiosondes launched from the ARM site on Gan Island during October 2011. In this analysis, the selected radiosondes were for clear sky conditions, so the liquid water density is set to zero in the simulations. The modeled VLWR values based on simulated brightness temperatures are shown in Figure 68 as a function of SWP in symbols of various colors corresponding to each elevation angle from 5º to 90º. VLWR is in the range of 1.8 to 2.2 for elevation angles from 50° to 90° and in the range of approximately 1.7 to 2 for elevation angles from 20° to 30°, and less than 1.7 for elevation angles from 5º to 11º. The VLWR values are approximately proportional to SWP for elevation angles from 30º to 90º and nearly independent of changes in SWP for elevation angles from 15º to 20º. In contrast, VLWR decreases as SWP increases for elevation angles from 5º to 11º.

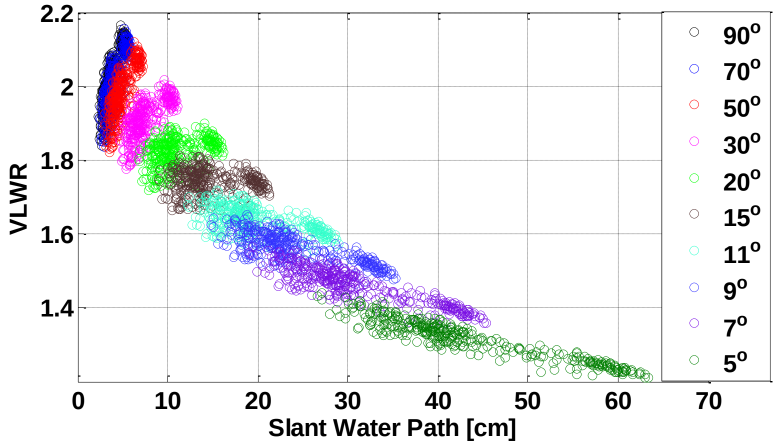

Figure 68: VLWR values for a range of SWP at elevation angles from 5° to 90°.

At higher elevation angles the brightness temperatures at 23.8 and 30.0 GHz are increasing linearly with water vapor path and brightness temperature at 23.8 GHz is higher than those at 30 GHz. This is because 23.8 GHz is more sensitive to changes in water vapor than 30 GHz. Therefore, an increase in water vapor path results in increase in VLWR. As the elevation angles decrease, the rate of increase in brightness temperature at 23.8 GHz becomes similar to that of rate of increase in at 30.0 GHz. This is because of the high amount of attenuation at 23.8 GHz because the radiometer ray passes through high amount of water vapor present in lower parts of troposphere. This results in the VLWR sensitivity close to one.

However, when the elevation angles are lower than 15º the brightness temperatures increase with slant water vapor path follow a different relationship for 23.8 and 30 GHz. Brightness temperatures at 23.8 GHz increase non-linearly while those at 30.0 GHz increase linearly. This is because of high amount of attenuation at 23.8 GHz. The 30 GHz is less attenuated at these elevation angles so they continue to increase linearly. Thus, the VLWR sensitivity values decrease as the SWVP increases. However, it is important to observe that VLWR values are always greater than one, which is because of the brightness temperatures at 23.8 GHz being greater than those at 30.0 GHz for clear sky conditions.

Based on the simulation results and the theoretical water vapor sensitivity analysis, the sensitivity of VLWR to water vapor in the atmosphere, i.e., $\frac{\partial VLWR}{\partial \rho_v}$, has three distinct regions, depending on the elevation angle of measurement, as explained below.

1. The region where VLWR increases with increasing water vapor i.e., $\frac{\partial VLWR}{\partial \rho_v} > 0$, corresponds to elevation angles from 30° to 90° i.e., Figure 68. For this region, $A > B$ i.e., $\left(\frac{\partial \alpha_{23.8v}(s)}{\partial \rho_v} - \alpha_{23.8v}(s)\frac{\partial \tau_{23.8v}}{\partial \rho_v} \gg \frac{\partial \alpha_{30v}(s)}{\partial \rho_v} - \alpha_{30v}(s)\frac{\partial \tau_{30v}}{\partial \rho_v}\right)$, and an increase in the absorption coefficient at 23.8 GHz (due to an increase in water vapor) has greater impact than an increase in path length does due to increasing zenith angle, so $\frac{\partial VLWR}{\partial \rho_v} > 0$.
2. The region where the VLWR is nearly independent of changes in water vapor i.e., $\frac{\partial VLWR}{\partial \rho_v} \approx 0$ corresponds to elevation angles from 15° to 20°. For this region, $A \approx B$ i.e., $\left(\frac{\partial \alpha_{23.8v}(s)}{\partial \rho_v} - \alpha_{23.8v}(s)\frac{\partial \tau_{23.8v}}{\partial \rho_v} > \frac{\partial \alpha_{30v}(s)}{\partial \rho_v} - \alpha_{30v}(s)\frac{\partial \tau_{30v}}{\partial \rho_v}\right)$ and an increase in the absorption coefficient at 23.8 GHz (due to an increase in water vapor) is nearly balanced by the increase in the path length due to increasing zenith angle, θ, so $\frac{\partial VLWR}{\partial \rho_v} \approx 0$.
3. The region where VLWR decreases with increasing water vapor i.e., $\frac{\partial VLWR}{\partial \rho_v} < 0$ corresponds to elevation angles from 5° to 11°. For this region, $A < B$ i.e., $\left(\frac{\partial \alpha_{23.8v}(s)}{\partial \rho_v} - \alpha_{23.8v}(s)\frac{\partial \tau_{23.8v}}{\partial \rho_v} <\right.$

$\frac{\partial \alpha_{30v}(s)}{\partial \rho_v} - \alpha_{30v}(s)\frac{\partial \tau_{30v}}{\partial \rho_v}\Big)$, and an increase in the path length due to increasing zenith angle has greater impact than an increase in the absorption coefficient at 23.8 GHz (due to an increase in water vapor), so $\frac{\partial VLWR}{\partial \rho_v} < 0$.

This dependence of VLWR on elevation angle is due to both the distribution of water vapor in the atmosphere, which is larger near the ground, and the path length along the radiometer's field of view close to the ground level since longer path lengths correspond to lower elevation angles.

8.2.2 Vapor-Liquid Water Ratio Sensitivity to Liquid Water

The analysis in the previous subsection focuses on the sensitivity of VLWR to water vapor under clear sky conditions. Here, the effect of liquid water on VLWR is considered. IWV is held constant at a value of 3.12 cm, which is the same as SWP at 90° elevation angle, while the ILW (and by extension, SLW) is varied based on the cloud liquid water content. Humidity profiles from radiosondes are used to compute liquid water density [82] profiles. The profiles of liquid water density and water vapor density are used to calculate absorption coefficients at 23.8 and 30.0 GHz using commonly-accepted atmospheric absorption models in this frequency range [28] [31] [33]. Liquid water density is calculated from radiosonde data using Eqn. (VIII.9) [82]

$$W = \begin{cases} 0 & RH < b_0 \text{ or } T < 240\ K \\ 2\left(\frac{RH - b_0}{30\%}\right) & RH > b_0 \text{ and } T > 240\ K \end{cases} \tag{VIII.9}$$

where:

- W is the liquid water density in g/m^3,
- RH is the relative humidity,
- b_0 is the threshold relative humidity percentage for liquid water formation set at 95%, and
- T is the physical temperature.

Liquid water absorption coefficients are calculated using Eqn. (VIII.10) [83]

$$\alpha_{fliquid} = 6\pi 10^{-2} \frac{Im\{\epsilon_f\}}{\left|\epsilon_f + 2\right|^2} Wf \tag{VIII.10}$$

where:

- $\alpha_{fliquid}$ is the absorption coefficient in Np/km for the frequency *f*, at 23.8 or 30.0 GHz,
- f is the frequency, and
- ϵ_f is the relative dielectric constant of cloud liquid water [33].

Liquid water absorption coefficients are added to the dry and water vapor absorption coefficients, as in Eqn. (VIII.5). The total absorption, $\alpha_f(s)$, is used in Eqn. (VIII.3) to simulate values of $T_{B_{23.8}}$ and $T_{B_{30.0}}$, which are then used to calculate VLWR. Figure 69 shows the relationship between VLWR and ILW at elevation angles of 5°, 11°, 30°, 50° and 90°. Based on the above analysis, as the liquid water content increases, VLWR decreases to near unity as the brightness temperatures at 23.8 GHz and 30.0 GHz become similar in value. In strong precipitation, VLWR values can decrease to less than unity for any measured elevation angle, particularly due to scattering. However, the slope of the curves, or rate of decrease of VLWR with increase in ILW, decreases as the elevation angle decreases, as shown in Figure 69.

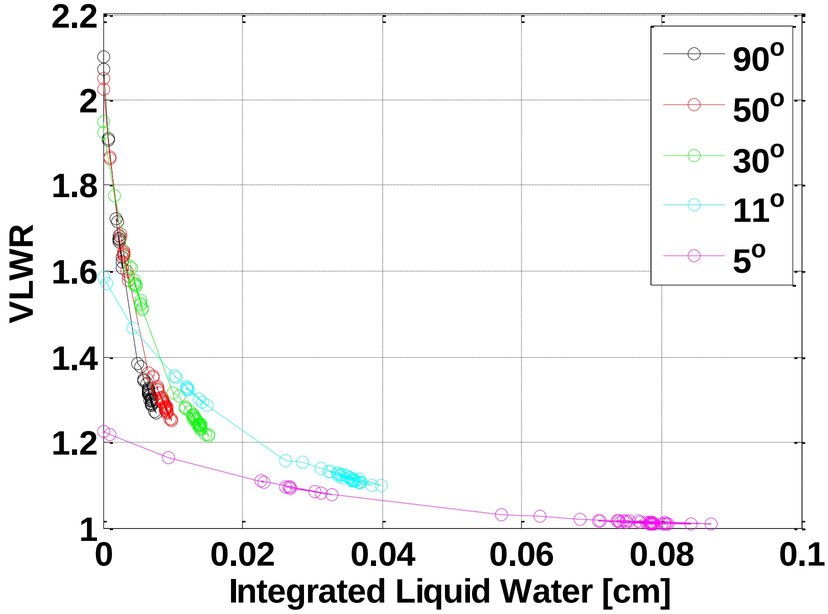

Figure 69: VLWR values for range of ILW for elevation angles of 5°, 11°, 30°, 50° and 90°.

Using the results in Figure 69 and the theoretical sensitivity analysis of $\frac{\partial VLWR}{\partial \rho_l}$, the sensitivity of VLWR to liquid water in the atmosphere has two distinct regions based on elevation angle.

1. The first region with a large negative slope i.e., $\frac{\partial VLWR}{\partial \rho_l} \ll 0$ corresponds to elevation angles from 20° to 90°. For this region, $B \gg A$ i.e., $\left(\frac{\partial \alpha_{30.0l}(s)}{\partial \rho_l} - \alpha_{30.0l}(s)\frac{\partial \tau_{30.0l}}{\partial \rho_l} \gg \frac{\partial \alpha_{23.8l}(s)}{\partial \rho_l} - \alpha_{23.8l}(s)\frac{\partial \tau_{23.8l}}{\partial \rho_l}\right)$ and $T_{B_{23.8}} > T_{B_{30.0}}$.

2. The second region with a smaller negative slope i.e., $\frac{\partial VLWR}{\partial \rho_l} < 0$ corresponds to elevation angles less than 11°. For this region $B > A$ i.e., $\left(i.e., \frac{\partial \alpha_{30.0l}(s)}{\partial \rho_l} - \alpha_{30.0l}(s)\frac{\partial \tau_{30.0l}}{\partial \rho_l} > \frac{\partial \alpha_{23.8l}(s)}{\partial \rho_l} - \alpha_{23.8l}(s)\frac{\partial \tau_{23.8l}}{\partial \rho_l}\right)$ and $T_{B_{23.8}} > T_{B_{30.0}}$.

In addition, for liquid water, this dependence of VLWR on the elevation angle is due to the distribution of water vapor and liquid water in the atmosphere, as well as the path length of the atmosphere along the radiometer field of view, with longer path lengths corresponding to lower elevation angles.

8.3. Vapor Liquid Water Ratio Sensitivity to Precipitation

The sensitivity of VLWR to variation in liquid water present in the atmosphere is significant as already discussed in Section 8.2.2. Here, the change in VLWR due to variation in precipitation intensity is analyzed by using VLWR measured during precipitation of various intensities in the range of 15-55 dBZ where 15 dBZ corresponds to light and 55 dBZ corresponds to heavy precipitation, respectively. Figure 70 shows a particular precipitation event with intensity in the range of 50-55 dBZ. The precipitation event is primarily concentrated in the azimuth angle of -90º to 90º where the most intense precipitation is over the radiometer.

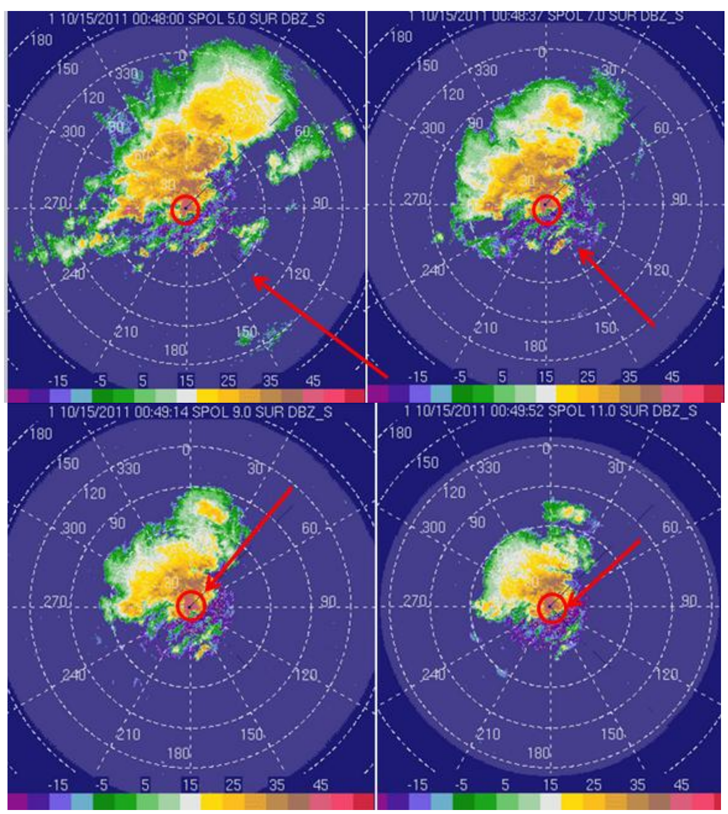

Figure 70: Precipitation event with radar reflectivity values in the range of 50-55 dBZ [84].

The VLWR values corresponding to the various azimuth (-50º to 150º) and elevation angles (5º, 7º, 9º and 11º) are calculated and shown in Figure 71. It can be observed that the VLWR values are less than one in Figure 71 for most of the azimuth and elevation angles. This is because heavy precipitation is observed over the radiometer location. The heavy precipitation can be inferred from the VLWR values for the azimuth angles of -50º to 38º.

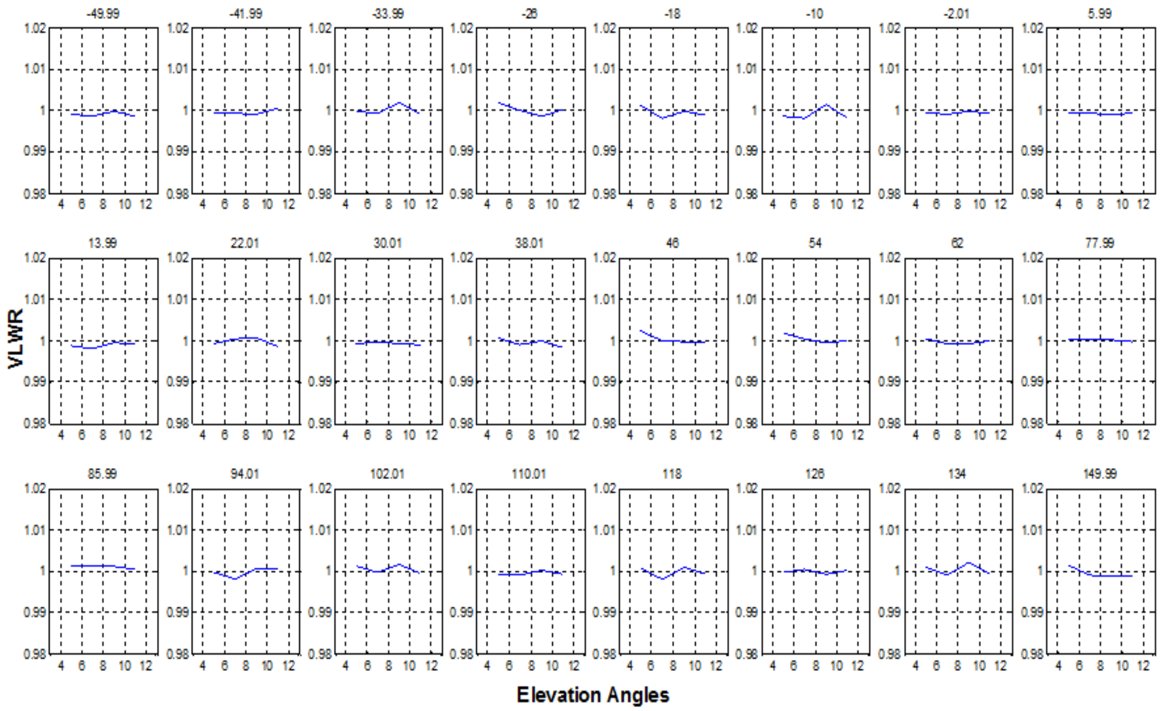

Figure 71: VLWR value corresponding to the precipitation event shown in Figure 70 depending on the elevation angle.

VLWR sensitivity to precipitation intensity is analyzed further by taking another case. Here the precipitation is of mixed intensities varying from light to heavy. The radar reflectivity data for this case is shown in Figure 72 where the precipitation intensity again varies from 15 to 55 dBZ. The precipitation is spread over the azimuth angles ranging from -120º to 120º where -90º to -30º correspond to heavy precipitation, -30º to 120º correspond to light and moderate precipitation. The corresponding VLWR values are shown in Figure 73. The VLWR values change with precipitation intensity and distance along the line of sight of the radiometer. The

VLWR values for light to moderate precipitation are in the range of 1-1.3 for most of the cases while for heavy precipitation it is close to one. Particularly, the light precipitation observed at approximately 30 km from radiometer at azimuth angle of 60º has VLWR values in the range 1-1.3.

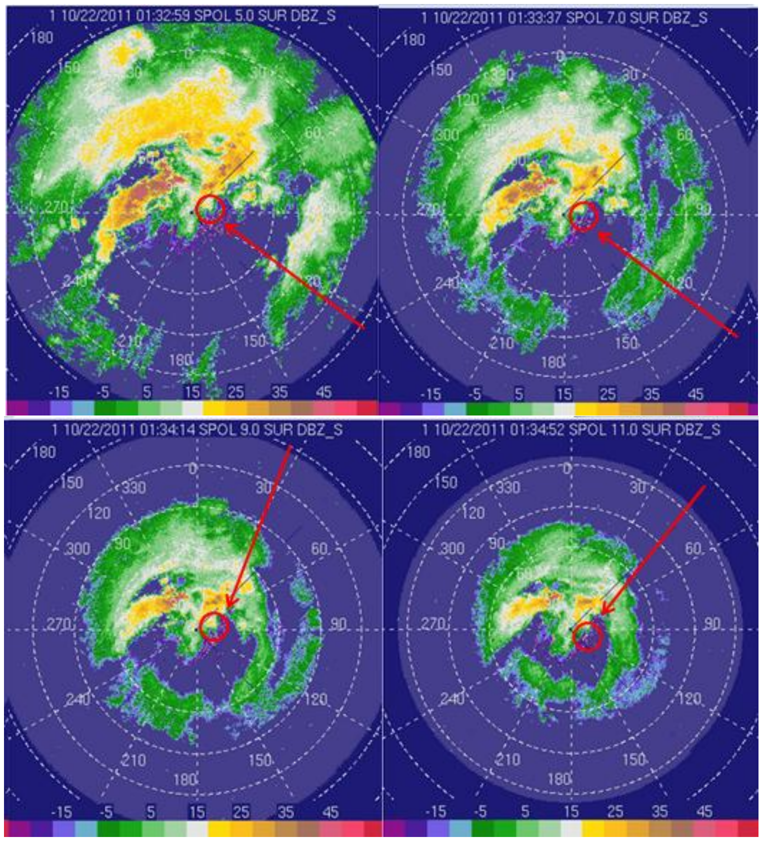

Figure 72: Precipitation close to the radiometer with radar reflectivity values in the range of 15-25 dBZ.

These values can be considered as threshold value of VLWR corresponding to light precipitation. Any values of VLWR below these will mean increase in precipitation intensity. Based on these values it can be inferred that for each elevation angle there are minimum and maximum values of VLWR for heavy and light, respectively.

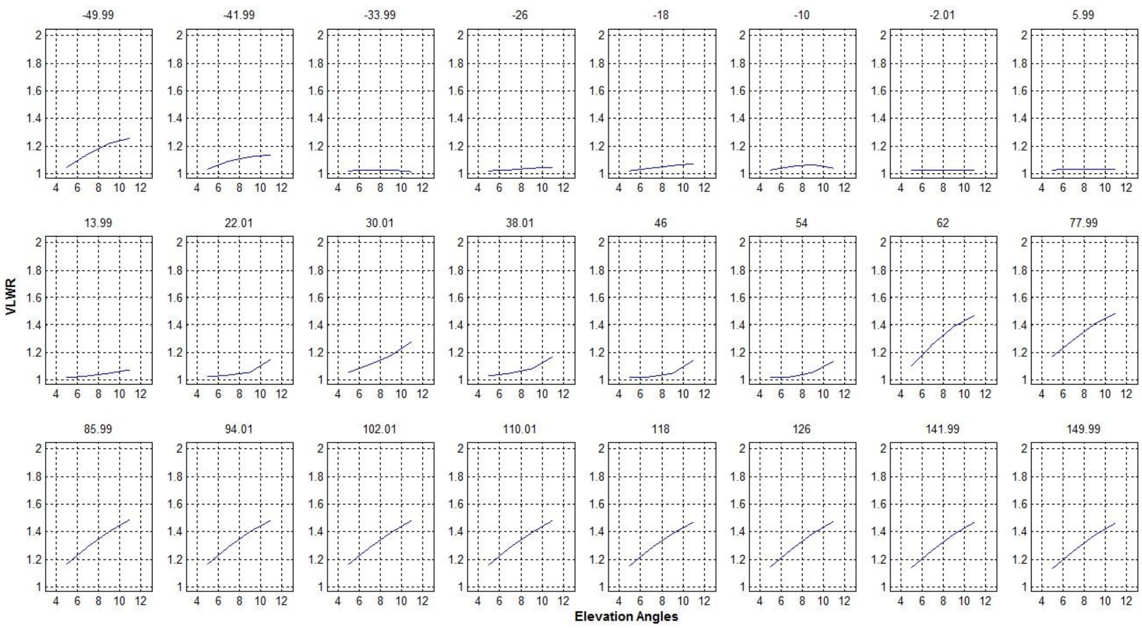

Figure 73: VLWR values corresponding to the precipitation event shown in Figure 72.

To calculate the minimum value of VLWR, 20 cases of heavy rainfall events similar to the one seen in Figure 70 are considered and the mean value is calculated. Results are shown in Figure 74. The mean minimum values are approximately one for all the elevation angles.

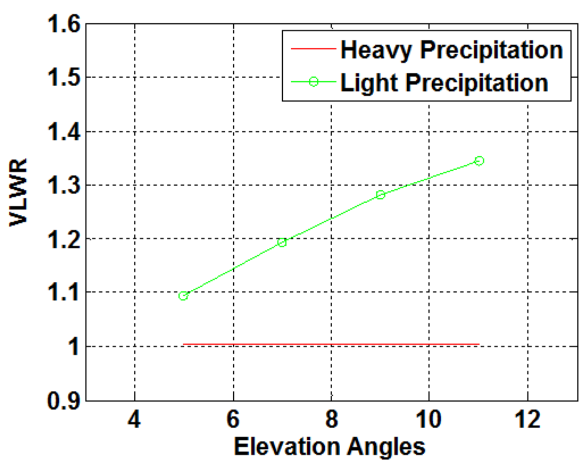

Figure 74: VLWR values for heavy and precipitation for various elevation angles.

Similarly mean threshold values of VLWR for various elevation angles are computed using 15 cases of light precipitation using cases shown in Figure 72. The mean threshold values vary from 1.1 to 1.35 for elevation 5º to 11º.

8.4. Sensitivity of VLWR to Distance of Precipitation Event from Radiometer

Along with variation in rain intensity, variation in precipitation distance from radiometer also affects the VLWR values. Variation in rainfall distance from radiometer is hereby known as precipitation range. To determine the impact of precipitation range on VLWR, regression analysis is performed where precipitation range values determined from radar measurements are used along with VLWR values to develop a relationship. The results of the regression are shown in Figure 75.

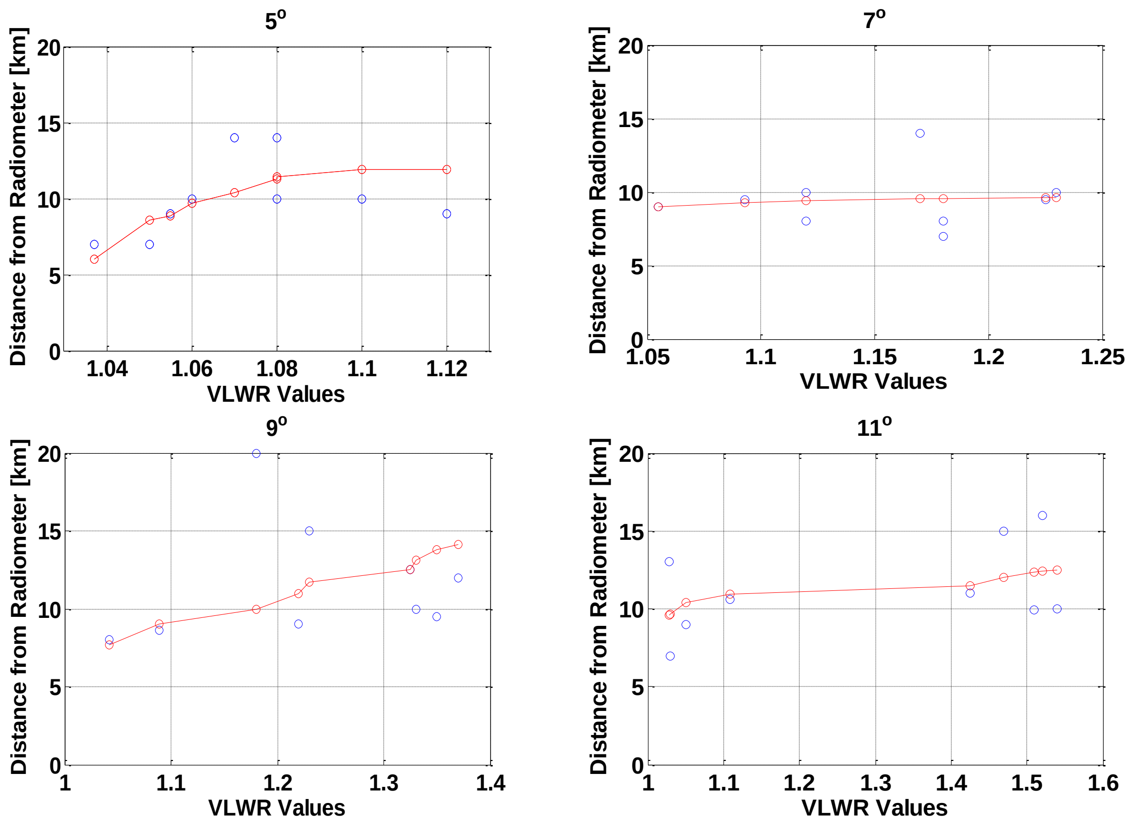

Figure 75: VLWR and precipitation distance relationship.

It is observed that, for elevation angles of 5°, 9° and 11°, the VLWR is sensitive to changes in precipitation range and there is a second order relationship between precipitation range and VLWR. However, for 7° elevation angle the VLWR is not sensitive to changes in precipitation range.

8.5. Retrieval of Integrated Water Vapor and Integrated Liquid Water for Zenith Measurements

As seen in the Section 8.2, VLWR is sensitive to liquid water water vapor, as well as the elevation angle of brightness temperature measurements. The sensitivity of VLWR to these parameters allows retrieval of integrated water vapor (IWV) and integrated liquid water (ILW) in the atmosphere and therefore the SWP and SLW as a function of elevation angle.

8.5.1 Retrieval Algorithm for IWV and ILW

Based on results of the sensitivity analysis of VLWR, a retrieval algorithm was developed to estimate IWV and ILW, as shown in Eqn. (VIII.11). This algorithm minimizes the squared differences between modeled and measured VLWRs as well as that between modeled and measured brightness temperatures at 30.0 GHz Eqn. (VIII.11).

$$\min_{\tau_{23.8},\tau_{30.0}} \chi^2 = |VLWR_{model} - VLWR'|^2 + \left|T_{B_{30.0}\,model} - T'_{B_{30.0}}\right|^2 \tag{VIII.11}$$

where:

- $VLWR_{model}$ is modeled VLWR for the IWV range of 0 to 9 cm and ILW range of 0 to 0.6 mm,
- $VLWR'$ is the VLWR calculated from the measured brightness temperatures at 23.8 GHz and 30.0 GHz,
- $T_{B_{30.0}\,model}$ and $T'_{B_{30.0}}$ are the modeled and measured brightness temperatures at 30.0 GHz, respectively. The brightness temperatures at 23.8 and 30.0 GHz are modeled using IWV and ILW from 700 radiosonde profiles collected at the ARM site on Gan Island during the months of June to August 2011. These data were interpolated to generate a brightness temperature model for the ranges of IWV and ILW mentioned above, for a zenith pointing

radiometer, as shown in Figure 76(a). It is inferred that modeled brightness temperature at 30 GHz is sensitive to changes in ILW and has no sensitivty to IWV variation.

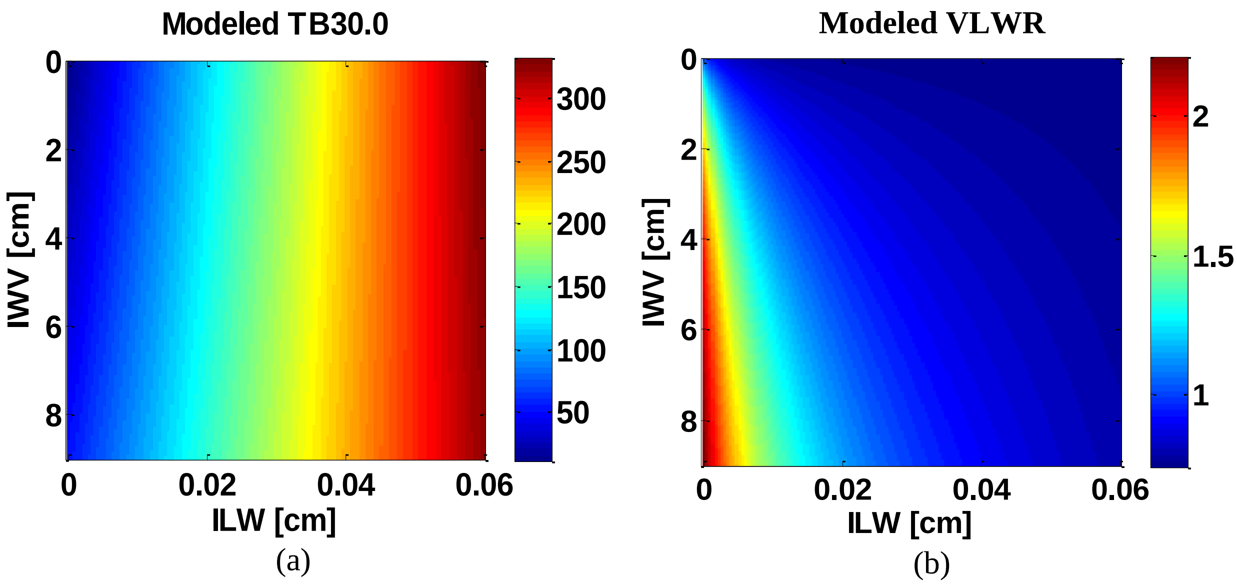

Figure 76: (a) Modeled brightness temperatures at 30 GHz, and (b) Modeled VLWR values for the IWV from 0 to 9 cm and ILW from 0 to 0.6 mm.

The modeled VLWR was calculated using Eqns. (VIII.1) and (VIII.3), and the results are shown in Figure 76(b). The modeled VLWR is larger than 2.0 when the ILW is less than 0.005 cm and the IWV is greater than 2.8 cm. When the ILW is above 0.025 cm for all values of IWV considered, the VLWR is less than or equal to unity. $VLWR_{model}$ and $T_{B_{30.0}model}$ calculated in this way are used to retrieve IWV and ILW from brightness temperatures measured by the UM-radiometer on December 15, 2011 at 05:30 UTC. The results of the retrieval are shown in Figure 77. The curve starting near the y-axis and ending on the x-axis shows the locus of points where the measured VLWR is equal to the modeled VLWR, i.e., the minimum of the first term in Eqn. (VIII.11).

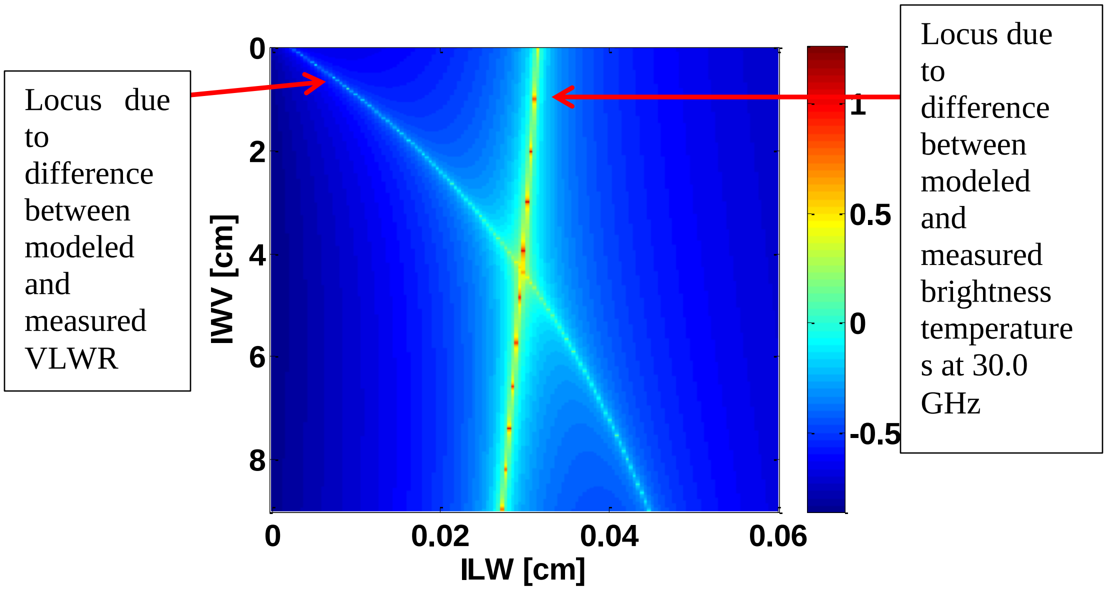

Figure 77: Intersection of the two loci representing the two terms in Eqn. (VIII.11).

From the first term, the VLWR (equal to 1.01 from measurements) could be produced by a range of ILW from 0 to 0.045 cm and a range of IWV from 0 to 9 cm. The nearly-vertical curve in the figure shows the locus of points where the measured $T'_{B_{30.0}}$ and modeled $T_{B_{30.0_{model}}}$ are equal, i.e., the minimum of the second term in Eqn. (VIII.11). From the second term, the measured $T'_{B_{30.0}}$ could be produced by a range of IWV from 0 to 9 cm but by only a narrow range of ILW, from 0.025 to 0.035 cm. From the intersection of the two loci in Figure 77, the estimated value of the IWV is found to be 4.36 cm and that of ILW is 0.032 cm.

This algorithm has been used to retrieve time series of IWV and ILW for December 15, 2011 as shown in blue in Figure 78 and Figure 79, respectively. IWV and ILW retrieved during precipitation are represented by the green circles around the corresponding blue points. Precipitating conditions have been determined when the VLWR value decreases below an empirically-determined threshold value of 1.2, based on mean VLWR determined for various light precipitation events during DYNAMO.

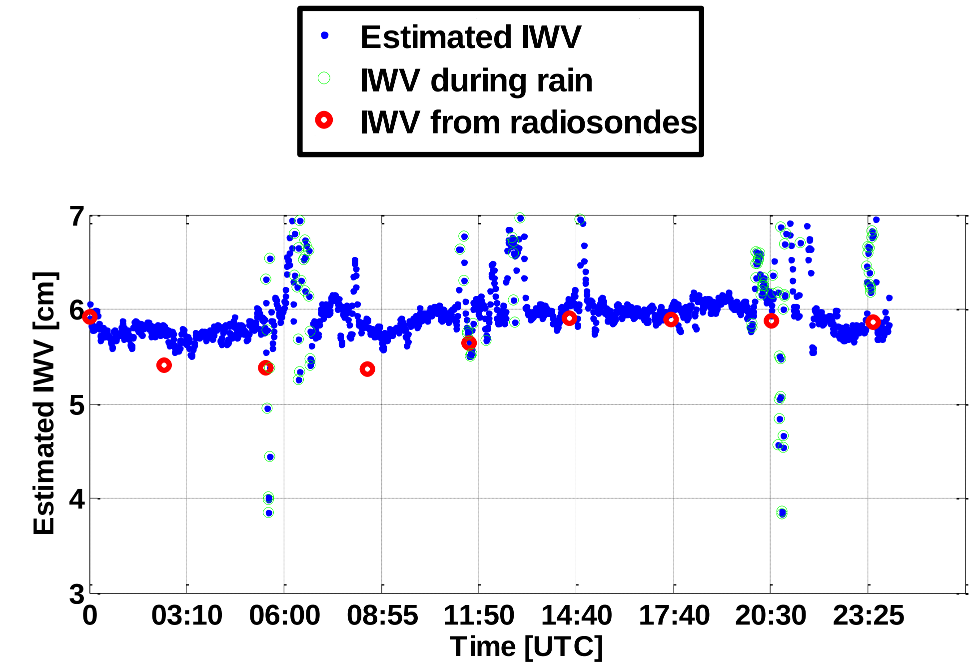

Figure 78: Time series of estimated integrated water vapor (IWV) from UM-radiometer measurements on December 15, 2011.

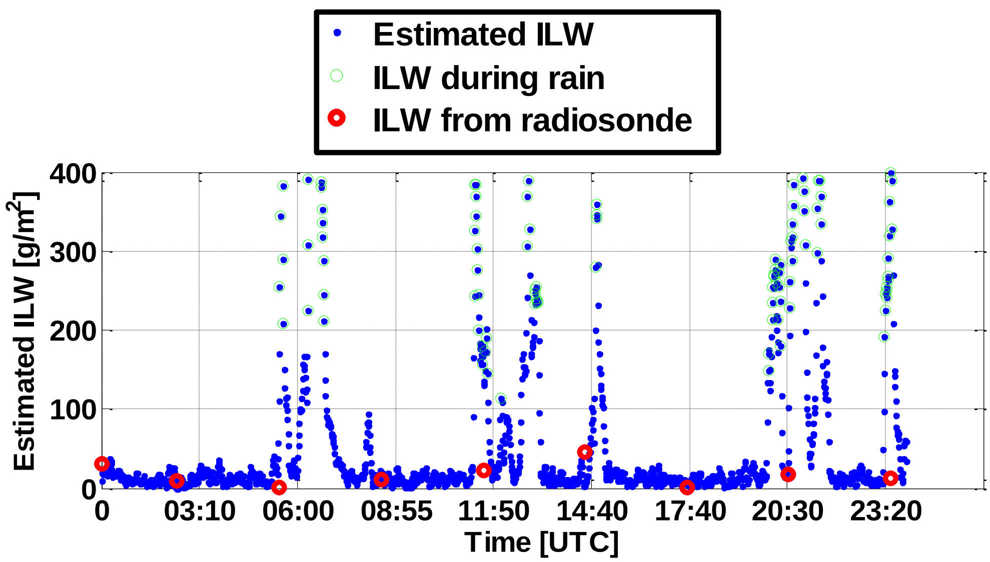

Figure 79: Time series of estimated integrated liquid water (ILW) from UM-radiometer measurements on December 15, 2011.

This is believed to be due to the fact that the DOE ARM radiosonde launch site was 8.5 km southeast of the UM-radiometer, and there was significant variability of water vapor and liquid water on this spatial scale. The red circles in Figure 78 and Figure 79 show the IWV and ILW, respectively, calculated from measurements using the 9 radiosondes launched on December 15,

2011. Retrieved IWV and ILW compare well with IWV and ILW measured by radiosondes. However, IWV and ILW from radiosondes launched at 02:30, 05:30 and 08:30 UTC exhibit lower values of IWV than the retrieved values.

8.5.2 IWV and ILW Observation System Simulation Experiment and Retrieval Performance of a Zenith-Pointing Radiometer

An Observation System Simulation Experiment (OSSE) was performed to determine the uncertainty associated with the retrieval algorithm used in the previous subsection. As part of the OSSE, atmospheric measurements from 500 radiosondes launched during August and September 2011 were used to simulate brightness temperatures at 23.8 and 30.0 GHz, from which the IWV and ILW were estimated using Eqn. (VIII.11). The uncertainty associated with the IWV retrieval algorithm was calculated as the difference between the estimated IWV and that measured by radiosondes. The average IWV retrieval uncertainty was calculated in each of 10 bins of 0.25 cm width, shown in Figure 80 as 3.5% to 4.5% for IWV values from 4.0 to 6.5 cm.

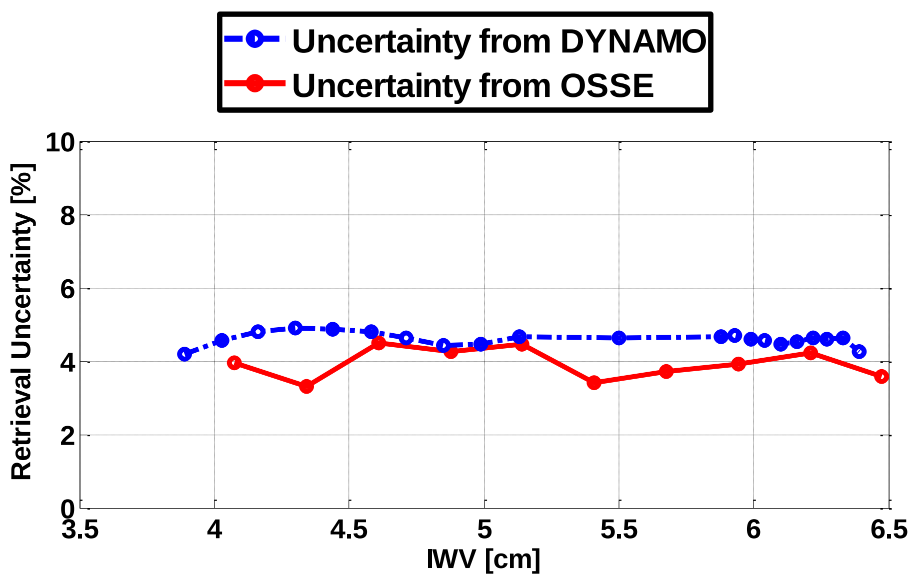

Figure 80: IWV retrieval uncertainty from OSSE (in red) and difference between radiometer estimates and radiosonde data measured during DYNAMO (in blue)

Similarly, the uncertainty associated with the ILW retrieval algorithm was calculated as the difference between the estimated ILW and that measured by radiosondes. The average ILW retrieval uncertainty was calculated in each of 10 bins of 0.004 cm width, shown in Figure 81 as 12% for ILW of 0.005 cm, decreasing to 5% for ILW of 0.0175 cm or greater and decreasing to 3% for ILW of 0.0275 cm or greater. Retrieval uncertainties for both IWV and ILW from the OSSE have generally similar values to the difference between retrieved values from DYNAMO data and radiosonde interpolated values, as shown in Figure 80 and Figure 81, respectively. Retrieval uncertainties have been calculated for zenith measurements performed from December 1-15, 2011.

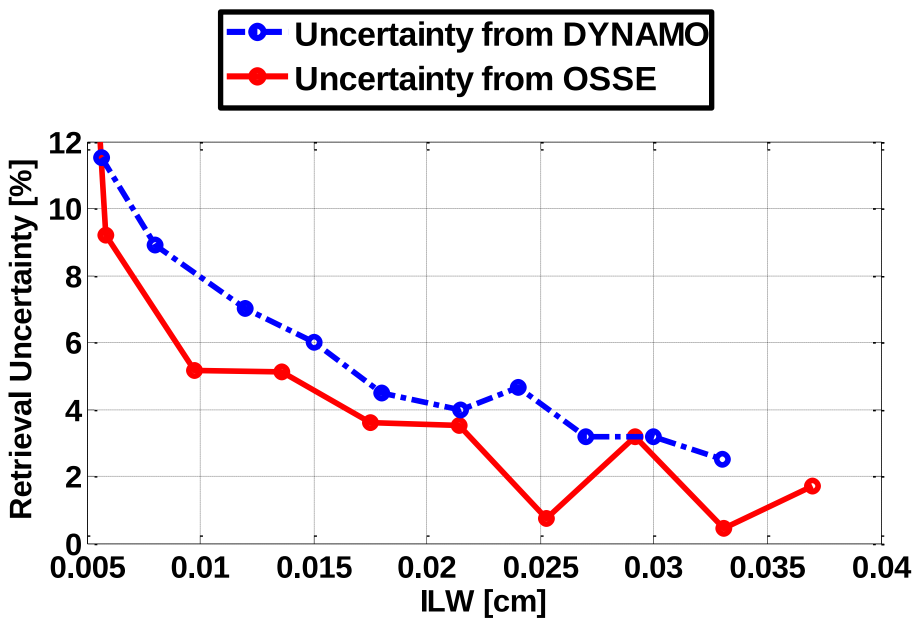

Figure 81: ILW retrieval uncertainty from OSSE (in red) and difference between radiometer estimates and radiosonde data measured during DYNAMO (in blue).

8.6. Slant Water Path and Slant Liquid Water Retrieval and Validation

This section describes the retrieval and validation of SWP and SLW at low elevation angles as well as the calculation of radiometer range.

8.6.1 Slant Water Path and Slant Liquid Water for Low Elevation Angle Measurements

Microwave radiometer measurements performed at various azimuth angles from zenith to low elevation angles are used to retrieve SWP and SLW using Eqn. (VIII.11). Models for $T_{B_{23.8}}$ and $T_{B_{30.0}}$ at 5°, 7°, 9° and 11° elevation angles were developed for a range of SWP and SLW. SWP and SLW have been retrieved for October 11, 2011 at the four low elevation angles and at azimuth angles from -50º to +150º for 21:35 UTC. The retrieved SWP and SLW are shown in Figure 82(a) and Figure 82(b), respectively, on a director cosine plane, where θ and ϕ are the elevation and azimuth angles of measurement, respectively. For elevation angles of 5° and 7°, retrieved SWP is from 27 cm to 65 cm, and it is from 20 cm to 42 cm for elevation angles of 9° and 11°. Similarly, retrieved SLW for elevation angles of 5° and 7° is from 0.05 to 0.37 cm, and it is from 0.05 to 0.17 cm for elevation angles of 9° and 11°.

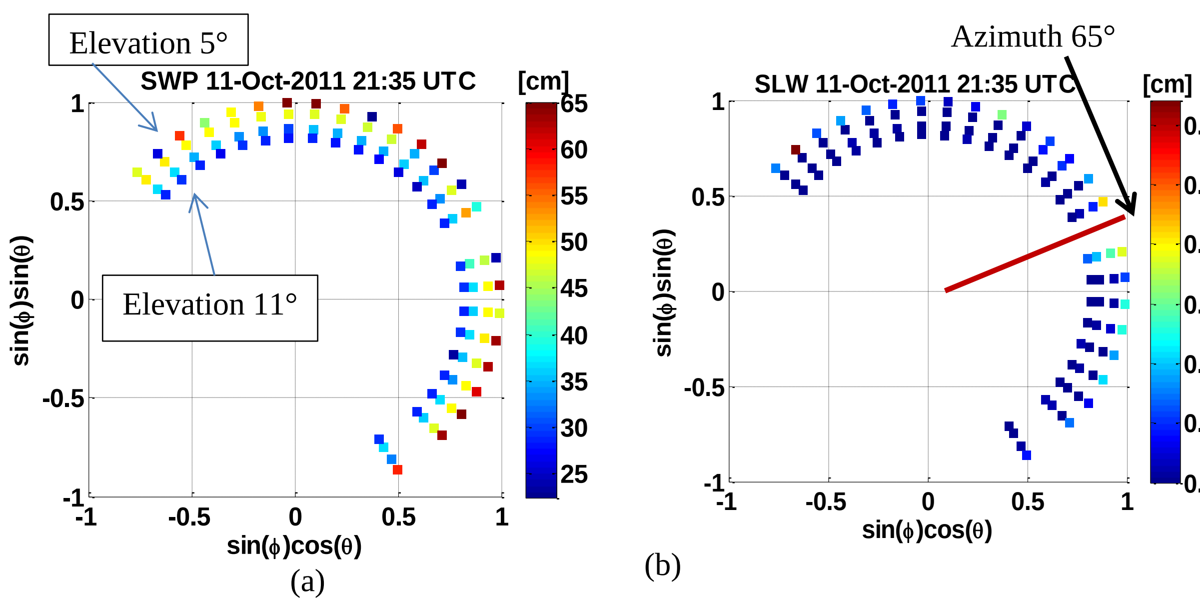

Figure 82: (a) Retrieved SWP and (b) SLW on October 11, 2011 at 21:35 UTC for all azimuth angles measured and elevation angles of 5°, 7°, 9° and 11°.

The SLW at the elevation angle of 5° and azimuth angles of -42°, 60° to 90°, 95° to 105° are greater than at the other azimuth angles. These correspond to precipitation, since the VLWR values are between 1 and 1.1, i.e. below the empirical precipitation threshold of 1.2. The radar reflectivity plan position indicator (PPI) image in Figure 83 shows measured precipitation with reflectivity 20-35 dBZ along the red segment at 65° azimuth.

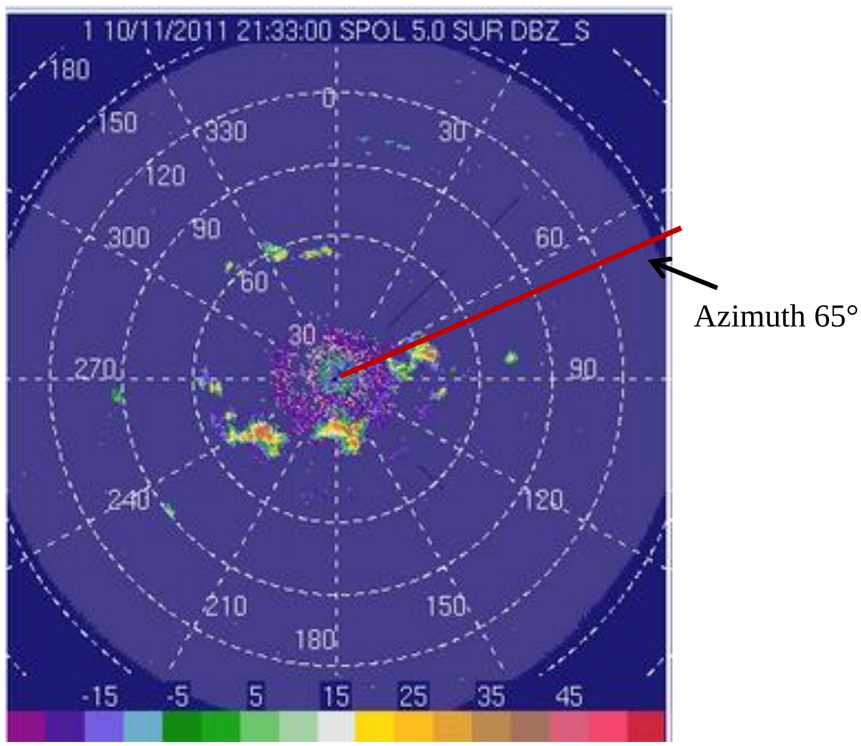

Figure 83: Radar reflectivity PPI image at 5° elevation angle on October 11, 2011 at 21:33 UTC

The performance of the retrieval algorithm for SWP and SLW is assessed using an OSSE as well as through comparison of SWP radiometer retrievals with SWP radar retrievals during the DYNAMO campaign. To implement the OSSE, radiosonde measured profiles are used to simulate $T_{B_{23.8}}$ and $T_{B_{30.0}}$, which are then used to estimate SWP and SLW at elevation angles of 5°, 7° and 9°. Uncertainties associated with the retrieval algorithm were calculated as the difference between the estimated SWP and SLW and the corresponding quantities measured by radiosondes, with the results as shown in Figure 84.

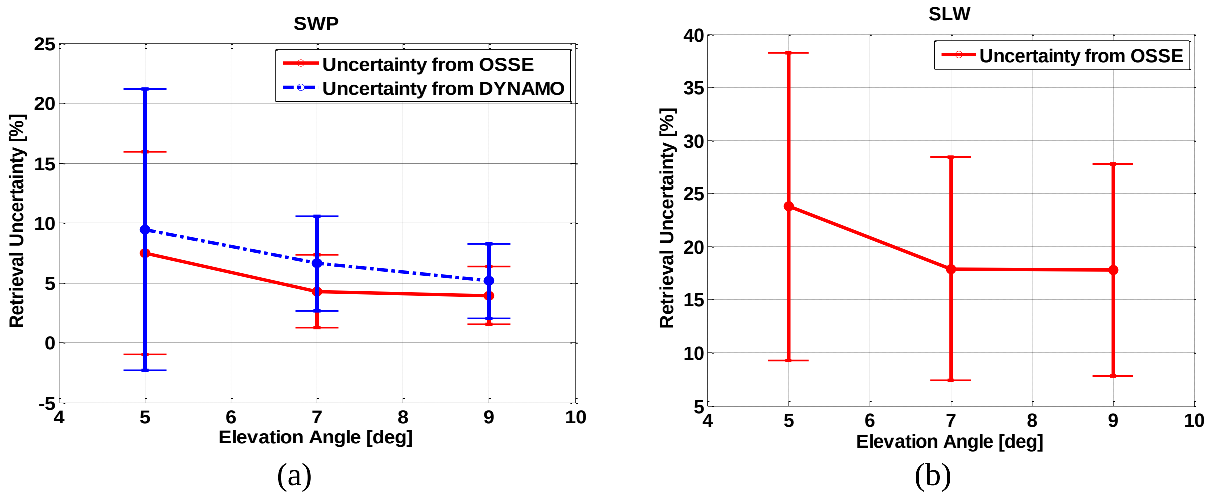

Figure 84: (a) Retrieval uncertainty of SWP at elevation angles of 5°, 7° and 9° based on an OSSE (in red). Comparison between radar- and radiometer-retrieved values of SWP (in blue). (b) Retrieval uncertainty of SLW at elevation angles of 5°, 7° and 9° based on an OSSE (in red).

SWP were retrieved using two independent measurement sources, the UM-radiometer and the NCAR S-PolKa radar, co-located during the DYNAMO experiment. To compare SWP retrievals, the radar and radiometer performed simultaneous measurements at 5°, 7° and 9° elevation angles to sample common volumes of the atmosphere. The SWP retrievals from the radar and radiometer are based on different principles due to different measurement physics. The radar measures the attenuation of the signal due to water vapor from the radar to the edge of a cloud or precipitation echo, so the range may vary substantially from measurement to measurement [85] [86]. The retrieval of SWP from radar involves comparison of the reflectivity from the edges of clouds and precipitation at 2.8 GHz (S-band), which is not significantly attenuated by water vapor, with those at 35 GHz (Ka-band), which is significantly attenuated. The attenuation value is then used to estimate the SWP. In contrast, radiometers provide a more consistent range for SWP retrieval, although greater values of attenuation often limit the range of the radiometer, depending on the atmospheric conditions. For comparison of the two retrievals, the radiometer-retrieved SWP is normalized by the equivalent range of the atmosphere measured by the radiometer and scaled by the radar range over which attenuation is measured. The radiometer measurements with elevation angles uncertainty less than 0.5° were grouped as the elevation angle under consideration and used for evaluating the accuracy of the retrieval algorithm. The equivalent radiometer range for a particular elevation angle has been computed using the path length of the atmosphere in the direction of the radiometer field of view from which 95% of the total measured power is emitted. Based on a planar atmosphere model, the equivalent radiometer ranges have been calculated as 50, 44 and 37 km for elevation angles of 5°, 7° and 9°, respectively which has been explained in the next sub-section.

The radar-retrieved SWP values are subtracted from the range-adjusted radiometer-retrieved SWP values to calculate the mean difference at each elevation angle as a percentage, as shown in the blue points in Figure 84(a), with error bars showing the standard deviation. The differences between these SWP retrievals are less than 10% for 5° elevation angle, decreasing to less than 7.5% for 7° and 9° elevation angles. Differences may be due to uncertainties in the retrieval from both the radar and radiometer, as well as to uncertainties in the range normalization for the radiometer-retrieved values. Furthermore, it can be observed that both the mean difference and its standard deviation decrease as the elevation angle increases. This is due to uncertainties that decrease at higher elevation angles since the equivalent radiometer range is typically longer than the actual radar range. On the other hand, the percentage mean error in SWP from the OSSE is less than 8% at 5° elevation angle and less than 5% at 7° and 9° elevation angles. The OSSE percentage errors are consistently approximately 2% lower than the differences between SWP retrieved from radar and radiometer measurements during DYNAMO.

The performance of the retrieval technique for estimation of SLW is based on OSSE results only because no SLW information is available from the radar measurements. Figure 84(b) shows the error of the retrieved SLW at 5°, 7° and 9° elevation angles. Exhibiting similar behavior to SWP in elevation angle with different magnitudes, the error is less than 24% at 5° elevation angle and decreasing with increasing elevation angle to less than 18% at 7° and 9° elevation angles.

8.6.2 Radiometer Range

A simulation based study is performed to determining the range of radiometer for various elevation angles. The atmosphere is considered to be horizontally stratified as in Figure II1 and most of the water vapor is present in the lowest 10 km of the troposphere.

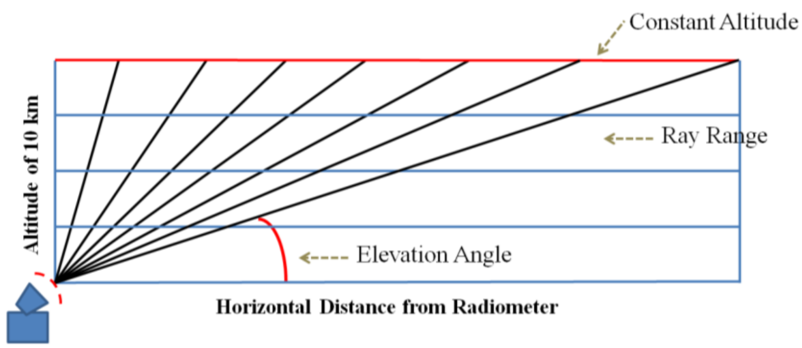

Figure 85. Radiometer scanning at various elevation angles

First, brightness temperatures are simulated for each frequency using RTE given by (I2) upto 10 km altitude in the troposphere without considering the radiometer range as shown in Figure II1. Then, brightness temperatures are again simulated using the RTE corresponding to each elevation angle but constraining the range not the altitude. The range for which brightness temperature calculated in step two is 95% of that simulated in step one is considered the actual radiometer range. This process is repeated for elevation angles 90^{o} to 5^{o} to find the radiometer range with respect to elevation angles. The radiometer range depends on the amount of atmospheric attenuation. To take into account this uncertainty, the radiometer range is calculated for different atmospheric conditions where temperature and water vapor change considerably, including light precipitating cases.

As shown in Figure II2, the radiometric range is 10 km for zenith angles 0° to 35° and it increases from 10 to 55 km for zenith angles 35° to 85°. The standard deviation of range is 1 km for 0° zenith angle and increases to 5 km for 85° zenith angle. These ranges have been calculated by considering weather conditions at Gan Island during DYNAMO experiment and they are expected to change with weather conditions and place.

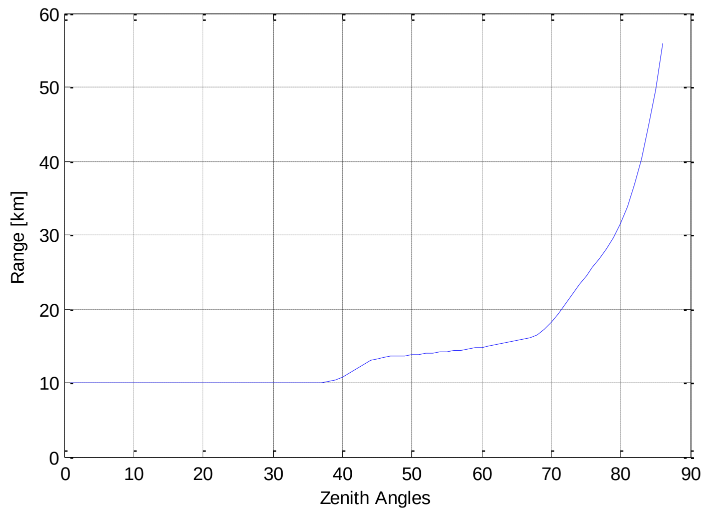

Figure II3. Dependence of the radiometric ranges on zenith angles.

8.7. Conclusions

In this chapter a new retrieval algorithm has been developed to retrieve SWP and SLW from ground-based microwave radiometer measurements from zenith to low elevation angles. To accomplish this, the vapor-liquid water ratio (VLWR) has been defined as the ratio of the brightness temperature at 23.8 GHz to that at 30.0 GHz. The sensitivities of VLWR to both atmospheric water vapor and liquid water are found to differ substantially as a function of elevation angle of radiometer measurements. The new retrieval algorithm was validated using ground-based University of Miami (UM) microwave radiometer measurements at 23.8 and 30.0 GHz performed on Gan Island during the DYNAMO Experiment. Retrievals of IWV and ILW from zenith pointing UM-radiometer measurements show good agreement between these quantities and those calculated from radiosonde measurements, with differences of less than 5% and 12% for IWV and ILW, respectively, where IWV is for all weather conditions, while ILW includes cloudy and precipitating conditions. The differences for ILW retrievals are 12% for the lowest ILW values and rapidly decrease with increasing ILW to less than 5% for ILW values greater than 0.0175 cm. The differences between retrieved IWV and ILW and those calculated from radiosonde measurements agree well with retrieval uncertainties found using an OSSE.

The new retrieval algorithm was also used to estimate SWP and SLW from UM-radiometer measurements at low elevation angles during DYNAMO. To the authors' knowledge, this is the first time that microwave radiometer-retrieved SWP has been validated by comparison with radar-retrieved SWP, showing a mean difference of less than 10% at 5° elevation angle and less than 7.5% at 7° and 9° elevation angles, decreasing as the elevation angle increases. These mean differences and their dependence on elevation angle agree well with SWP retrieval uncertainties found using an OSSE. For liquid water, the OSSE shows that the retrieval error in SLW is less than 24% at 5° elevation angle, decreasing to less than 18% at 7° and 9° elevation angles. Such retrievals of SWP and SLW are useful for characterizing the spatial and temporal variation in the distribution of water vapor and liquid water in the lower troposphere, which may in turn contribute to improved forecasting of convective initiation and precipitation. VLWR is sensitive to precipitation intensity and precipitation range. These correlations can be used to develop a relationship to determine intensity and distance of precipitation from the radiometer.

Chapter IX Conclusions and Future Work

9.1. Conclusions

One of the main goals of the research work presented in this dissertation is to perform a comprehensive analysis of various methods of improving vertical resolution, accuracy, detection of gradients and dynamic changes in estimated water vapor profiles using microwave and millimeter-wave radiometer measurements. Therefore, two methods have been followed for improving water vapor retrieval using Bayesian optimal estimation technique which uses measured brightness temperatures as inputs.

- First is a theoretical study, used for determination of measurement frequencies in the 10-200 GHz range which provide the highest DOF of measurements for retrieval of water vapor and temperature profiles as explained in Chapter IV. Maximizing the DOF of measurements maximizes the amount of information provided to the retrieval and hence is important for improving vertical resolution and accuracy.
- Second method is to optimize the background information covariance matrix and layer thickness used in the estimation technique as discussed in Chapter V. This optimization results in the background data set being correlated with the water vapor profile during measurement. This background data set plays an important role in improving the ability to detect dynamic changes and gradients in water vapor profiles during clear sky conditions. The field campaign HUMEX11 at the central facility of the ARM site in SGP, Oklahoma was designed to assess the ability to remotely sense dynamic changes and gradients in atmospheric water vapor profiles retrieved from K-band microwave brightness temperatures.

For determining frequencies with highest DOF for water vapor and temperature profile estimation a branch and bound feature selection algorithm was used. It was found that the frequencies in the ranges of 20 – 23 GHz, 85 – 90 GHz and 165 – 200 GHz provide the maximum number of independent pieces of information for water vapor profile retrieval from zenith-pointing ground-based as well as nadir viewing airborne microwave radiometer measurements. The maximum number of independent pieces of information is 5 – 6 from ground based and 8 – 9 from airborne radiometers for water vapor profiling. Temperature profiling requires the use of frequency ranges 55 – 65 GHz and 116 – 120 GHz for maximizing number of independent pieces of information for ground-based measurements. The frequencies required for nadir-pointing airborne measurements of temperature profile are similar to the ground-based measurement. In addition to that millimeter-wave frequency at 118.75 GHz is also required for airborne measurements. The maximum number of independent pieces of information is 6 – 7 for temperature profiling from ground and 5 – 6 for airbourne instruments. Inclusion of additional measurement frequencies results in redundant information about the atmospheric parameter of interest since that information is linearly dependent on that already measured at other frequencies.

Measurement noise and uncertainty analyses have shown that DOF and vertical resolution are inversely proportional to measurement uncertainty and instrument noise. Similarly, it was found that there is an inverse relationship between vertical resolution and DOF. Therefore, to get the best performance in terms of vertical resolution and accuracy, a low noise radiometer need to be designed with maximum number of independent measurement frequencies.

For improving the ability to detect dynamic changes and gradients, an analysis is performed to determine the optimum background data set size as well as layer thickness which will be used for cases when the background data set is correlated with the atmospheric state during the radiometric measurement time and therefore, represents variability associated with water vapor profile.

To determine the optimum background data set size, eigenvalue analysis of covariance matrix for the data set sizes of 110 and 1400 profiles (for both the layer thickness of 100 and 500 m) is performed. The maximum variability peak occurs for data set size of approximately 25-35 profiles. However, the maximum accuracy is achieved by using a data set of 40-60 profiles. So, there is a balance between ability to achieve maximum accuracy and using the maximum variability data set, which provides the maximum information to sense dynamic changes. This is because the data set variability can be associated not only to atmospheric dynamic changes but also to noise. To reduce the effect of noise it is necessary that the collected data set has statistical significance, and usually this is achieved by the increasing the data set size above the size of 30-40 profiles. Therefore, the optimal background data set for minimum retrieval error has to be short enough to be close in time to the measurements but not so short that is not statistically significant.

Analyses have also proved that large background data sets provide better accuracy in a statistical sense, but dynamic changes cannot be detected. Therefore, a large background data set is less than optimal for sensing dynamic changes in the atmosphere. However, sometimes background data taken close to radiometric measurements might not be available. In that case, the best performance is obtained by using a large data set taken over a long period of time representing seasonal variability. This makes the retrieval tend toward a “standard atmosphere”.

So optimum background data set with thin layers can be used to retrieve water vapor profile on days when weather is quickly evolving while large background data set with thicker layer can be used when the weather is nearly constant. Therefore, depending on the weather conditions, the sizes of background data sets and layer thicknesses can be chosen appropriately.

Another goal of the dissertation is to develop a new retrieval algorithm for estimation of SWP and SLW from UM-radiometer measurements performed at low elevation angles of 5º, 7º, 9º and 11º during the DYNAMO experiment. However, the radiometer measurements at those elevation angles were found to have anisotropy which varied with the azimuth angle of measurement. This azimuth anisotropy was observed for clear sky conditions while they were not evident for rainy and cloudy conditions as discussed in Chapter VII. Various possible source/sources of anisotropy were analyzed and it was found that a change of 0.5º to 1º in the 5º elevation produces a brightness temperature difference of 10-20 K and 20-30 K for 23.8 GHz and 30 GHz measurement frequencies, respectively. These values of brightness temperatures are similar to the anisotropy amplitude observed. It was inferred that the sand underneath the base of the radiometer pedestal was not perfectly stable due to which radiometer elevation angle changed as it scanned the volume of the atmosphere for the azimuth angle range -50º to 150º.

These brightness temperatures were used along with VLWR to develop a new retrieval algorithm to estimate IWV and ILW for zenith pointing measurements. VLWR is defined as the ratio of the brightness temperature at 23.8 GHz to that at 30.0 GHz and it's sensitivity to both atmospheric water vapor and liquid water is found to differ substantially as a function of elevation angle of radiometer measurements as explained in Chapter VIII. Retrievals of IWV and ILW from zenith pointing UM-radiometer measurements show good agreement between these quantities and those calculated from radiosonde measurements, with differences of less than 5% and 12% for IWV and ILW, respectively, where IWV is for all weather conditions, while ILW includes cloudy and precipitating conditions. The new retrieval algorithm was also used to estimate SWP and SLW from UM-radiometer measurements at low elevation angles during DYNAMO. Microwave radiometer-retrieved SWP has been validated by comparison with radar-retrieved SWP, showing a mean difference of less than 10% at 5° elevation angle and less than 7.5% at 7° and 9° elevation angles, decreasing as the elevation angle increases. These mean differences and their dependence on elevation angle agree well with SWP retrieval uncertainties found using an OSSE.

9.2. Future Work

Some recommendations for future work are as follows:

1) Determining optimum background data set size for water vapor profile retrieval for various ARM sites in the US for different weather conditions. This background data set can be used for determining dynamic changes in the water vapor profile in those sites when the measurements are taken close to the background data set.
2) Determination of the optimum background data set size and layer thickness for temperature profile retrieval using eigenvalue and accuracy analyses. Use of brightness temperature measurements performed by microwave radiometer profiler [87] for frequency range of 50-59 GHz to retrieve temperature profiles using the optimum background data set taken at ARM site. These profiles can be used for estimating the dynamic changes and gradients in the temperature profiles which in-turn can increase the accuracy of the water vapor profile when radiosonde data is not available as *a-priori* close to the measurement time.
3) Comparison of the retrieved temperature profile with those from AERI so as to determine the associated retrieval error.

4) Comparison of the SLW retrieved from radiometer measurements with those from the S-PolKa radar at the elevation angles of 5º, 7º, 9º and 11º to determine the retrieval error for SLW estimation.
5) Modelling of the brightness temperatures at 23.8 and 30.0 GHz using the radiative transfer code by DOE. Retrieval of SWP and SLW using these modeled brightness temperatures and comparison of these SWP and SLW accuracy with those from the model used in Chapter VIII will provide proper information about the performance of the retrieval technique.
6) The observed variation of VLWR with elevation angles during clear, cloudy and precipitating conditions in Chapters VIII and IX can be used for determining the distance of precipitation from radiometer or the height of cloud base.

Bibliography

[1] S. C. Sherwood, R. Roca, T. M. Weckwerth and N. G. Andronova, "Tropospheric water vapor, convection and climate," *Rev. of Geophys.*, pp. 1-30, 2010.

[2] F. Fabry, "The spatial variability of moisture in th boundary layer and its effect on convection initiation: Project-long characterization," *Mon. Wea. Rev.*, vol. 134, pp. 79-91, 2006.

[3] H. R. Byers and R. R. Braham, "Thunderstorm structure and circulation," *J. Meteor.*, vol. 5, pp. 71-86, 1948.

[4] D. D. Turner, S. A. Clough, J. C. Liljegren, E. E. Clothiaux, K. E. Cady-Pereira and K. L. Gaustad, "Retrieving liquid water path and precipitable water vapor from the atmospheric radiation measurement (ARM) microwave radiometers," *IEEE Trans. Geosci. Remote Sens.*, vol. 45, no. 11, pp. 3680 - 3690, Nov. 2007.

[5] S. Padmanabhan, S. C. Reising, J. Vivekanandan and F. Iturbide-Sanchez, "Retrieval of atmospheric water vapor density with fine spatial resolution using 3-D tomographic inversion of microwave brightness temperatures measured by a network of scanning compact radiometers," *IEEE Trans. Geosci. Remote Sensing*, vol. 47, no. 11, pp. 3708-3721, Nov. 2009.

[6] W. F. Feltz, H. B. Howell, R. O. Knuteson, H. M. Woolf and H. . E. Revercomb, "Near continuous profiling of temperature, moisture, and atmospheric stability using the atmospheric emitted radiance interferometer (AERI)," *J. Appl. Meteor.*, vol. 42, pp. 584-597, 2003.

[7] Y. H. Kuo, Y. R. Guo and E. R. Westwater, "Assimilation of precipitable water measurements into a mesoscale model," *Mon. Wea. Rev.*, vol. 121, no. 4, pp. 1215-1238, 1993.

[8] M. N. Deeter and K. F. Evans, "Mesoscale variations of water vapor inferred from millimeter-wave imaging radiometer during TOGA COARE," *J. Appl. Meteorol.*, vol. 36, no. 2, p. 183–188, Feb. 1997.

[9] H. Seko, H. Nakamura, Y. Shoji and T. Iwabuchi, "The meso-gamma scale water vapor distribution associated with thunderstorm calculated from a dense network of GPS receivers," *J. Meteorol. Soc. Jpn.,* vol. 82, no. 1B, pp. 569-586, Mar. 2004.

[10] D. H. Lenschow and B. B. Stankov, "Length scales in the convective boundary layer," *J. Atmos. Sci.,* vol. 43, no. 12, p. 1198–1209, Jun. 1986.

[11] T. J. Hewison, *Profiling temperature and humidity by ground-based microwave radiometers,* Reading: The University of Reading, 2006.

[12] T. J. Hewison, "1D-VAR retrieval of temperature and humidity profiles from a ground-based microwave radiometer," *IEEE Trans. Geosci. Remote Sens.*, vol. 45, no. 7, pp. 2163-2168, Jul. 2007.

[13] U. Löhnert, S. Crewell and C. Simmer, "An integrated approach toward retrieving physically consistent profiles of temperature, humidity, and cloud liquid water," *J. Appl. Meteor.,* vol. 43, pp. 1295-1307, Sept. 2004.

[14] C. D. Rodgers, Inverse Methods for Atmospheric Sounding: Theory and Practice, Singapore: World Scientific, 2000.

[15] M. A. Janssen, "An introduction to the passive remote sensing of atmosphere," in *Atmospheric Remote Sensing by Microwave Radiometry*, New York, Wiley-Interscience, 1993, p. 1–35.

[16] F. S. Solheim, J. R. Godwin, E. R. Westwater, Y. Han, S. J. Keihm, K. Marsh and R. Ware, "Radiometric profiling of temperature, water vapor, and cloud liquid water using various inversion methods," *Radio Sci.,* vol. 33, pp. 393 - 404, 1998.

[17] T. M. Scheve and C. T. Swift, "Profiling atmospheric water vapor with a K-band spectral radiometer," *IEEE Trans. Geosci. Remote Sens.*, vol. 37, no. 3, p. 1719–1729, May 1999.

[18] R. A. Ferrare, D. D. Turner, M. Clayton, B. Schmid, J. Redemann, D. Covert, R. Elleman, J. Ogren, E. Andrews, E. Goldsmith and H. Johsson, "Evaluation of daytime measurements of aerosols and water vapor made by an operational Raman lidar over the Southern Great Plains," *J. Geophys. Res.,* vol. 111, no. D05S08, doi:10.1029/2005JD005836, 2006.

[19] A. V. Bosisio and G. Drufuca, "Retrieval of two-dimensional absorption coefficient structure from a scanning radiometer at 23.8 GHz," *Radio Sci.*, vol. 38, no. 3, p. 8038, 2003.

[20] L. N. Trefethen and D. Bau III, Numerical linear algebra, Philadelphia: Society for Industrial and Applied Mathematics, 1997.

[21] F. Iturbide-Sanchez, S. C. Reising and S. Padmanabhan, "A miniaturized spectrometer radiometer based on MMIC technology for tropospheric water vapor profiling," *IEEE Trans. Geosci. Remote Sens.*, vol. 44, no. 7, pp. 2181-2193, 2007.

[22] J. Hamilton, Time Series Analysis, Princeton University Press, 1994.

[23] F. Ulaby, R. Moore and A. Fung, Microwave Remote Sensing: Active and Passive, Vol. I - Microwave Remote Sensing Fundamentals and Radiometry, Reading, MA: Addison-Wesley, 1981.

[24] R. J. Hill, "Water vapor-absorption line shape comparison using the 22-GHz line: The Van Vleck-Weisskopf shape affirmed," *Radio Sci.*, vol. 21, pp. 447-451, May-June 1986.

[25] W. H. Press, S. A. Teukolsky, W. T. Vetterling and B. P. Flannery, Numerical Recipes: The Art of Scientific Computing, New York: Cambridge University Press, 2007.

[26] S. Sahoo, S. C. Reising, S. Padmanabhan, J. Vivekanandan, F. Iturbide-Sanchez, N. Pierdicca, E. Pichelli and D. Cimini, "3-D humidity retrieval using a network of compact microwave radiometers to correct for variations in wet tropospheric path delay in spaceborne interferometric SAR imagery," *IEEE Trans. Geosci. Remote Sens.*, vol. 49, no. 9, pp. 3281-3290, 2011.

[27] J. C. Liljegren, E. E. Clothiaux, G. G. Mace, S. Kato and X. Dong, "A new retrieval for cloud liquid water path using a ground-based microwave radiometer and measurements of cloud temperature," *J. Geophys. Res.*, vol. 106, no. D13, pp. 14485-14500, Jul. 2001.

[28] E. R. Westwater, "Ground-based microwave remote sensing of meteorological variables," in *Atmospheric Remote Sensing by Microwave Radiometry*, New York, Wiley, 1993, p. 145–214.

[29] L. Li, J. Vivekanandan, C. H. Chan and L. Tsang, "Microwave radiometric technique to retrieve vapor, liquid and ice, Part I-Developement of neural network-based inversion method," *IEEE Trans. Geosci. Remote Sens.*, vol. 35, no. 2, pp. 224-236, 1997.

[30] K. Gilliam, *Personal communication,* Fort Collins: Colorado State University, 2013.

[31] P. W. Rosenkranz, "Absorption of microwaves by atmospheric gases," in *Atmospheric*

Remote Sensing by Microwave Radiometry, New York, Wiley-Interscience Publication, 1993, pp. 37-79.

[32] H. J. Liebe, "A contribution to modeling atmospheric millimeter-wave properties," *Frequenz,* vol. 41, pp. 31-36, 1987.

[33] H. J. Liebe, G. A. Hufford and T. Manabe, "A model for the complex permittivity of water at frequencies below 1 THz," *International J. of Infrared and Millimeter Waves,* vol. 12, no. 7, pp. 659-675, 1991.

[34] H. J. Liebe, G. A. Hufford and M. G. Cotton, "Atmospheric propagation effects through natural and man-made obscurants for visible to MM-Wave radiation," in *AGARD Conf. Proc. 542*, 1993.

[35] P. Rosenkranz, "Water vapor microwave continuum absorption: A comparison of measurements and models," *Radio Sci.,* vol. 33, no. 4, pp. 919-928, Jul.-Aug. 1998.

[36] S. Sahoo, X. Bosch-Lluis, S. C. Reising and J. Vivekanandan, "Radiometric information content for water vapor and temperature profiling in clear skies between 10-200 GHz," *IEEE J. Sel. Topics Appl. Earth Observ. Remote Sens.*, 2014.

[37] J. M. Aparicio and S. Laroche, "An evaluation of the expression of the atmospheric refractivity for GPS signals," *J. Geophys. Res.,* vol. 116, no. D11104, pp. 1-14, 2011.

[38] C. Henrickson, Chemistry, Cliffs Notes, 2005.

[39] R. H. Perry and D. W. Green, Perry's Chemical Engineers' Handbook, McGraw-Hill, 2008.

[40] J. H. Van Vleck, "The absorption of microwaves by uncondensed water vapor," *Phys. Rev.,* vol. 71, pp. 425-433, 1947.

[41] S. Sahoo, X. Bosch-Lluis, S. C. Reising and J. Vivekanandan, "Optimization of background information and layer thickness for improved accuracy of water vapor profile retrieval from ground-based microwave radiometer measurements at K-band," *IEEE J. Sel. Topics Appl. Earth Observ. Remote Sens.,* 2014.

[42] E. R. Westwater, S. Crewell and C. Matzler, "Surface-based microwave and millimeter wave radiometric remote sensing of the troposphere: A tutorial," *IEEE Geosci. Remote Sens. Newsletter,* pp. 16 - 33, March 2005.

[43] D. Cimini, E. R. Westwater and A. J. Gasiewski, "Temperature and humidity profiling in the

Arctic using millimeter-wave radiometry and 1DVAR," *IEEE Trans. Geosci. Remote Sens.*, vol. 48, no. 3, p. 1381– 1388, Mar. 2010.

[44] J. Wang and L. Zhangs, "Systematic errors in global radiosonde precipitable water data from comparisons with ground-based GPS measurements," *J. Climate,* vol. 21, pp. 2218-2238, 2008.

[45] J. E. M. Goldsmith, F. H. Blair, S. E. Bisson and D. D. Turner, "Turn-Key Raman lidar for profiling atmospheric water vapor, clouds, and aerosols," *Appl. Opt.,* vol. 37, no. 21, pp. 4979-4990, July 1998.

[46] A. S. Milman, Mathematical Principles of Remote Sensing: Making Inferences from Noisy Data, MI: CRC Press, 2000.

[47] J. Randa, J. Lahtinen, A. Camps, A. J. Gasiewski, M. Hallikainen, D. M. Le Vine, M. Martin-Neira, J. Piepmeier, P. W. Rosenkranz, C. S. Ruf, J. Shiue and N. Skou, "Recommended Terminology for Microwave Radiometry," NIST Technical Note TN1551; National Institute of Standards and Technology, Gaithersburg, MD, USA, 2008.

[48] N. C. Grody, "Remote Sensing of the atmosphere from satellites using microwave radiometry," in *Atmospheric Remote Sensing by Microwave Radiometry*, New York, Wiley-Interscience, 1993, pp. 259 - 314.

[49] A. J. Gasiewski, "Channel ranking in passive microwave wet-path delay measurements," in *Proc. IEEE Geosci. Remote Sens. Symp.*, 1993.

[50] M. Klein and A. J. Gasiewski, "The Sensitivity of Millimeter and Sub-millimeter Frequencies to Atmospheric Temperature and Water Vapor Variations," in *Proc. IEEE Geosci. Remote Sens. Symp.*, 1998.

[51] M. P. Cadeddu, J. C. Liljegren and D. D. Turner, "The atmospheric radiation measurement (ARM) program network of microwave radiometers: Instrumentation, data and retrievals," *Atmos. Meas. Tech.,* vol. 6, pp. 2359-2372, 2013.

[52] I. Guyon and A. Elisseeff, "An introduction to variable and feature selection," *J. of Machine Learning Research*, vol. 3, pp. 1157 - 1182, March 2003.

[53] O. Ludwig and U. Nunes, "Novel maximum-margin training algorithms for supervised neural networks," *IEEE Trans. Neural Network*, vol. 21, no. 6, pp. 972 - 984, Jun. 2010.

[54] P. M. Narendra and K. Fukunaga, "A branch and bound algorithm for feature subset selection," *IEEE Trans. Comput.*, Vols. C-26, no. 9, pp. 917 - 921, 1977.

[55] P. C. Pandey, E. G. Njoku and J. W. Waters, "Inference of cloud temperature and thickness by microwave radiometry from space," *J. Climate Appl. Meteor.*, vol. 22, pp. 1894 - 1898, July 1983.

[56] J. A. Weinman, "The effect of cirrus clouds on 118-GHz brightness temperatures," *J. Geophys. Res.*, vol. 93, no. D9, pp. 11059 - 11062, Sept. 1988.

[57] C. Kummerow, Y. Hong, W. S. Olson, S. Yang, R. F. Adler, . J. McCollum, R. Ferraro, G. Petty, D.-B. Shin and T. T. Wilheit, "The evolution of the Goddard profiling algorithm (GPROF) for rainfall estimation from passive microwave sensors," *J. Appl. Meteor.*, vol. 40, pp. 1801-1820, Jun. 2001.

[58] P. E. Racette, E. R. Westwater, Y. Han, A. J. Gasiewski, M. Klein, D. Cimini, D. C. Jones, W. Manning, E. J. Kim, J. R. Wang, V. Leuski and P. Kiedron, "Measurement of low amounts of precipitable water vapor using ground-based millimeterwave radiometry," *J. Atmos. Oceanic Technol.*, vol. 22, pp. 317-337, April 2005.

[59] V. H. Payne, E. J. Mlawer, K. E. Cady-Pereira and J. Moncet, "Water vapor continuum absorption in the microwave," *IEEE Trans. Geosci. Remote Sens.*, vol. 49, no. 6, p. 2194 – 1388, Jun. 2011.

[60] M. N. Deeter and K. F. Evans, "Mesoscale variations of water vapor inferred from millimeter-wave imaging radiometer during TOGA COARE," *J. Appl. Meteor.*, vol. 36, no. 2, p. 183–188, Feb. 1997.

[61] H. Seko, H. Nakamura, Y. Shoji and T. Iwabuchi, "The meso-gamma scale water vapor distribution associated with thunderstorm calculated from a dense network of GPS receivers," *J. Meteor. Soc. Japan*, vol. 82, no. 1B, pp. 569-586, Mar. 2004.

[62] D. H. Lenschow and B. B. Stankov, "Length scales in the convective boundary layer," *J. Atmos. Sci.*, vol. 43, no. 12, p. 1198–1209, Jun. 1986.

[63] National Research Council Committee on Developing Mesoscale Meteorological Observational Capabilities to Meet Multiple National Needs, "Observing Weather and Climate from the Ground Up: A Nationwide Network of Networks," National Academies

Press, Washington, DC, 2009.

[64] R. A. Ferrare, D. D. Turner, M. Clayton, B. Schmid, J. Redemann, D. Covert, R. Elleman, J. Ogren, E. Andrews, E. Goldsmith and H. Johsson, "Evaluation of daytime measurements of aerosols and water vapor made by an operational Raman lidar over the Southern Great Plains," *Journal of Geophysical Research,* vol. 111, no. D05S08, doi:10.1029/2005JD005836, 2006.

[65] D. Turner, "Raman Lidar (RL) Handbook," U.S. Department of Energy, Office of Science, Office of Biological and Environmental Research, 2004.

[66] D. Cimini, T. J. Hewison, L. Martin, J. Güldner and F. S. Marzano, "Temperature and humidity profile retrievals from groundbased microwave radiometers during TUC," *Meteor. Z.*, vol. 15, no. 5, p. 45–56, Feb. 2006.

[67] Atmospheric and Environmental Research, Inc., "Algorithm theoretical basis document (ATBD) for the conical-scanning microwave imager/sounder (CMIS) environmental data records (EDRs)," 15 March 2001. [Online]. Available: https://www.aer.com/sites/default/files/atbd_v07-1_CIWP.pdf. [Accessed 15 May 2014].

[68] J. J. Braun and C. Rocken, "Water vapor tomography within the planetary boundary layer using GPS," in *Int. Workshop on GPS Meteor.*, Tsukuba, Japan, 2003.

[69] F. Iturbide-Sanchez, S. C. Reising and S. Padmanabhan, "A Miniaturized Spectrometer Radiometer Based on MMIC Technology for Tropospheric Water Vapor Profiling," *IEEE Trans. Geosci. Remote Sens.,* vol. 44, no. 7, pp. 2181-2193, 2007.

[70] Y. Han and E. R. Westwater, "Analysis and improvement of tipping calibration for ground-based microwave radiometers," *IEEE Trans. Geosci. Remote Sens.*, vol. 38, no. 3, p. 1260–1277, May 2000.

[71] W. L. Ecklund, D. A. Carter and B. B. Balsley, "A UHF wind profiler for the boundary layer: Brief description and initial results.," *J. Atmos. Oceanic Technol.,* vol. 5, p. 432–441, 1988.

[72] M. Decker, E. Westwater and F. Guiraud, "Experimental evaluation of ground-based microwave sensing of atmospheric temperature and water vapor profile," *J. Appl. Meteor.,* vol. 17, no. 12, p. 1788–1795, Dec. 1978.

[73] M. P. Cadeddu, "Microwave Radiometer - 3 Channel (MWR3C) Handbook 01 May 2012. [Online]. Available: [Accessed 15 May 2014].," 01 May 2012. [Online]. Available: http://www.arm.gov/publications/tech_reports/handbooks/mwr3c_handbook.pdf?id=24.. [Accessed 15 May 2014].

[74] V. R. Morris, ""Microwave Radiometer (MWR) Handbook," Aug. 2006. [Online]. Available: http://www.arm.gov/publications/tech_reports/handbooks/mwr_handbook.pdf?id=36.. [Accessed 15 May 2014].

[75] "DYNAMO Documentation," Jan 2010. [Online]. Available: http://www.eol.ucar.edu/projects/dynamo/documents/index.html. [Accessed 28 May 2014].

[76] "DYNAMO Data Access," 2011. [Online]. Available: http://data.eol.ucar.edu/master_list/?project=DYNAMO. [Accessed 28 May 2014].

[77] C. Zhang, "Madden-Julian Oscillation," *Rev. Geophys.*, vol. 43, no. 2, pp. 1-36, June 2005.

[78] G. Farquharson, F. Pratte, M. Pipersky, D. Ferraro, A. Phinney, E. Loew, R. A. Rilling, S. M. Ellis and J. Vivekanandan, "NCAR S-Pol second frequency (Ka-band) radar," in *Proc. of 32nd Conf. on Radar Meteor.*, 2005.

[79] K. Yoneyama, C. Zhang and C. N. Long, "Tracking pulses of the Madden-Julian oscillation," *Bull. Amer. Meteorol. Soc.*, pp. 1871 - 1891, 2013.

[80] E. L. Daley, "The Effects of a Remote Atoll and Lagoon on the Marine Boundary Layer," Naval Postgraduate School, Monterey, California, Dec. 2012.

[81] A. V. Bosisio, P. Ciotti, E. Fionda and A. Martellucci, "Rainy event detection by means of observed brightness temperature ratio," in *12th Specialist Meeting on Microwave Radiometry and Remote Sensing of the Environment (Microrad)*, Frascati, Italy, 5-9 March 2012.

[82] C. Mätzler and J. Morland, "Refined physical retrieval of integrated water vapor and cloud liquid for microwave radiometer data," *IEEE Geosci. Remote Sens.*, vol. 47, no. 6, pp. 1585-1594, June 2009.

[83] A. J. Gasiewski, "Microwave radiative transfer in hydrometeors," in *Atmospheric Remote Sensing by Microwave Radiometry*, New York, Wiley, 1993, pp. 91-144.

[84] B. Rilling, NCAR, 2012. [Online]. Available: http://www.eol.ucar.edu/rsf/image_archive/dynamo/spol/sur/. [Accessed 28 May 2014].

[85] R. Meneghini, L. Liao and L. Tian, "A feasibility study for simultaneous estimates of water vapor and precipitation parameters using a three-frequency radar," *J. Appl. Meteor.*, vol. 44, pp. 1511-1525, Oct. 2005.

[86] S. M. Ellis and J. Vivekanandan, "Water vapor estimates using simultaneous dual-wavelength radar observations," *Radio Sci.*, vol. 45, no. 5, p. doi: 10.1029/2009RS004280, Oct. 2010.

[87] J. C. Lilijegren, B. M. Lesht, S. Kato and E. E. Clothiax, "Evaluation of profiles of temperature, water vapor, and cloud liquid water from a new microwave radiometer," in *Eleventh ARM Science Team Meeting Proceedings*, Atlanta, Mar. 19-23, 2001.

[88] "Convection," Wikipedia, 9 Mar. 2014. [Online]. Available: http://en.wikipedia.org/wiki/Convection. [Accessed 30 Oct. 2014].

[89] "What is convection," Weather quiestions, Mar. 2014. [Online]. Available: http://www.weatherquestions.com/What_is_convection.htm. [Accessed 30 Oct. 2014].

[90] P. Schlosser, S. Pfirman and M. Ting, "The Climate System," Columbia University, Jan. 2008. [Online]. Available: http://eesc.columbia.edu/courses/ees/climate/lectures/atm_phys.html. [Accessed 30 Oct. 2014].

[91] B. Stevens, "Atmospheric moist convection," *Ann. Rev. Earth Planet Sci.*, vol. 33, p. 605–643, 2005.

[92] M. A. Tompkins, "A prognostic parameterization for the subgrid-scale variability of water vapor and clouds in large-scale models and its use to diagnose cloud cover," *J. Atmos. Sci.*, vol. 59, pp. 1917-1942, 2002.

[93] "Dynamic Precipitation and Convective Precipitaion," Weather Prediction, Jun. 2012. [Online]. Available: http://www.theweatherprediction.com/habyhints/336/. [Accessed 31 Oct. 2014].

[94] "Lifting Mechanisms," North Carolina State University, 25 Jun. 2012. [Online]. Available: http://www.nc-climate.ncsu.edu/edu/k12/.LiftingMechanisms. [Accessed 30 Oct. 2014].

[95] "METR 4433," Oklahoma University, 2011 January. [Online]. Available: kkd.ou.edu/METR4433_Spring_2011/HCRs.pdf. [Accessed October 2014].

[96] "Convergence Lines," Weather Service of New Zealand, 17 October 2012. [Online]. Available: http://blog.metservice.com/2012/10/convergence-lines/. [Accessed 17 October 2014].